Water and Thermal Management of PEM Fuel Cells

By:

Raja Muhammad Aslam Raja Arif

A thesis submitted in partial fulfilment of the requirements for the degree of
Doctor of Philosophy

The University of Sheffield
Faculty of Engineering
Department of Mechanical Engineering

March 2018

AUTHOR'S DECLARATION

Hereby I, Raja Muhammad Aslam Raja Arif confirm that the work submitted is my own and that appropriate credit has been given where reference has been made to the work of others.

The work in Chapter 4 of this thesis has appeared in publication as follows:

***R. M. Aslam**, D. B. Ingham, M. S. Ismail, K. J. Hughes, L. Ma, and M. Pourkashanian, "Simultaneous direct visualization of liquid water in the cathode and anode serpentine flow channels of proton exchange membrane (PEM) fuel cells," Journal of Energy Institute, pp. 1–14, 2017.*

All the other authors were in my supervisory group who provide advices and suggestions regarding the research direction and analysis approaches.

The work in Chapter 5 of this thesis has appeared in publication as follows:

***R. M. Aslam**, D. B. Ingham, M. S. Ismail, K. J. Hughes, L. Ma, and M. Pourkashanian, "Simultaneous thermal and visual imaging of liquid water of the PEM fuel cell flow channels," Journal of Energy Institute, pp. 1–8, 2018.*

Similarly, all the other authors were in my supervisory group who provide advices and suggestions regarding the research direction and analysis approaches.

ACKNOWLEDGEMENTS

First and foremost, my deep gratitude goes to my God for His blessings upon me for my entire life. Without His mercy and bounties, I will not able to do anything in this world.

I would like to express my sincere gratitude to my supervisors, Prof. M. Pourkashanian, Prof. Derek Ingham, Prof. Lin Ma and Dr. Kevin Hughes for their strong support and help in providing sincere advices and knowledge. Many thanks for their encouragement and tremendous effort on my research study. Special thanks goes to Dr. Mohammed Ismail for his day-to-day guidance and always willing to help me, provide his best advices and useful discussions on how to proceed with my research. In addition, I offer my gratitude to my friendly fuel cell research group in this university especially to Mr. Dmitry Govorukhin and Mr. Paul Crosby for their technical assistance throughout my research.

I would also like to thank my parents and family who always support me through my ups and downs and encourage me with their best prayers. To my parents, who always support and believe in anything that I pursue, this work is for the both of you to be proud of. Special appreciation goes to my wife, Anizatul Azna who always motivates me to finish this journey despite the hardship that we face along the way. She always cheers me up, gave birth to our first child, Imad Aqel in my 2nd year of PhD and we are expecting our second child by the time I am finishing this journey. Those are great sacrifices that cannot be repaid.

Finally, I would like to express my gratitude to my sponsor, Majlis Amanah Rakyat (MARA) and to all my friends for their help and support.

ABSTRACT

Proton Exchange Membrane (PEM) fuel cells have a great potential to replace conventional fossil fuel dependent power conversion technologies in a wide range of portable, automotive and stationary applications and this is due to their high efficiency, quick start-up and sizing flexibility. However, there are still some technical challenges that hinder the widespread deployment of this clean technology into the marketplace. Two of the key challenges are the water management and thermal management of the fuel cell; any mismanagement of water and/or heat could lead to water flooding or membrane dry-out which are both detrimental to the fuel cell performance and durability.

In order to have insights on how to manage water and heat within the fuel cells, a transparent and commercially available PEM fuel cell has been directly visualised using high-resolution digital and thermal cameras at both sides of the fuel cell. With this technique, real-time videos that show how liquid water and heat evolve have been recorded. There has been a particular emphasis on how liquid water forms, accumulates and moves along the flow channels. Further, the sensitivity of the distribution of liquid water and temperature within the fuel cell to the operating conditions has been investigated. For this investigation, a new parameter, termed as the wetted bend area ratio, has been introduced to give an indication on how flooded the flow channels are and subsequently explain the variations in the performance of the PEM fuel cell as the operating conditions change. The main findings are the temperature distribution across the MEA becomes less uniform as the wetted ratio number decreases. Further, the temperature distribution along the MEA at the cathode side becomes less uniform as the air flow rate increases. In addition, there exist optimum values for the operating conditions to increase the fuel cell performance.

Since the operation of the PEM fuel cell at high temperatures (i.e.>100°C) is an increasingly adopted way to resolve water flooding problems, the reliability of the currently used components remain questionable. To partly answer this question, the gas permeability of the diffusion media used in PEM fuel cells has been investigated under higher temperatures for the first time. The results show that the gas permeability increases as the operating temperature increases and this may enhance the reactant transport within the PEM fuel cell.

CONTENT

LIST OF TABLES

LIST OF FIGURES

PUBLICATIONS AND CONFERENCES

Journal papers

1. **R. M. Aslam**, D. B. Ingham, M. S. Ismail, K. J. Hughes, L. Ma, and M. Pourkashanian, "Simultaneous direct visualization of liquid water in the cathode and anode serpentine flow channels of proton exchange membrane (PEM) fuel cells," *J. Energy Inst.*, pp. 1–14, 2017. **Chapter 4**
2. **R. M. Aslam**, D. B. Ingham, M. S. Ismail, K. J. Hughes, L. Ma, and M. Pourkashanian, "Simultaneous thermal and visual imaging of liquid water of the PEM fuel cell flow channels," *J. Energy Inst.*, pp. 1–8, 2018. **Chapter 5**
3. **R. M. Aslam**, D. B. Ingham, M. S. Ismail, K. J. Hughes, L. Ma, and M. Pourkashanian, "Effect of heat-treatment process on the through-plane gas permeability of GDL samples," **In preparation for submission to the International Journal of Hydrogen Energy. Chapter 6**

Conferences

1. "Visualization of liquid water in proton exchange membrane fuel cell: A progress report". Hydrogen Fuel Cell SUPERGEN Conference in the UK, University of Birmingham (December 12-14, 2014). Poster presentation.
2. "Simultaneous visualization of temperature and liquid water distribution in PEM fuel cells: A progress report". Energy Postgraduate Symposium by Energy 2050, The Doctoral Academy and The Grantham Centre for Sustainable Futures in the UK, University of Sheffield (November 20, 2015). Poster presentation.

NOMENCLATURE

Roman symbols

k	permeability, m^2
k	effective thermal conductivity, W/mK
L	thickness of porous medium, µm
P	pressure, Pa
Q	volume of flow rate, m^3/s
V	voltage, V
wt	weight of a sample, mg

Greek characters

μ	fluid viscosity of air flow, Pa.s
ρ	density, kg/m^3
π	Pi
Δ	math symbol for increment

Abbreviations

2D	Two-dimensional
3D	Three-dimensional
%RH	Percentage of relative humidity
AFC	Alkaline Fuel Cell
BD	Back Diffusion
BTU	British Thermal Unit
CPP	Clean Power Plan
DAFC	Direct Alcohol Fuel Cell
DMFC	Direct Methanol Fuel Cell

EIA	Energy Information Administration
EOD	Electro Osmotic Drag
ESEM	Environmental Scanning Electron Microscope
FCTS	Fuel Cell Test Station
GDL	Gas Diffusion Layer
GDM	Gas Diffusion Media
GHG	Green House Gases
MCFC	Molten Carbonate Fuel Cell
MEA	Membrane Electrode Assembly
MPL	Micro Porous Layer
NASA	National Aeronautics and Space Administration
OECD	Organization for Economic Cooperation and Development
PAFC	Phosphoric Acid Fuel Cell
PEM	Proton Exchange Membrane
PFSA	Perfluorosulfonic Acid
PTFE	Polytetrafluoroethylene
SEM	Scanning Electron Microscopy
SLPM	Standard Litre per Minute
SOFC	Solid Oxide Fuel Cell
TOD	Thermal-osmotic Drag
UNFCCC	United Nations Framework Convention on Climate Change
UK	United Kingdom
USA	United States of America

USD	United States Dollar
WEO	World Energy Outlook

Chemical symbols

e^-	Electron
CO_2	Carbon Dioxide
CO_3^{2-}	Carbonate ion
H_2	Hydrogen
H^+	Proton ion
H_2O	Water
K	Potassium
Li	Lithium
N_2	Nitrogen
Na	Sodium
O_2	Oxygen
O_2^-	Superoxide ion
OH^-	Hydroxide ion

CHAPTER 1

INTRODUCTION

1.1 ENERGY AT A GLANCE

Energy is important to the daily lives of human beings. From waking up in the morning until going to bed at night, much energy is consumed. With the increasing number of human beings in this world and the growing economy, this will result in an increasing amount of energy consumption. In 2008, the world's energy consumption was estimated to be 22 billion kWh yr^{-1} and will increase to 53 billion kWh by 2020 [1]. Further, a projection made by the International Energy Outlook 2013 regarding the world consumption of energy is of concern. They estimate that the energy consumption will grow by 56% between 2010 and 2040. This increasing pattern will be more significant in the non-OECD countries because of their growing economy, see Figure 1.1. Based on the same report, the industrial sector consumes the highest energy, which is 51.7%, followed by transportation 26.6%, residential 13.9% and commercial 7.8% [2].

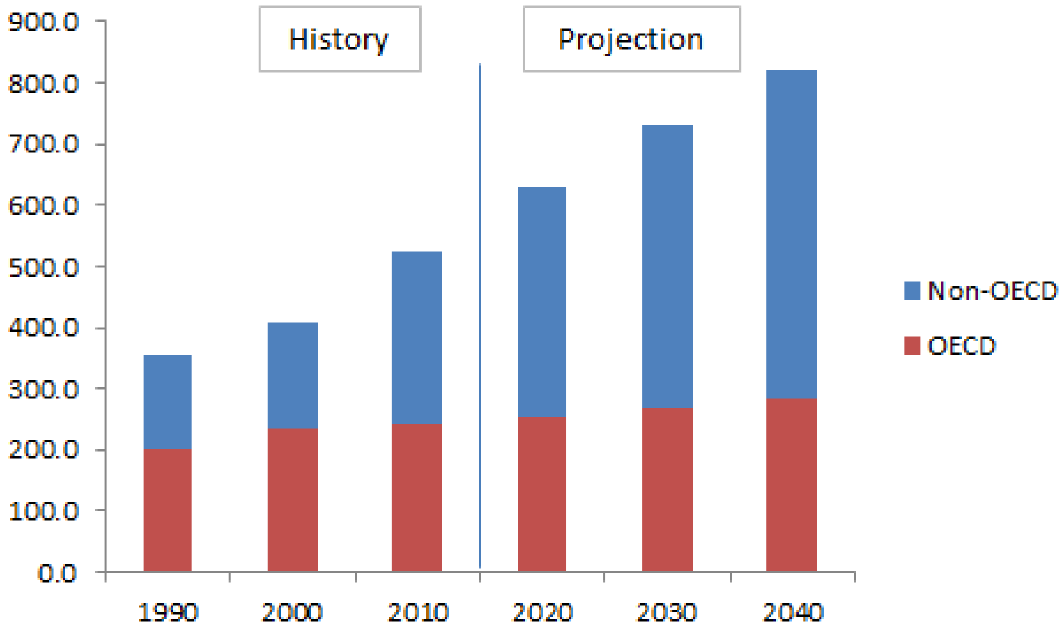

Figure 1.1: World energy consumption from 1990-2040 (quadrillion BTU) [2].

Fossil fuels, which consist of coal, natural gas and oil, account for 84% of the energy generated, see the World Energy Outlook (WEO) 2007 [3].This is worrying due to the energy crisis that the world has been confronted with. There are two main problems with the continued use of fossil fuels.

(i) The first problem is the limitation in the amount of fossil fuels supply. In 70 to 150 years in time, the fossil fuel reserves will be depleted. Up until now, the majority of energy is obtained from fossil fuels and does not depend much on other sources of energy. Figure 1.2 shows that the estimation of the world’s fossil fluid fuel demand will outstrip the world’s fossil fluid fuel production in 2015 [4].

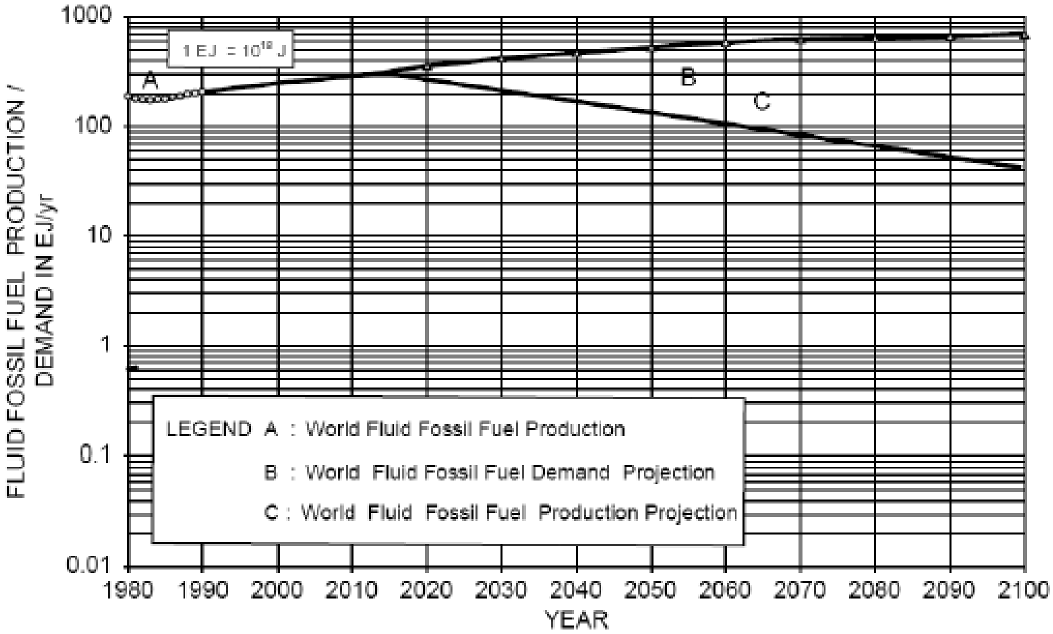

Figure 1.2: Estimation of world fluid fossil fuel production and demand [3].

The world will face an energy crisis unless a sustainable alternative fuel is available by 2015 and a fuel price hike will occur as a result of the crisis. From 1999 until now there has only been one occasion when the crude oil prices has fallen sharply and that was in the second half of 2008 and this was due to the global financial crisis. In 2011 and 2012, the average oil price per barrel was quite similar which were $111.26 and $111.67 respectively while compared to $79.45 per barrel in 2010 [5].

(ii) At the same time, climate change remains a serious concern. This is the second issue that is causing serious environmental problems. The continuous usage of fossil fuels generates Green House Gases (GHG) that causes global warming and climate change. The release of CO_2 into the Earth's atmosphere has been linked to global warming. Global warming is the warming of the Earth's surface due to the sun's rays and has been linked to the melting of the polar ice caps, which has been linked to ecological and environmental damage. In 2011, it is reported that the atmospheric CO_2 concentration was close to 390 ppm [6] and to record the high level of 400 ppm in 2013 [7]. It is estimated that the CO_2 concentrations in the atmosphere is increasing to as much as 600-1550 ppm in 2030 without climate change mitigation policies [7]. If this scenario is not stopped, numerous consequences will occur and this is actually happening at this moment of time. It is reported that the global mean temperature has increased by about 0.8 °C in the last century and half [8]. These global weather pattern changes will cause a disaster, such as floods and droughts in parts of the world. In the same report, it has been projected that on average a global warming of 1.1-6.4 °C, with a 2.8-7.8 °C warming in the Arctic, will occur by 2100 [8]. Further, the global temperature will keep on rising unless something is done to stop it.

Increasing social concern and awareness about climate change and exhaustible sources of fossil fuels has led to the need for alternative and renewable energy sources and carriers. Necessary steps need to be taken towards the development of new energy production technologies before the climate change becomes worsen. Venturing into sustainable energy production will also assist in solving the problem of fossil fuel depletion. Over the last few decades, the use of alternative energy conversion devices that are efficient, sustainable and environmental friendly have received much attention due to the increasing concerns in the growing power demand and global climate change.

Rising concerns in society is not sufficient to mitigate this problem. It must be translated into the form of a regulation. This is why the Kyoto Protocol, which regulates the reduction of GHG was established. The protocol is now becoming a binding international law when its ratification was approved by Russia and it came into force in 2005. It requires developed countries, including the United Kingdom (UK), to reduce their GHG emissions below the level specified for each of them in the treaty. It must be achieved within a five-year time between 2008 and 2012, and add up to a total cut in GHG emissions of at least 5% against the baseline of 1990 [9]. It was reported in DECC's 2011 statistics that the GHG emissions calculated fell by almost 28% from 1990 to 2009 [10]. The UK government is very committed to delivering on the Kyoto Protocol and it is continuing the effort by making the long term goal which is to reduce the carbon dioxide emissions by 80% of their 1990 level by 2050 [11].

Also, recent historic breakthroughs in international climate policy, namely The Paris Agreement [12], was negotiated by representatives of 196 parties and adopted by consensus in December 2015. Three major aims are described in Article 2, "enhancing the implementation" of the United Nations Framework Convention on Climate Change (UNFCCC) through;

a) holding the increase in the global average temperature to well below 2 ºC above pre-industrial levels and to pursue efforts to limit the temperature increase to 1.5 ºC above pre-industrial levels, recognizing that this would significantly reduce the risk and impacts of climate change,
b) increasing the ability to adapt to the adverse impacts of climate change and foster climate resilience and low greenhouse emissions development, in a manner that does not threaten food production, and
c) making finance flows consistent with a pathway towards low greenhouse emissions and climate-resilient development.

Alternative clean and renewable energy sources have become an important concern among energy providers and these have been explored in the last few decades. In addition, systems, which utilise wind, solar, hydrothermal and electrochemical energy, are emerging and developing. In 2011, 2% of the renewable energy sources have contributed to the world's total energy feedstock and by 2030, it is expected to increase up to 6% [13]. In another recent report by Energy Information Administration (EIA) [14], the renewable energy sources have become the world's fastest-growing energy source over the projection period between 2012 and 2040. Between 2012 and 2040, the consumption by renewable energy increases by an average of 2.6% per year as shown in Figure 1.3. Although the consumption of non-fossil fuels is expected to grow faster than consumption of fossil fuels, the fossil fuels still accounts to the largest portion of energy use in 2040 at 78% [14]. Hence, bigger and continuous contribution of renewable energy sources is required to tackle the issue with energy crisis and climate change.

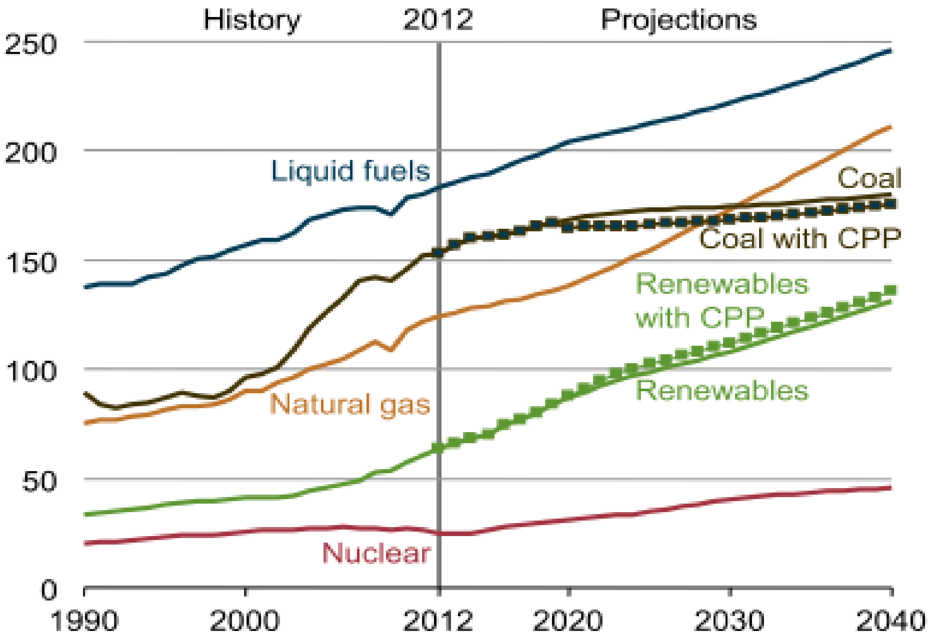

Figure 1.3: Total world energy consumption by energy source, 1990-2040 (quadrillion BTU) [14].

1.2 FUEL CELLS

Alternative sources of energy that are sustainable, environmental-friendly and efficient have become popular among researchers due to the increasing concerns regarding growing power demands and global environmental issues. One of the potential alternatives to fossil fuels is hydrogen [15]. Its high content of energy makes it a promising alternative source of energy in this century and the device that is always associated with hydrogen is the fuel cell.

A fuel cell is a device that generates electricity through a chemical reaction and it is considered by many to be the most promising energy conversion device. In fact, it can be converted into energy with a higher efficiency than the combustion of fossil fuels. This is because they are electrochemical engines and not heat engines and as such they are not subject to Carnot Cycle limitations [16]. Fuel cells combine fuel and oxidant electrochemically to produce electricity. They convert directly the chemical energy in the fuel into electricity directly without any combustion process. When pure hydrogen is used as the fuel, it gives zero pollution since it generates only water as the by-product. It operates in quite a similar manner to batteries in terms of converting chemical energy directly into electrical energy. However, the difference is that the fuel cell is an open system device that makes it able to continuously produce electrical power as long as the reactants are supplied. In contrast, for batteries the energy is produced is limited due to the amount of reactant stored in the device.

Sir William Grove invented the first fuel cell in 1834 by reacting oxygen and hydrogen on separate platinum electrodes that were immersed in dilute sulphuric acid inside five cells of a gas voltaic battery and used the current produced to electrolyse the water in another similar cell. However, the fuel cell could not compete with the dynamo, which was invented by von Siemens, due to its inefficient performance [4]. There were several attempts made in order to improve the efficiency of this new technology to invent a practical fuel cell and it was not until the 1960s that the first practical fuel cell was developed by General Electric with the purpose to be used by NASA in their space missions. It consisted of two porous electrodes which are lightly catalysed on one surface, bonded on either side of a thin sheet of a hydrogen ion conducting polymer, the solid polymer electrolyte [17]. However, according to Warshay et al. [18], the first practical fuel cell was invented in 1932 by Bacon. A 5 kW hydrogen-oxygen alkaline electrolyte system was capable of powering a welding machine, a circular saw and a two-ton forklift truck. The development of the fuel cell technology has been expanding year by year and to date there are a wide variety of fuel cells that have been developed.

Fuel cells are usually classified by the electrolyte used in the cell. There are alkaline fuel cells (AFC), phosphoric acid fuel cells (PAFC), molten carbonate fuel cells (MCFC), proton exchange membrane fuel cells (PEM fuel cell), direct alcohol fuel cells (DAFC) and solid oxide fuel cells (SOFC). The first three fuel cells have been well developed and have reached their maturity, while the three later fuel cells are the most extensively studied fuel cells today and there are a large number of issues that need resolving before they are in a strong position to be commercialized.

The first type of fuel cell that has been investigated and put into applications is the alkaline fuel cells (AFC) [19]. In 1950, the first experiment with vehicular application based on AFC was applied. Later on, NASA has developed the AFC for the Apollo Program. In the AFC, it uses potassium hydroxide as the electrolyte to allow the ions flowing between the electrodes. However, due to the rapid development of PEM fuel cell, the AFC has fallen out of favour within the research community.

Meanwhile, the phosphoric acid fuel cell (PAFC) was first installed in 1970s [20]. In fact, more than 500 PAFC power plants have been installed and tested around the world since then. As its name implies, it uses the liquid phosphoric acid as the electrolyte. However, since 2000, the numbers of PAFC in the market has slowed down due to economic and technical challenges and more attention has been shifted to other fuel cell technologies.

Molten carbonate fuel cells (MCFCs) use an eutectic mixture of lithium and potassium carbonates as the electrolyte. Development started in 1960 when Broers and Ketelaar reported a high temperature fuel cell which employed an electrolyte comprising a mixture of alkali metal carbonates constrained within a disc of magnesium oxide [21]. MCFC does not require an external supply of hydrogen as do the AFC, PAFC and PEM fuel cells. Its high operating temperature, i.e. 600 to 700 °C converts the fuels to hydrogen within the fuel cell itself. The main issue in the MCFC technology is its durability. Due to the high operating temperature and the corrosive electrolyte used, the durability of the components and materials of the fuel cell becomes a problem and thus decrease the fuel cell life.

Direct alcohol fuel cells (DAFCs) are similar to PEM fuel cells where the fuel is fed into the fuel cell and uses the proton exchange membrane as the electrolyte. There are a few alcohols such as ethanol, ethylene glycol and propanol, which have been considered for use in DAFCs but methanol is the most promising organic fuel due to its advantages. However, there are very few DAFCs that have been demonstrated with Direct Methanol Fuel Cell (DMFC) being the most advanced system [22]. Nonetheless, due to high permeation of methanol through the

PEM electrolyte, i.e. methanol crossover, the current efficiency has become the main problem regarding DMFC [23].

Solid oxide fuel cells (SOFCs) use a metal oxide (stabilised zirconia) as the electrolyte and operate at temperatures as high as 1000 °C. The first operation of ceramic fuel cells at 1000 °C was performed in 1937 by Baur and Preis [24]. Since then, the development of SOFC has accelerated. However, the challenges involving SOFCs are mainly on the relatively slow start-up and response to step changes in demand that are essential in high temperature devices and the fuel cell life. As SOFCs operate at high temperature, the durability of the components of the fuel cell also becomes an issue and exerts many constraints on the selection of materials for the components of the fuel cell. Recent developments to solve these issues, such as the material selection and reduction in the operating temperature down to ~300-400 °C, are still in progress [25].

Further, each type of fuel cell is suited for different applications and these can be summarized into three major applications, namely transportation, portable devices and stationary power generation. In addition, fuel cells can be categorized by the operational temperature. There are low and high temperature fuel cells. AFC, PAFC, PEM fuel cell and DAFC lie in the low temperature fuel cell range while MCFC and SOFC lie in the high temperature fuel cell range. Table 1.1 summarizes the type of fuel cells according to the electrolyte used and operating temperature.

In this thesis, the PEM fuel cell is the main focus due to its characteristics and enormous potential in bringing the fuel cell industry to the next level of commercialisation. In 2015, Toyota Motor Corporation launched the world’s first mass-produced hydrogen fuel cell vehicle, the Toyota Mirai after more than 2 decades of thorough research and rigorous testing [26]. However, after two years hitting the roads, in 2017, the Toyota Mirai was recalled due to problems with the output voltage generated by their fuel cell system [27].

Table 1.1: Summary of the types of fuel cells.

Type	Electrolyte	Ion	Operating temperature (°C)
AFC	Potassium hydroxide	OH^-	Low (90-100)
PAFC	Liquid phosphoric acid	H^+	Low (150-200)
MCFC	Lithium/potassium carbonate	CO_3^{2-}	High (600-700)
PEMFC	Proton exchange membrane	H^+	Low (50-100)
DAFC	Proton exchange membrane	H^+	Low (20-90)
SOFC	Stabilized zirconia	O_2^-	High (700-1000)

1.3 RESEARCH MOTIVATION

As the PEM fuel cell is considered as the potential solution to the environmental and energy problems and it is expected to become a most promising energy converter for automotive, stationary and portable applications, it is vital to understand the operation of the PEM fuel cell and solve any issues that can stop this development and expectation to become a reality. One of the major issues related to the PEM fuel cell is water management, with almost every component in the PEM fuel cell being related to this issue. Hence, a good understanding of the operation and what occurs in each component is required to achieve a solution to the problem.

1.4 RESEARCH OBJECTIVES

There are three main objectives of this research. Firstly, to investigate the water management in PEM fuel cells under different operating conditions. This thesis focuses on the performance and visualization of the water behaviour in the gas channels of PEM fuel cells. Another objective of this research is to investigate the temperature distributions in PEM fuel cells under different operating conditions in order to improve the performance of the PEM fuel cell. Finally, to investigate the gas permeability of the GDL under high temperature conditions in order to ensure the possibility of high temperature membrane development for the high temperature PEM fuel cells.

1.5 RESEARCH METHODOLOGY

Experimental techniques are the main methods that can achieve the objectives. The principles and methods that are employed in this research are based on the in-house fuel cell test facility. Several parameters in the operating conditions, such as gas flow rate, gas relative humidity and operating pressure are used to investigate the effect of these parameters on the water management within the cell. A commercial transparent PEM fuel cell from Pragma Industries, ClearPak Single Cell is used to carry out the experimental investigations. It is designed in order to have a clear visualization of the gas flow field channel through the end plate. This is helpful in analysing the water behaviour and gives a good understanding in how to manage the water in the PEM fuel cell. In addition, a mechanical modification on the commercial PEM fuel cell is performed in order to allow infrared visualization by a thermal camera over the MEA surface inside the PEM fuel cell.

1.6 THESIS OUTLINE

This thesis is divided into 7 chapters. Chapter 1 is an introduction on energy and some general information related to the thesis. Also it provides the history of the fuel cell and different types of fuel cells as an alternative source of energy. This is followed by an explanation of the motivation, objectives and methodology of the thesis.

Chapter 2 is a literature review on the design and components of the PEM fuel cell. It also contains an explanation of the operation of the PEM fuel cell. The review also focuses on the experimental works that are related to the main issue of the thesis, namely water and thermal management. The review on the gas permeability of the gas diffusion layer is also included in this chapter.

Chapter 3 describes the specifications of the in-house fuel cell test facility. The experimental techniques, including the procedures, methods and materials used, are presented. In addition, the visualization techniques that are employed are also explained in these chapters.

Chapter 4 is the main chapter of the experimental investigation. It describes the experimental investigation on the PEM fuel cell, which is the effect of the operating conditions on the water management by visualizing and analysing the water distributions respectively. A quantitative and qualitative analysis is discussed with regards to the effect of several operating conditions on the liquid water accumulation inside the PEM fuel cell.

Chapter 5 is another main chapter on the experimental investigation involving water and thermal management. The water and temperature distributions inside the PEM fuel cell is visualized and discussed under different reactant flow rates.

Chapter 6 discusses the ex-situ experimental investigation on the gas permeability of GDLs under a high temperature condition. The chapter introduces the research advancements in PEM fuel cells that involve the high temperature PEM fuel cell to obtain further insights in the water management problem.

Chapter 7 concludes the contributions and the knowledge that is obtained in this thesis from the experimental investigations discussed and performed in Chapters 4 to 6. Further, in this chapter some suggestions of possible future investigations that may be potentially performed as a continuity and coherency of this thesis are presented for the development of the PEM fuel cell technology.

CHAPTER 2

LITERATURE REVIEW

Fuel cells have a great potential to replace conventional fossil fuel dependent power conversion technologies with an increasing trend towards reduction of emissions and higher efficiency power generation. One of the most common and has a wide range of applications, e.g. portable, automotive and stationary, is the PEM fuel cell. This is due to their high efficiency quick start-up and sizing flexibility [28]. Due to their capability of providing a wide range of energy (from a few watts to the MW range), they have been attractive sources of energy for a wide range of portable and mobile applications. In this investigation, a literature review on the PEM fuel cell has been presented and discussed in the PEM fuel cell area and has been focused on the water and thermal management, operating conditions and gas permeability. The main purpose of the review is to gather ideas on how to improve and expand the experimental testing of the PEM fuel cell.

In this chapter, Sections 2.1-2.2 provide a brief review of the PEM fuel cell in term of its introduction, the advantages and disadvantages and operation. This is followed by a general review of all the components of the PEM fuel cell in Section 2.3.

In Section 2.4, a review on the water management in PEM fuel cells is discussed in terms of water transportation and visualization. This is followed by a review on the thermal management in PEM fuel cell in Section 2.5. Next, a literature review on the operating conditions related to water and thermal management investigations are discussed in Section 2.6. Further, a literature review on through-plane gas permeability in gas diffusion media is presented in Section 2.7. Finally, Section 2.8 concludes this chapter by highlighting the impact of this research in order to expand the knowledge in the PEM fuel cell technologies.

2.1 OVERVIEW OF THE PROTON EXCHANGE MEMBRANE FUEL CELL (PEM FUEL CELL)

In the 1960s, the proton exchange membrane, or polymer electrolyte membrane (PEM) was called a solid polymer electrolyte fuel cell. It has become the most promising and most widely researched type of fuel cell due to its great potential. As a result, there have been significant improvements in the PEM fuel cell technology which mainly have been capitalized in the increased performance, the durability and the reduction of the cost per kilowatt of the power produced [29]. Further, it has a low operation temperature, has a high efficiency, has a quick start-up and has a high power density compared to the other types of fuel cells. The PEM fuel cell can start quickly due to the low operation temperature and the advantages of the PEM fuel cell are that there are no corrosive fluid hazards and the cell can work in any orientation. This means that the PEM fuel cell is particularly suitable for use in vehicles and in portable applications. Furthermore, it is simple and easily combined into stacks of fuel cells to produce higher power outputs. As mentioned in Section 1.2, fuel cells are an emerging technology which can be applied in transportation, portable devices and smaller stationary power generations. It has already been demonstrated in numerous applications, such as automobiles, buses, scooters, bicycles, golf carts, fork lifts, airplanes, locomotives, boats, underwater vehicles, distributed power generation, cogeneration, back-up power and portable power [30].

The PEM fuel cell has a large specific power and it is flexible to scale the power output over a wide range, from a few watts to hundreds of kilowatts. However, the commercialization of the PEM fuel cell has still not occurred widely and this is mainly due to the high cost of production. It is predicted that the cost of mass produced PEM fuel cell will be ~70 USD/kW and this is more than double the cost of the production of current automobile internal combustion engines [31]. The reduction in cost can be in many ways, such as the reduction of the amount of noble-metal catalyst used, improving the power output by optimization of the operating conditions of PEM fuel cell, i.e. water and thermal management and the development of enhanced and cost-effective component materials. In this thesis, emphasis is placed on addressing the latter two issues.

2.2 ELECTROCHEMICAL REACTIONS IN PEM FUEL CELL

The electrochemical reactions in a PEM fuel cell occur simultaneously on both sides of the anode and the cathode in a similar manner as to what occurs in the other types of fuel cells. The following anodic and cathodic reactions take place, respectively:

$$\mathbf{H_2 \rightarrow\ 2H^+ +\ 2e^-} \tag{2.1}$$

and

$$\mathbf{2H^+ +\ 2e^- + \frac{1}{2}O_2 \rightarrow\ H_2O} \tag{2.2}$$

Overall:

$$\mathbf{H_2 + \frac{1}{2}\ O_2 \rightarrow H_2O + heat} \tag{2.3}$$

At the heart of a single PEM fuel cell is a polymer membrane that has some unique capabilities. It conducts protons from the anode to the cathode but at the same time it is impermeable to gases. The two porous electrically conductive electrodes squeeze the membrane, which acts as the electrolyte between them. Typically, the electrodes are made from carbon cloth or carbon paper. There is a catalyst layer for each of the anode and the cathode at the interface between the porous electrode and the polymer membrane. Currently, the most common catalyst used in a PEM fuel cell is platinum. Next to the catalyst layer is the GDL that acts as a supporting material in the membrane electrode assembly (MEA). The gas diffusion layer (GDL) are porous materials composed of a dense array of carbon fibres, which also provide an electrically conductive pathway for the current collection. The assembly of the GDL, the catalyst layers and the membrane is called the MEA. A schematic diagram of a single PEM fuel cell configuration is shown in Figure 2.1.

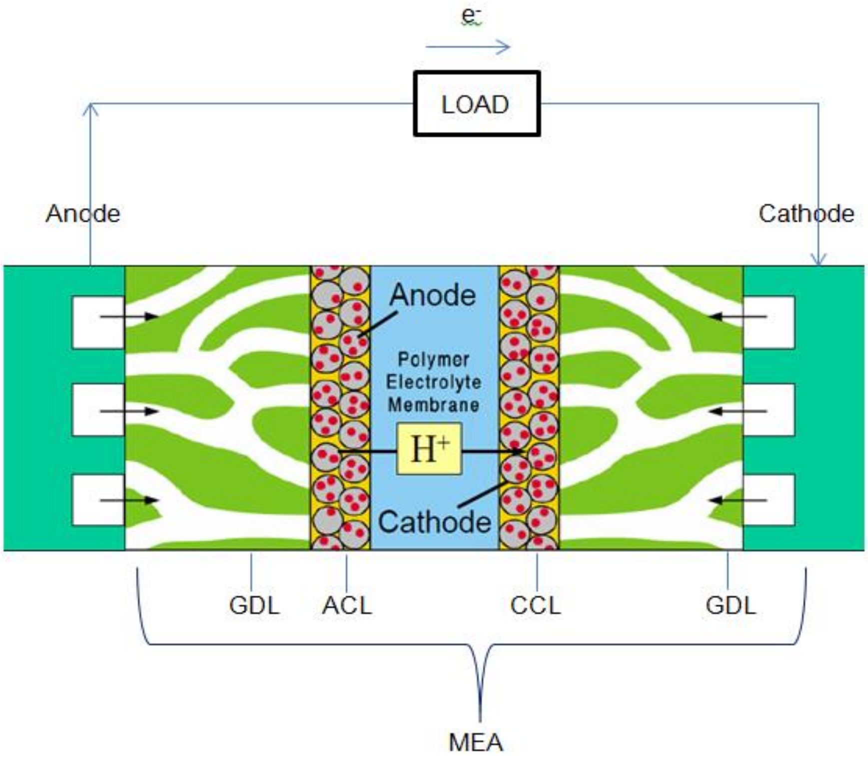

Figure 2.1: A schematic diagram of a single PEM fuel cell configuration.

Whenever hydrogen is fed to the anode gas distributor plate, it is distributed over the surface of the GDL. Then it diffuses into the catalyst layer and splits into its primary constituents, protons and electrons and this reaction is catalysed by the platinum. Each hydrogen atom consists of one proton and one electron. The protons travel through the membrane to the cathode while the electrons flow through the electrically conductive electrode, through the current collector and through the external circuit of the PEM fuel cell and travel to the other side of the membrane and hence produces the electric current. At the cathode catalyst side, the electrons meet the protons that have travelled through the membrane. At the same time, the air or oxygen gas is fed to the cathode gas distributor plate and then flow through the GDL and the catalyst layer at the cathode. The electrons then meet the protons that have travelled through the membrane and they react with the oxygen. As a result, water is created in the electrochemical reaction as shown in equation (2.2).

2.3 COMPONENTS OF THE PEM FUEL CELL

As shown in the Figure 2.1, a single PEM fuel cell is comprised of a MEA, which consists of a membrane, two catalyst layers and two gas diffusion layers (GDL) and two distributor plates or often known as bipolar plates in a fuel cell stack. Each of these components plays a vital role in the performance of the PEM fuel cell.

Numerous researchers have reviewed and analysed the design and manufacture of the PEM fuel cell. Litster and McLean [32] have reviewed and investigated the design of the PEM fuel cell electrodes to achieve a better performance of the PEM fuel cell. They found that the most common form of electrode is that featuring a thin-film catalyst layer. Mehta and Cooper [33] also made an in depth review on the PEM fuel cell design and manufacture, focusing on the MEA components and bipolar plates and performed an analysis within the context of vehicle applications.

2.3.1 Membrane Electrode Assembly (MEA)

Again, the MEA is a combination of five layers that consist of one membrane, two catalyst layers and two gas diffusion layers. However, practically it requires another two sets of sealing gaskets, thus making it seven layers, see Figure 2.2. Each layer of the MEA performs a unique role and this is now described. Also, some MEA include a micro-porous layer (MPL) which is inserted between the GDL and the catalyst layer. The MPL has been found to enhance the performance of the PEM fuel cell.

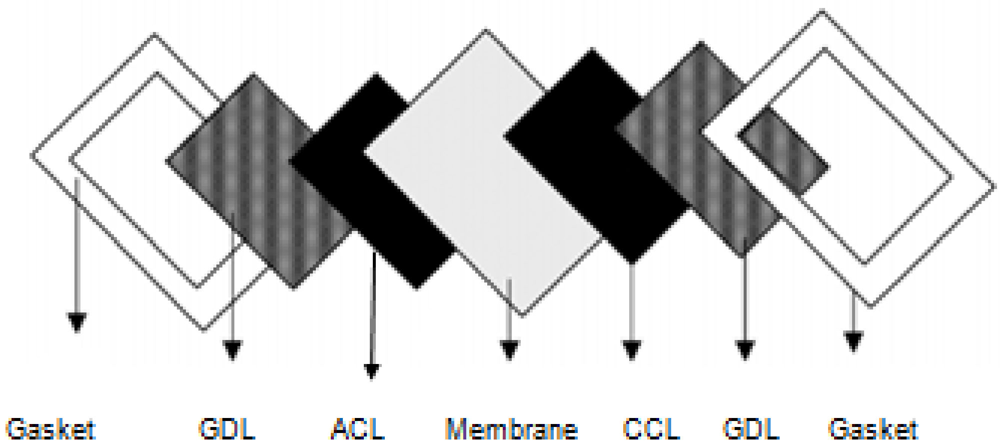

Figure 2.2: A schematic diagram of a MEA.

2.3.1. (a) Membrane

The membrane has several specific functions. It must exhibit relatively high proton conductivity and present an adequate barrier to the mixing of the fuel and reactant gases and it must be chemically and mechanically stable in the fuel cell environment [16]. Further, the proton conductivity of a membrane is strongly dependent on the membrane structure and its water content.

The most common material used for the membrane is perfluorosulfonic acid (PFSA), as suggested by Gottesfeld and Zawodzinki [33]. Many PFSA membranes are commercially available from several manufacturers, such as DuPont, Gore, Asahi Glass, Asahi Kasei, Solvay and 3M [34]. There are two major advantages of using PFSA membranes, namely the strength and stability in both oxidative and reductive environments and the high proton conductivity. When the membrane becomes hydrated, the protons become highly mobile. Therefore, the thickness of the membrane needs to be carefully chosen to have a lower internal resistance and also a lower reactant crossover. A higher resistance results in a lower power density and a higher reactant crossover results in a decrease in the fuel utilization.

2.3.1. (b) Anode and cathode electrode

The anode and cathode electrode are essentially a thin catalyst layer pressed between the ionomer membrane and it is a porous, electrically conductive substrate and it is the location where the electrochemical reactions occur [16]. The electrodes have to be porous to gas diffusion in order to ensure the supply of the reactant gases to active sites where the noble metal catalyst is in contact with the ionic and electronic conductor.

The best catalysts for both electrodes are platinum, despite the fact that a huge variety of non-noble metal catalysts have been investigated [35]. In the early stages of PEM fuel cell developments, platinum was used in quantities as large as 28 mg cm^{-2} and this high usage of platinum has led to the myth, and it is still widely held, that the major factor in the cost of a PEM fuel cell is due to the platinum [36].

However, recently the high usage of platinum has been reduced to about 0.2 mg cm^{-2} and yet with the power increasing [36].

The main requirement of a good electrode is a three-phase boundary. This is because there are three kinds of species that participate in the electrochemical reactions, namely the gases, electrons and protons [16].

2.3.1. (c) Gas diffusion layer

The gas diffusion layer (GDL) in a PEM fuel cell is sandwiched between the catalyst layer and the gas flow channel, see Figure 2.1, and its structure controls the catalyst utilization and the overall cell performance [37]. Although the GDL does not directly participate in the electrochemical reactions, it has several important functions. The main functions of a GDL are to collect the current, remove the heat and water from the MEA, allow the gas transport towards the catalyst layer and provide a physical support for the catalyst layer. It is one of the most vital components, acting both as the functional as well as the support structure for the MEA in the PEM fuel cell [38].

Because of the several important functions, the GDL possess specific requirements to perform the functions, namely; it must be

I. sufficiently porous,
II. electrically and thermally conductive, and
III. sufficiently rigid to support the MEA.

As mentioned by Escribano et al. [39], it is difficult to balance all the specific requirements in order to perform all the functions of the GDL. For example, to increase the air and water permeability then the porosity must be higher but at the same time these results in a lower strength, and electrical and thermal conductivity.

The GDL play a vital role in water management, and must strike a fine balance between water removal and membrane hydration. It is commonly treated with a hydrophobic coating of polytetrafluoroethylene (PTFE) to enhance the liquid water removal from the fuel cell. Also it is typically wet-proofed in order to ensure that the liquid water does not clog the surface and the pores in the GDL and hence it will not impede gas transport to the catalyst layer [37].

2.3.1. (d) Micro-porous layer

The MPL with an average pore size in the range of 10-100 nm is placed adjacent to the catalyst layer and normally made of carbon black powder and PTFE particles. Several researchers have investigated the role of the MPL with respect to water management in PEM fuel cells. There are numerous different experimental groups that have shown that the use of MPLs normally improves the performance of the fuel cell; however, there is not yet agreement among the researchers on the reasons behind this improvement [40]. However, the reasons could be categorised in terms of the microporosity of the MPL [41]–[46], reduced water saturation [47]–[57], promoted back diffusion process [31], [40], [58]–[62], promoted removal of water to the flow field channel [63]–[65], reduced the number of water breakthroughs [66]–[68] and unrelated to water transport [69], [70].

Wilson et al. [41] found that the MPL is required if the fuel cell are to be operated under well-humidified conditions (70% RH). This is due to the presence of relatively small pores compared to those of the macroporous carbon paper. These small pores assist in preventing the formation of water droplets and consequently reduce the mass transport resistance. On the other hand, they found that severe flooding occurs in macroporous carbon paper which substantially feature larger pores, e.g. of the order of 30 µm. Similar findings have been reported by Qi et al. [42]. With smaller pore size, water may not be able to form stable droplets in the MPL due to higher capillary pressure and therefore the latter layer is less likely to be flooded [42]. Passalacqua et al. [43] found that the power density of the PEM fuel cell was improved by almost 57% by introducing the MPL. Also, Wilson et al. [41] and Qi et al. [42] attributed this improvement to the presence of relatively small pores in the MPL. In addition, they reported that the applied MPL increases the limiting current density and reduces the ohmic losses. Kong et al. [45] investigated the influence of pore-size distribution in the MPL on the mass-transport in PEM fuel cells. A pore former and heat treatment was employed to modify the microstructure of the MPL. They found that the pore-size distribution has a greater influence on the cell performance compared to the total porosity. The microporosity of the MPL has been agreed by few researchers that it prevents the formation of the water droplets and hence less likely to be flooded. However, the microporosity of the MPL restricted the gas transport of air (since generally it is applied only at the cathode side) to the reactant sites and this leads to the mass transport limitation.

Hirano et al. [47] showed that an extremely thin MPL layer (1 µm) resulted in an enhanced cathode performance and this was attributed to the resulting minimal mass transport resistance in the high current density region. Similar findings have been reported by Malevich et al. [48] through the employment of electrochemical impedance spectroscopy (EIS) measurements. They attributed this to the reduced water saturation in the GDL and consequently improved oxygen transport to the cathode catalyst layer. A similar observation was found by Kim et al. [49] through using a similar measurement technique. In addition, they reported a negative value of the net water-drag coefficient in the presence of the MPL, thus indicating that the water is transported from the cathode to the anode side, which justifies the reduction of the liquid saturation in the cathode GDL. Meng [57] developed a multi-dimensional two-phase PEM fuel cell model to study the liquid water transport across the different porous materials including the MPL. He showed that the liquid water saturation possesses the lowest value inside the MPL. Also, he reported that the liquid saturation in the catalyst layer without the MPL is slightly lower than that with the MPL. He concluded that the MPL acts as a barrier for the liquid water transport on the cathode side of the PEM fuel cell.

Weber and Newman [40] found that, through simulation works, the MPL largely keeps water away from the cathode GDL and forces it to move towards the anode by back diffusion. The reason behind this is that the MPL causes a higher liquid pressure due to its lower permeability (owing to the smaller and more hydrophobic pores of the MPL). Ultimately, this results in a better membrane humidification and a reduced level of water flooding. In another investigation, Pasaogullari et al. [62] found that there is an increased tendency of water to flow towards the anode by permeation with the presence of MPL. This is due to the strong capillary pressure of the MPL and the increased resistance to liquid water removal from the cathode towards the GDL, which establishes a higher pressure differential across the membrane. They also found that the water flux towards the anode is improved with MPLs of smaller pore size and lower porosity. Spernjak et al. [60] employed a transparent fuel cell to study the effect of MPL. They observed that liquid water appeared in the anode gas channel when the MPL was placed only at the cathode side. They attributed this to the presence of the cathode MPL that enhances back diffusion. Also, they reported poor performance for the fuel cell running with bare GDLs and they attributed this to the incapability of the GDL to push water towards the membrane, resulting in the dehydration of the latter.

Nam and Kaviany [63] studied the effective diffusivity and water saturation distribution in the GDL with and without MPL at the cathode side by employing a half-cell model. They found that the MPL decreases the liquid water saturation in the catalyst layer and assists in removing liquid water from the catalyst layer to the cathode GDL. They attributed this to the higher capillary pressure that arises because of the smaller permeability of the MPL. Similar findings have been obtained through an experimental investigation by Park et al. [64] and Pasaogullari et al. [65].

Nam et al. [66] investigated the roles of MPL in the pore water control in PEM fuel cells. An environmental scanning electron microscope (ESEM) is used to visualise the vapour condensation and liquid water breakthrough in the porous layers. They found that in the absence of the MPL, large droplets and high liquid saturation present at the interface between the catalyst layer and GDL. Meanwhile, in the presence of the MPL, the droplet size, as well as the liquid saturation, reduces and this is due to the relatively smaller pores of the MPLs. Also, the MPL reduces the number of liquid water breakthrough towards the GDL and therefore reduces the liquid water saturation in the GDL and improves oxygen diffusion. Similar findings have been reported by Gostick et al. [67].

Atiyeh et al. [69] attempted to determine whether, how and to what extent does the MPL at either electrode or at both electrodes affect the water transport in fuel cells. They placed MPLs at both and either electrodes of a fuel cell and the net drag coefficient was determined from the water balance measurements. They found that the addition of the MPL at both or either electrodes did not cause a significant change to the overall drag coefficient but exhibited better overall performance and durability compared to without an MPL. Hence, they concluded that the enhanced performance of the PEM fuel cell is not associated with the overall water drag as has been reported by other researchers. However, as mentioned by them in their report, the correlation between the cell performance and water transport cannot be determined and requires further investigation. The non-influence of the MPL on the water balance was also reported by Thomas et al. [70]. From their experimental works, they reported that the presence of the MPL has an effect on the electrodes temperature by adding a thermal resistance and the performance of the fuel cell but not on the water balance.

2.3.1. (e) Sealing gasket

The sealing gasket is a small component of the MEA but it is a very important component for a PEM fuel cell. The gasket provides the correct compression when the fuel cell is assembled and prevents any potential fuel leak, which would reduce the overall efficiency. The thickness of the gasket and the degree to which it is being compressed affects the thickness and the porosity of the GDL and hence influences the overall performance of the PEM fuel cell [71].

According to Ghosh [72], the dimensional mismatch between the gasket and the GDL produces a significant impact on the overall performance of the PEM fuel cell. The mismatch may lead to several problems, such as gas leakage and increase in contact resistance in the cell due to the poor contact between the bipolar plate and the GDL. A recent review of the sealing structures has been reported by Ye et al. [73] and they concluded that it is a key factor affecting the electrical output performance and the security of the fuel cells.

2.3.2 Gas distributor plate

One of the most important components in a PEM fuel cell is the gas distributor plate, or sometimes known as the bipolar plate in fuel cell stacks. The main function of the plate, as the name implies, is to distribute the reactant gases into the electrode. In addition, it also acts as the current conductor between the cells, supports the MEA structure, removes the water from the fuel cell, humidifies the reactant gases and separates the cells inside a fuel cell stack. On the plate, a flow channel, or commonly known as a flow field channel, is grooved to provide the pathway for the reactant gases and also the by-products of the reactions. There are several types of flow field channels with different patterns and shapes, such as the parallel, serpentine and interdigitated. Li et al. [74] have reviewed in depth several flow field designs with each of them having pros and cons and being suitable for different applications.

As the plate significantly contributes to the volume, weight and cost of the PEM fuel cell, numerous researchers have investigated suitable materials for the plate, such as non-metals, metals and composites. Currently, the most common material used to manufacture the plate is graphite. This is due to the graphite’s high corrosion resistance and good surface contact resistance. However, graphite on the other hand suffers weak mechanical strength and brittleness that leads to the bulky use of graphite. In addition, to groove the flow field channel on the graphite plate consumes a high cost of machining. Due to the drawbacks associated with the use of graphite, metallic materials have received much attention for their use in the manufacture of the plate. A review by Hermann et al. [75] provides an overview of the materials and their characteristics and concludes that more research needs to be performed on the metals and composites in order to replace the most commonly used material, which is graphite, as they are yet to attain the long-term reliability and power densities achievable by non-porous graphite.

2.4 WATER MANAGEMENT IN PEM FUEL CELL

As mentioned in Section 1.2, the PEM fuel cell has a very large potential in bringing the fuel cell industry to the next level. However, there are some very important issues that need to be resolved in order for the PEM fuel cell to be commercialized, such as cost, durability and water management. The high performance and efficient operation of a PEM fuel cell relies on the water management in the cell. To ensure high proton conductivity, the membrane needs to be fully hydrated while at the same time it is important to remove the excess water generated at the cathode to avoid the flooding of the catalyst layer and the GDL.

Water needs to be balanced within a PEM fuel cell in order to meet the conflicting requirements of membrane hydration and cathode anti-flooding [31]. Excessive water at the cathode catalyst layer impedes the oxygen transport to the active sites and this results in an increased mass transport limitation which is demonstrated by the lowering of the limiting current densities. This can lead to fuel starvation and severe performance losses. In addition, depending on the humidification level of the reactant feed streams, localized drying of the membrane can occur and this leads to excessive ohmic heating and ultimately to a pinhole formation in the membrane [69]. Thus, it is one of the crucial issues in the operation of a PEM fuel cell because it does not only compromise the fuel cell performance but also it contributes to a rapid degradation of the MEA in a PEM fuel cell. Water plays interesting roles which are favourable for proton delivery and adverse to mass transfer [76]. In order to improve the water management in PEM fuel cells, it is vital to have a good understanding on the transportation and the balancing of the water within the PEM fuel cell.

Water flooding can occur by the inefficient operation of the PEM fuel cell. As shown in equation (2.2), the end product of the reaction at the cathode side is water. If the water removal rate does not keep up with the generation rate, then excessive water will accumulate. This causes water flooding and thus hindering the transport of oxygen by blockage of the pores in the porous cathode catalyst layer and the GDL covering up the active sites in the catalyst layer and the plugging of the gas transport channels in the flow field [77]. As a result, the reactants will be non-uniformly distributed over the active catalyst site and this will make the cell performance unpredictable, unreliable and unrepeatable under identical operating conditions. Meanwhile, if the water removal exceeds the water generation rate, the membrane will dehydrate and this will result in the poor performance of the cell due to significant ohmic losses within the cell.

Due to these complicated issues, the water management in a PEM fuel cell has attracted the attention of numerous researchers from all over the world because it is a fundamental issue limiting of the performance of the PEM fuel cell. Studies on this topic, as reviewed by Li et al. [77], have ranged from numerical simulations and modelling, to experimental investigations and diagnosis with an objective to develop a thorough understanding of the problem, and hence deduce mitigation strategies by manipulating the operating conditions.

2.4.1 Water transportation in PEM fuel cell

There are several water transport mechanisms in PEM fuel cell, with two major mechanisms, namely the electro-osmotic drag (EOD) and the back diffusion

(BD). EOD occurs whenever the proton is transported from the anode to the cathode side. The number of water molecules dragged by each proton can be determined by the EOD coefficient and due to the EOD effect, the membrane close to the anode side may dry out quickly [78].

Meanwhile, back diffusion transports the water molecules from the cathode side to the anode side and it is driven by the water concentration gradient. The water molecules diffuse through the membrane with each proton being investigated by using several methods which have been summarized by Wei Dai et al. [76] as follows; flow permeation and sorption, water flux measurement, streaming potential and nuclear magnetic resonance.

Apart from EOD and BD, the water can be transported from the cathode to the anode and vice versa when certain conditions occur, such as high temperatures (>80 °C) or high backpressures are applied within the PEM fuel cell and then the water will travel through thermal-osmotic drag (TOD) and the pressure driven hydraulic permeation, respectively. A schematic of the water transport mechanism is shown in Figure 2.3.

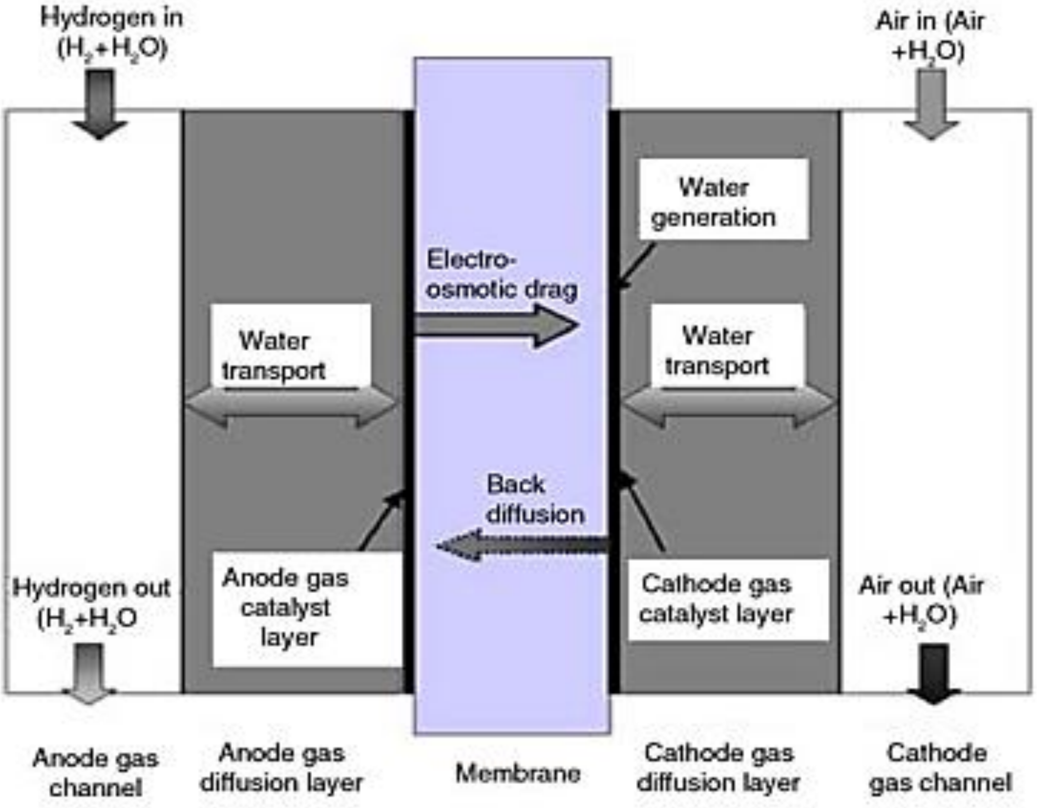

Figure 2.3: Schematic of the water transport mechanisms in PEM fuel cells [79].

Yan et al. [79] have performed an investigation on the water balance in a PEM fuel cell by measuring the net drag coefficient under various conditions and also they investigated the effects of the water balance on the cell performance. The results obtained showed that the net drag coefficient of water through the membrane depended on the current density and humidification of the feed gases. Apart from that, they also found that the humidity of both the anode and cathode inlet gases had a significant effect on the cell performance.

2.4.2 Water visualization technique

It is essential to study the water behaviour inside the PEM fuel cell in order to have a better understanding of the problem and this leads to the solution of the water management in a PEM fuel cell. In order to study the water behaviour, a visualization process has to be performed and there are several visualization techniques that can be applied to study the water behaviour inside the PEM fuel cell.

A review by Bazylak [80] has provided an overview of the recent developments in visualizing the liquid water within a PEM fuel cell and this has focused on nuclear magnetic resonance (NMR) imaging, beam interrogation and direct optical photography. Each technique has their pros and cons and these are summarized in Table 2.1.

In this thesis, a direct visualization technique has been used to obtain an understanding of the water behaviour inside the PEM fuel cell due to the advantages and its ease to be utilized for the in-house transparent PEM fuel cell. Numerous previous works [60], [81]–[87] have been performed experimentally using this technique to visualize the water behaviour and distribution inside the PEM fuel cell.

Tuber et al. [81] performed a visualization of the water build up in the cathode of a transparent PEM fuel cell under different operating conditions and diffusion layer characteristics. However, the visualization was performed at the cathode only. Spernjak et al. [60] on the other hand visualised the water accumulation at both the anode and cathode channels under different operating conditions. They studied the effectiveness of different GDL materials in water removal in the flow channels of a transparent PEM fuel cell.

Ous et al. [82] investigated the accumulation of water in the flow channels of a transparent PEM fuel cell under different operating conditions by direct visualization. However, the visualizations at both the anode and cathode flow channels were not performed simultaneously and also there was no temperature distribution investigation. Weng et al. [83] also employed direct visualization in investigating the distribution of water and water flooding inside the cathode flow channels under different cathode stoichiometries.

Meanwhile, Kandlikar et al. [84] performed a simultaneous direct visualization at the anode and cathode flow channels to characterise and quantify the two-phase flow under different anode and cathode stoichiometry ratios. Using a digital video processing algorithm, the quantification of liquid water in the flow channels was obtained as the water coverage ratio. In another research utilising direct visualization and image processing by Bozorgnezhad et al. [85], two-phase flow and droplet behaviour in microchannels of a PEM fuel cell were investigated under different operating conditions. The emphasis was in analysing the two-phase pattern and these were characterised in different patterns, such as small droplets, medium droplets, film flow, annular, slug and plug.

Zhan et al. [86] also employed a direct visualization technique in investigating the water transport in a transparent PEM fuel cell under different operating conditions. However, the visualization was focused on the liquid water flow state at the turns of the serpentine flow channels. Also, the water production and emergence was analysed at the cathode flow channels only.

Another recent investigation was performed by Ramiar et al. [88] and also they utilised direct visualization in investigating the water management of a transparent PEM fuel cell. The effect of dead-end and open-end modes was studied with the proposed novel flow field channels.

Table 2.1: Summary of the visualization techniques and their advantages and disadvantages [38].

Technique	Pros	Cons
NMR	• Compatible with operating fuel cell • Can detect water under land areas	• Incompatible with carbon materials • Limited spatial and temporal resolutions
Neutron imaging	• Compatible with operating a fuel cell and carbon materials	• Limited spatial and temporal resolutions • Limited availability
Synchroton X-ray	• Compatible with operating a fuel cell and carbon materials	• Limited temporal resolutions • Limited availability
Direct visualization	• Compatible with operating a fuel cell • High temporal and spatial resolutions	• Require a transparent window
Fluorescence microscopy	• High temporal and spatial resolutions	• Has yet to be demonstrated with an operating fuel cell

2.5 THERMAL MANAGEMENT IN PEM FUEL CELL

Apart from the water management challenge, proper thermal management also has been recognized as being one of the critical technical issues that must be resolved before PEM fuel cells can be commercialized [89]. From the overall reaction (2.3), waste heat is produced from PEM fuel cells and this limits its energy efficiency to about 50% [90]. Apart from the electrochemical reactions, heat can be generated from the water behaviour in PEM fuel cells as well. The water and thermal management is directly linked because:

i. the absorption and release of latent heat results from the evaporation and condensation processes;
ii. water and heat transport occur in conjunction with each other due to a heat pipe effect. Meaning a temperature gradient induces a phase change and the net mass transfer of water [91], and
iii. the saturation pressure is strongly dependent on the local temperature [92].

For the fuel cells with no active cooling, the heat is generally transported through the cell components through conduction and eventually is removed via the reactant gases in the flow field channels. Hence, it is more relevant and useful to investigate the water and thermal management simultaneously.

Temperature has a significant influence in achieving a high performance of PEM fuel cells [93]. This is due to strong temperature effects on the activity of the catalyst, dehydration of polymer membrane, mass transfer and thermal management of PEM fuel cells. The temperature distribution over the MEA surface has a big impact on the performance, lifetime and reliability of PEM fuel cells. Membrane dehydration can occur if the local temperature on the MEA surface is too high, while water condensation and flooding may occur on the other hand. Generally, the temperature is not distributed over the MEA surface in a homogeneous form [94]. This inhomogeneous distribution may decrease the reliability and durability of the membrane applied in PEM fuel cells thus achieving a uniform temperature distribution with a small variation being favoured for PEM fuel cells. Any hot spots should be avoided in order to increase the reliability and durability under the operation of PEM fuel cells. Hence, determining the temperature distribution over the MEA surface inside the PEM fuel cell is essential in order to ensure proper thermal management and that the PEM fuel cell operates safely.

Temperature measurements inside the PEM fuel cell using thermocouples, micro-sensors and infrared thermal cameras have been commonly used by several researchers [90],[92]–[97]. Guo et al. [92] revealed that the temperature distributions over the MEA surface were higher at the downstream than the upstream region, and hence could easily locate the hot regions from infrared temperature images. Also, they reported that the non-uniformity of the temperature distributions increases with higher current density. In other research, Lin et al [95] utilized thermocouples inserted inside the PEM fuel cell to measure the temperature distributions. They reported that the non-uniformity of the temperature distribution was not negligible and it was larger at the cathode side compared to the anode side. Lee et al. [99] on the other hand fabricated flexible sensors which were embedded in the PEM fuel cell to measure the temperature distribution and revealed its feasibility to measure the local temperature.

Although numerous measurements of the temperature distribution have been reported, simultaneous investigations and the visualization of the water and temperature distribution and their relations in PEM fuel cells are very scarce. Hakenjos et al. [94] designed a special PEM fuel cell that allowed simultaneous investigation of the water and temperature distributions under different air flow rates. They reported that the enthalpy of the condensation is the cause for an elevated temperature in regions where liquid water is observed. Kim et al. [100] performed a similar investigation to that of Hakenjos et al. [94] and reached to the same conclusion, i.e. the enthalpy of condensation is the cause of the high temperatures in the regions where liquid water is observed. Both of the above research groups presented images of the temperature and water distributions at the cathode side from the infrared thermal camera and the digital camera, respectively. However, the status of liquid water at the anode side has not been visualized in the above investigations. The liquid water at the anode side of the PEM fuel cell may be a performance-limiting factor as it may cause flooding under certain conditions, e.g. when operating with a low current density, with a low fuel rate or when the humidifying water of the fuel condenses under certain operating conditions [101] and [102]. Also, both of the above studies have been limited to a qualitative description of liquid water and they have not provided a quantitative indicator on how flooded are the channels. In another investigation, Daino et al. [103] studied the water transport and thermal profile in a PEM fuel cell. They analysed the images of liquid water and temperature profile across both the anode and cathode GDL under different current densities. Nishida et al. [104] studied the water vapour, temperature and current distribution on the anode side in a low humidity PEM fuel cell. In addition, they discussed the effect of the flow configuration on the water transport and reaction distribution.

2.6 OPERATING CONDITIONS

As mentioned in Section 2.4, water in a PEM fuel cell has to be managed properly in order to avoid flooding or drying and thus lead to a better performance of a PEM fuel cell. In addition, the performance of the PEM fuel cell is also influenced by many parameters, such as operating temperature, pressure, humidification and flow rate of the gas reactants [105]. It is very important to understand the effects of these parameters on the performance of a PEM fuel cell.

As mentioned in the “First Fuel Cell law” [16], one cannot change only one parameter in a fuel cell as the changing of one parameter causes a change in at least two other parameters and at least one of them has an opposite effect to the one expected to be seen. There has been a huge number of researches performed experimentally and numerically to investigate the effects of these parameters on the performance of a PEM fuel cell and these are summarized in Table 2.2.

Table 2.2: Summary of the previous investigations and their parameter study.

Author	Parameter study	Methods
Ma et al. [106]	• Anode and cathode gas humidity	3D Mathematical Modelling
Wong et al. [107]	• Anode and cathode gas humidity	2D Modelling
Tohidi et al. [108]	• Anode and cathode gas flow rate • Cell temperature • Operating pressure • Anode and cathode gas humidity	1D Modelling
Zhang et al. [109]	• Anode and cathode gas humidity at elevated temperature	Experimental and mathematical analysis
Wang et al. [110]	• Anode and cathode gas humidity	3D Modelling
Guvelioglu et al. [111]	• Anode and cathode gas flow rate • Anode and cathode humidity	2D and 3D Modelling
Saleh et al. [112]	• Symmetrical and asymmetrical anode and cathode gas humidity at different temperatures	Experimental
Yan et al. [113]	• Anode and cathode gas humidity • Anode and cathode gas flow rate • Operating temperature • Operating pressure	Experimental
Amirinejad et al. [114]	• Operating temperature • Operating pressure • Anode and cathode gas humidity	Experimental

Wang et al. [115]	• Operating temperature • Anode and cathode gas humidity • Operating pressure • Anode and cathode gas flow rate	Experimental and 3D modelling
Williams et al. [116]	• Anode and cathode gas humidity • Operation temperature • Cathode gas flow rate	Experimental
Wang et al. [105]	• Operating temperature • Anode gas humidity • Operating pressure	Experimental and 3D modelling
Lee et al. [117]	• Anode and cathode gas humidity • Operation temperature	Experimental
Misran et al. [118]	• Operating temperatures • Operating pressure	Experimental and modelling
Sinha et al. [119]	• Operating temperature	3D modelling
Rohendi et al. [120]	• Operating temperature • Operating pressure	Experimental
Bilgili et al. [121]	• Anode and cathode flow rates • Anode and cathode gas humidity • Operating temperature • Operating pressure	3D Modelling

Since the main methodology of this thesis is focused on using an experimental investigation, previous experimental investigations performed by other researchers have been theoretically investigated. Zhang et al. [109] have studied the effect of the relative humidity on the PEM fuel cell performance at elevated temperatures of 120 °C. They found that the fuel cell performance could be depressed significantly by decreasing the relative humidity from 100% to about 25%. However, a special MEA that can withstand an elevated temperature needs to be fabricated. However, they only investigated the water behaviour inside the PEM fuel cell.

Saleh et al. [112] also investigated the effect of the relative humidity on the PEM fuel cell performance. However, they performed a different experimental setup. The cathode and anode relative humidity were set at equal and unequal values so as to have a symmetrical and asymmetrical relative humidity. Also, in this investigation, they did not investigate the water behaviour inside the PEM fuel cell.

Another experimental investigation was performed by Yan et al. [113] by manipulating the operating conditions of the PEM fuel cell. Both single fuel cell and stack configurations were used in the investigations. Again, they did not perform a water behaviour investigation.

Similarly, Amirinejad et al. [114] performed an experimental investigation but the water management investigation was not performed when investigating the effects of the operating conditions on the cell performance. In addition, they used a very small single PEM fuel cell with an active area of 5 cm^2. Another experimental investigation using a very small single PEM fuel cell was performed by Williams et al. [116] and their total active area was only 6.25 cm^2.

Wang et al. [115] performed another experimental investigation on the operating conditions of the PEM fuel cell. However, they used a different flow field channel type, namely the interdigitated flow fields and these are not the best flow field channel types as reported by Spernjak et al. [122].

Hence, in this thesis, some of the important operating parameters, namely gas flow rate, gas relative humidity and operating pressure are the focus of this work and the effects of these parameters on the fuel cell performance will be investigated, as well as visualizing the water behaviour inside the PEM fuel cell and the temperature distributions over the MEA surface.

The humidification of the reactant gases ensures the hydration of the membrane, especially at lower current densities. However, if the humidification continues at a higher current density, it will result in water flooding. As for the flow rate, a high gas flow rate will assist in the removing of the excess water in the flow field channel. However, at lower current density operations and dry gas condition, the high gas flow rate will make the membrane dry. Meanwhile, a fuel cell generates more power when the operating pressure is increased. However, the pressurization also related to the water management problem. Thus, in this study the effect of these parameters will be studied at both sides of the electrode under several sets of operating conditions.

2.7 GAS PERMEABILITY OF THE GAS DIFFUSION LAYER

One of the vital functions of the GDL is that it acts as a medium through which gases permeate in order to get to-and-from the catalyst layer. Hence, the GDL must be sufficiently permeable and porous to allow the flow of both reactant gases and waste products of water and heat. The permeability of the GDL somewhat dictates the rate of mass transport through the cell, and in the case of a small fuel cell, heat removal from it. Therefore, the key indicator of material performance is the permeability of a fuel cell [123]. Generally, carbon paper or carbon cloth that is a porous and fibrous material makes the GDL structure. Figure 2.4 shows how they compare to each other.

There are several reasons why carbon-based materials are commonly used as GDLs. These are due to their stability in acidic environments, capability to provide high gas permeability, high electrical conductivity and their elasticity under compression [37]. In term of performance, carbon cloth is a better choice as a GDL material at high-humidity operations while carbon paper performed better under dry conditions [124]. However, more interest is shown in carbon paper, as it tends to be more affordable and compatible with a MPL.

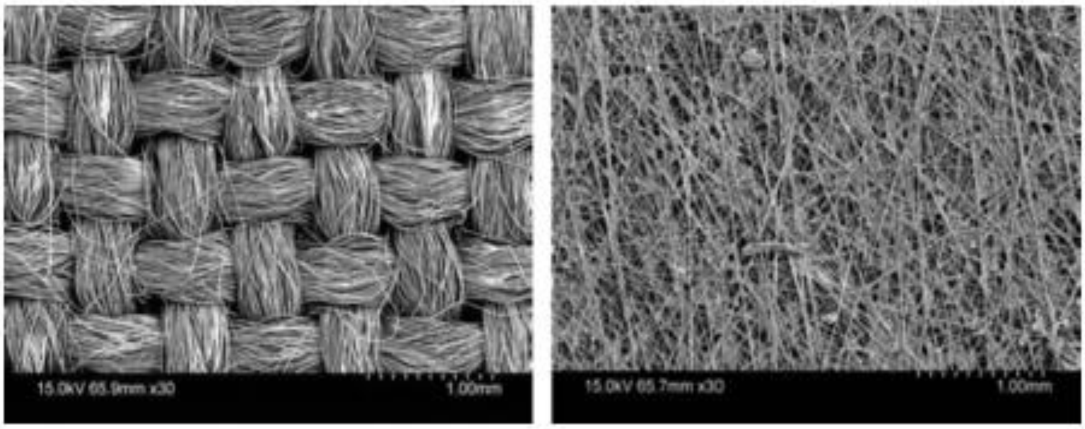

Figure 2.4: Comparison between carbon cloth and carbon paper structure [123].

There has been extensive research [42], [125]–[136] carried out on the permeability of GDL with different emphasis such as how compression, GDL thickness, PTFE loading, carbon loading and MPL components affect the porosity of the material. Gurau et al. [126] described a method to determine the absolute in and through-plane permeability of the GDL by controlling the gas flow through the porous sample. They reported that the permeability coefficients increase with the samples that have higher content of PTFE. However, it is reported by Pharoah [127] that the in-plane permeability plays a bigger role than the through-plane permeability in fuel cell mass transport. Gostick et al. [128] also reported that the in-plane permeability was significantly more than the through-plane permeability for the different GDL samples. Ismail et al. [133] in their 2011 publication studied the effect MPL had on the water vapour transport coefficients. It was reported that the water transport and the permeability of MPL improved by increasing the PTFE loading within the MPL. The through-plane permeability is significantly lower than the in-plane permeability which agreed as reported by the previous researchers [127], [128]. Ihonen et al. [136] studied the effect of compression on the GDL characterisation and they reported that the compression increases cell flooding due to the decreased porosity of the GDL. Tamayol et al. [135] also investigated the effect of mechanical compression on the through-plane gas permeability and reported similar results.

However, to my best knowledge, there has been no previous research conducted into how heat treatment affects the through-plane gas permeability of the GDL samples. This information is vital in order to have further insight on recent developments of high temperature PEM fuel cells to solve the water management problem. PEM fuel cells normally operate at low operating conditions; however, it could be beneficial to discover how the GDL behave to heat treatment to investigate how their performance differs with temperature. It can be assumed that exposing the GDL to heat would cause it to melt to some extent and alter its morphology and porosity, which subsequently affect the permeability.

2.8 CHAPTER SUMMARY

In this chapter, a literature review, namely an overview of the PEM fuel cell, the components of the PEM fuel cell and the water and thermal management inside the PEM fuel cell has been presented. Also, this chapter presents the gas permeability of GDL which affect the reactant gases transport within the porous media.

The water and thermal management investigations performed by previous researchers have been critically reviewed in this chapter to discover the knowledge gaps, which subsequently shape the direction of this thesis. In addition, this chapter reveals some gaps in the knowledge and some opportunities for the improvement of the PEM fuel cells that may be investigated.

CHAPTER 3

EXPERIMENTAL SETUP

In this chapter, the research methodology that has been employed for the investigation on the PEM fuel cell is described. Section 3.1 provides the research objectives and the flow process of the investigation. This is followed by the main part of the chapter and a description of the in-house fuel cell test station (FCTS) which described in Section 3.2. All the operating conditions, controller and measurement systems are explained briefly as part of the components of the FCTS. In Section 3.3, the visualization technique applied in the temperature distribution investigation is described. Finally, Section 3.4 provides the experimental setup for the improvement in the PEM fuel cell.

3.1 RESEARCH OBJECTIVES

An experimental approach is employed in this thesis and it is explored in this chapter. The approach will be performed with three main objectives, as mentioned in Section 1.4, which are as follows:

i. to investigate the water management in a PEM fuel cell under different operating conditions
ii. to investigate the temperature distributions in a PEM fuel cell under different operating conditions
iii. to investigate the through-plane gas permeability of GDL under heat treatment

The general idea of the experimental approach is shown in Figure 3.1. The experimental setup to achieve the research objectives can be summarized in three parts, namely:

1. Water management investigation
2. Thermal management investigation
3. Gas permeability investigation

In order to meet the objectives of this investigation of the water and thermal management in a PEM fuel cell under several sets of operating conditions, the PEM fuel cell must be operated at an acceptable fuel cell performance. Therefore, a commercial PEM fuel cell is used in order to obtain a good performance for the PEM fuel cell.

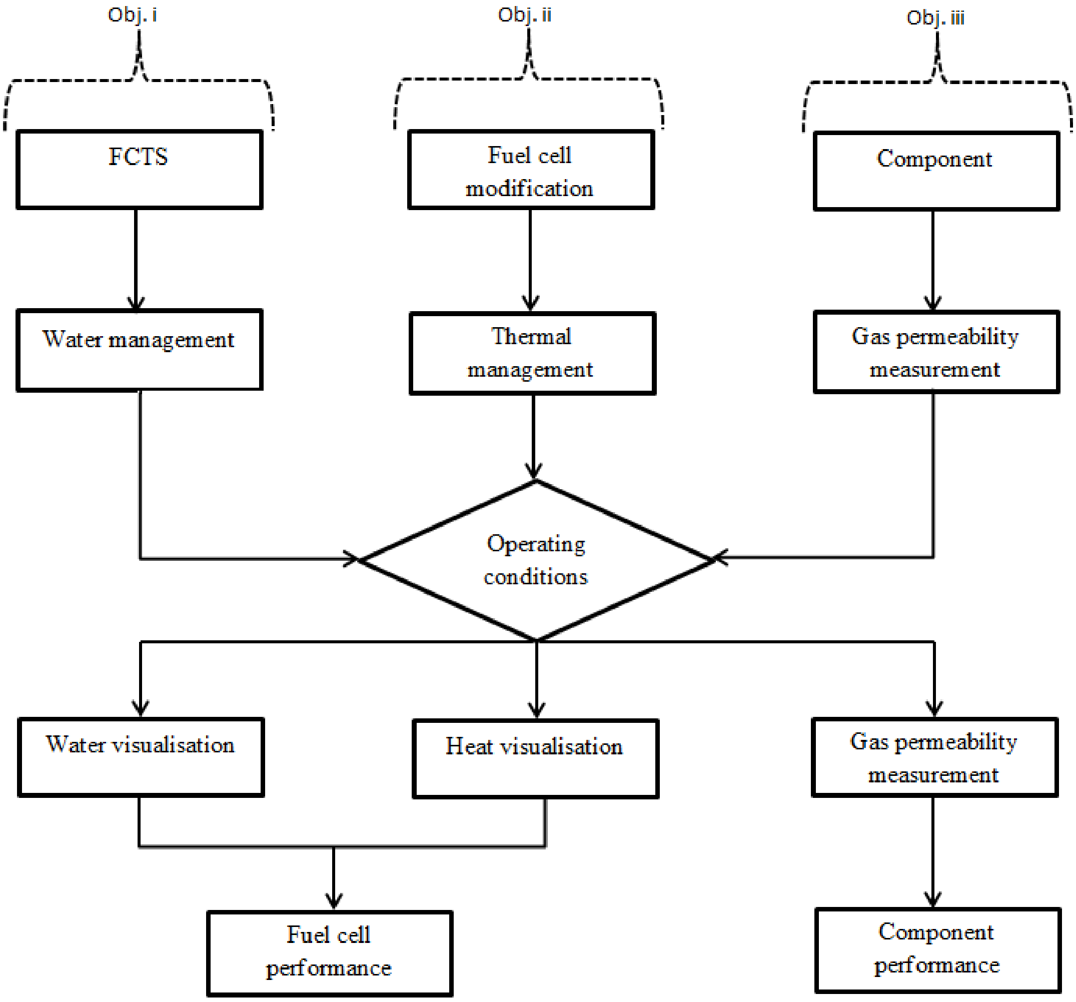

Figure 3.1: General schematic of the experimental approach.

3.2 FUEL CELL TEST STATION (FCTS)

The water management investigation inside the transparent PEM fuel cell requires a fuel cell rig that can provide complete control and monitoring systems during the experimental investigation on the PEM fuel cell. An in-house FCTS, which has been designed by a previous researcher [137], is utilised to perform the experimental investigations on the operating conditions of the PEM fuel cell and the cell performance.

The test station is equipped with both a controlling and monitoring system for the reactant gas flow rate, reactant gas pressure, reactant gas inlet relative humidity, temperature of the PEM fuel cell, temperature of the reactant gas inlet and the electronic load to the PEM fuel cell. In addition, the test station monitors the temperature of the reactant gas outlet and the pressure drop across the PEM fuel cell. Further, a data acquisition system is applied to log all the experimental data and at the same time to enable it to be monitored and controlled.

There are two symmetrical sections on the FCTS which correspond to the anode and cathode electrodes of the PEM fuel cell. Both sides go through the same flow process of the operating fuel cell. A schematic of the design process of the FCTS is shown in Figure 3.2. The reactant gases, hydrogen and air, are provided through the gas supply system from the main gas source. The maximum pressure of the reactant gas is controlled by the gas supply system, the flow control systems control the flow, and the amount of the reactant gas supplied into the FCTS. To serve as the main gas source, the gas generator, or the gas cylinder, can be fitted into the FCTS.

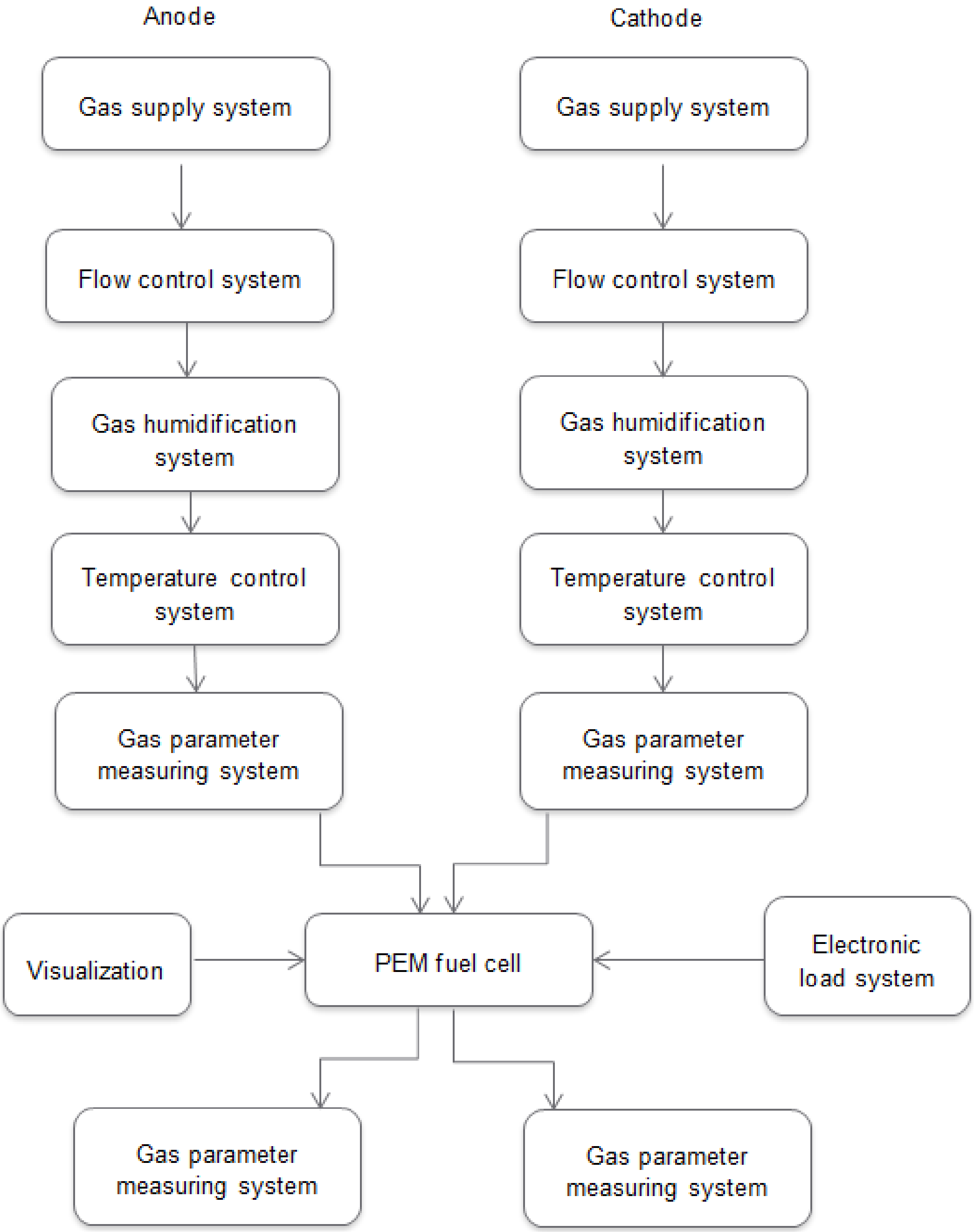

Figure 3.2: A schematic of the design process of the FCTS.

The reactant gas then flows to the gas humidification system where it is humidified to a certain level of the gas relative humidity required in the experimental investigations. After humidification, the temperature of the reactant gas is controlled and monitored by the temperature control system. Further, the reactant gas is heated along the gas tubes after the gas humidification system to the gas inlet connection in the PEM fuel cell. In addition, the temperature of the humidifier in the gas humidification system is also controlled and monitored by the temperature control system.

To complete the control and monitor the reactant gas, the FCTS is fitted with a gas parameter measuring system. This consists of electronic devices that provide readings of the temperature and pressure in the gas inlet of the PEM fuel cell. Not only that, the reading of the pressure drop between the gas inlet and outlet of the PEM fuel cell and the temperature of the gas outlet is provided by the system. Two commercial potentiostats are connected directly to the PEM fuel cell in the FCTS to control and measure the operating voltage and current. All the measured data from the electronic measurement devices in the FCTS are converted to reading signals, which consist of the following:

i. Gas inlet and outlet flow rates
ii. PEM fuel cell temperature
iii. Gas inlet and outlet temperatures
iv. Gas inlet relative humidities
v. Gas inlet pressures
vi. Pressure drop across the PEM fuel cell

A data acquisition system is used to log and record all of the sent reading signals into the computer.

The in-house FCTS is designed for a single cell or multiple cells of small power category of the PEM fuel cells, as it has a maximum testing power only up to 80 W. This is based on the typical performance of the PEM fuel cell and the configuration of the in-house FCTS. However, it could be modified to have a higher maximum testing power by using, for example, an upgrading of the mass flow meters.

Further, 2.5 bar of working pressure has been set for this FCTS due to the limitation in the working pressure for the installed humidifier in the FCTS. To ensure a safe operating condition, safety valves are installed on both the anode and the cathode sides of the FCTS. These valves release the gas in order to stabilise the pressure whenever the working pressure inside the FCTS exceeds the set limitation.

Figure 3.3 shows a photograph of the in-house FCTS. There are two main sections in the structure of the FCTS. All the electronic measuring and monitoring devices, such as the computer and flow controller power unit, are located on the right hand side of the FCTS while the PEM fuel cell and the process equipment are located at the left hand side. In order to enhance the controlling and monitoring of the operating parameters, a touch screen monitor is installed into the FCTS and the operator of the FCTS can easily monitor parameters to be read through the LabVIEW interface on the touch screen monitor. Also, another portable monitor is available to be employed by the operator so that it provides a convenient and user-friendly FCTS.

A detailed overview of the FCTS components is discussed in the following subsections which include: the flow control system, the gas humidification system, the temperature control and measurement system, the electronic control system, the data acquisition system and the visualization system.

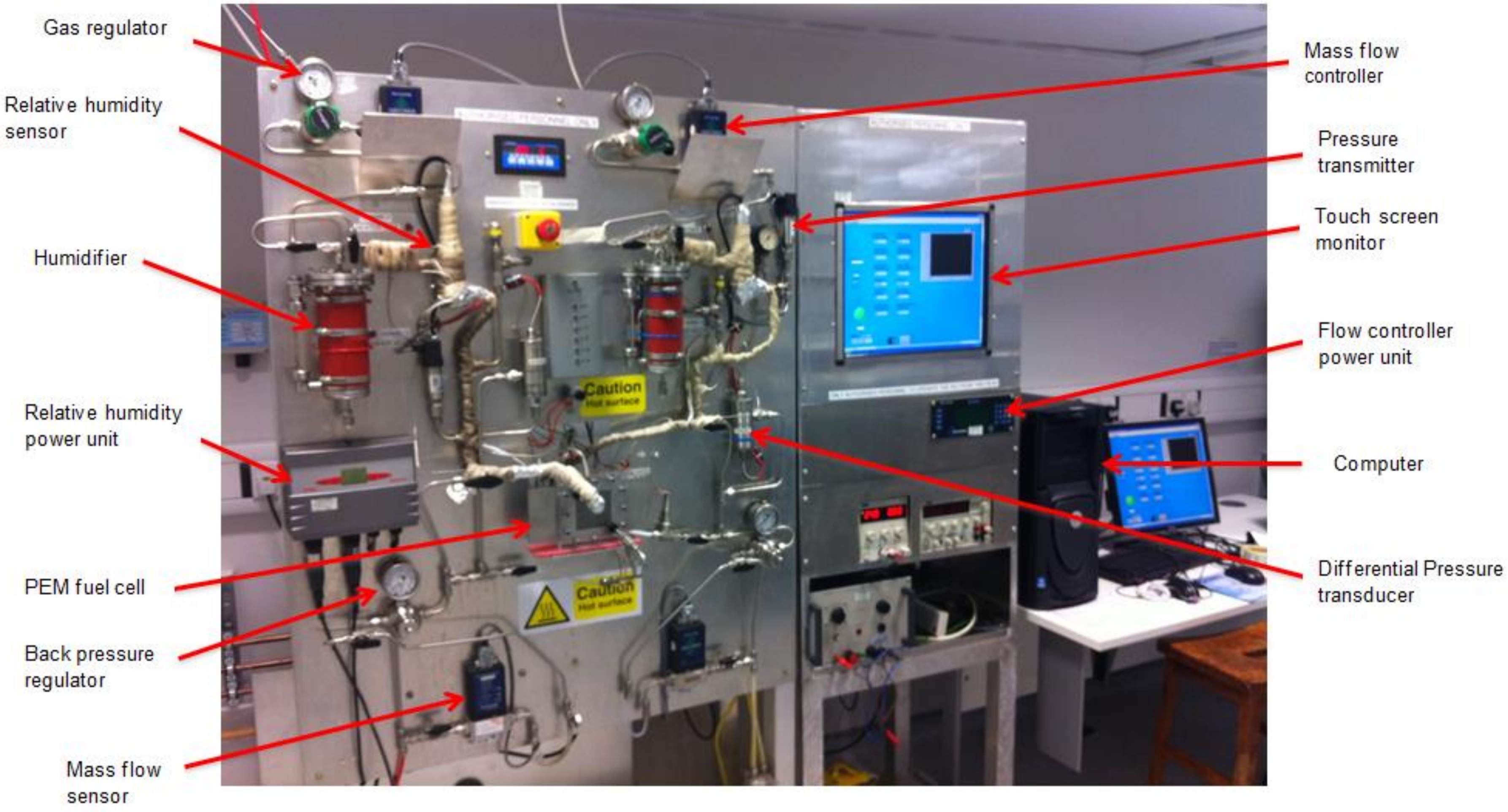

Figure 3.3: A photograph of the in-house fuel cell test station.

3.2.1 Flow control system

In this FCTS, compressed gas bottles of hydrogen, air and nitrogen are used as the reactant gases supplier for the PEM fuel cell experimental investigations. High purity hydrogen and purified air are used as the fuel and oxidant in order to prevent the fuel cell from being poisoned on the catalyst. Hence, this could increase the life time of the PEM fuel cell. The FCTS also accepts other gas sources as reactant gases, such as hydrogen gas from a water electrolyser. Further, the hydrogen as outlet of the water electrolyser can be easily connected to the FCTS gas inlet tubes. The fuel and oxidant reactant remaining in the FCTS gas lines and the PEM fuel cell after operation of the FCTS could give a potential hazard since the hydrogen gas is very flammable. That is why nitrogen is used for purging purposes to clean the remaining fuel and the oxidant reactant before operating the FCTS. For this purpose, a two-way valve is installed in the FCTS to switch the supplied gas from the nitrogen to the reactant gases or vice versa by the operator.

The gas regulators at the inlet control the working pressures in the FCTS. The high pressure of the gases from the gas sources are regulated by these regulators to a suitable working pressure of the FCTS and an acceptable operating pressure of the PEM fuel cell. The maximum working pressure of this FCTS, namely 2.5 bar, is due to the gas humidifiers maximum pressure installed into the FCTS. Hence, to operate the FCTS at a high working gas pressure, the gas humidifiers in the FCTS have to be bypassed. The design of the operating PEM fuel cell also must be designed to the desired operating pressure. There are two backpressure regulators installed in the FCTS at the gas outlets of the PEM fuel cell to control the operating pressure inside the PEM fuel cell.

Two pressure transmitters, model Omega PX4202 with 0.25% full scale accuracy are used to measure the gas inlet pressures of the PEM fuel cell in the FCTS. Both of them are installed before the anode and the cathode gas inlet of the PEM fuel cell. Apart from that, there are two differential pressure transducers installed in the FCTS between the gas inlet and the gas outlet of the PEM fuel cell. Both of these transducers model Omega PX81 with 0.25% full-scale accuracy measuring the pressure drop between the anode and the cathode of the PEM fuel cell. The signal readings from both of these two pressure devices, pressure transmitters and differential pressure transducers are sent to the data acquisition system for recording and monitoring.

The flow rates of the supplied gas into the PEM fuel cell are controlled by the mass flow controllers that are installed in the FCTS before the gas inlets of the PEM fuel cell. In addition, the gas flow rates that flow out from the PEM fuel cell are also being measured. This is achieved by the mass flow sensors, which are installed in the FCTS after the gas outlets of the PEM fuel cell. The mass flow control system model Teledyne Hasting Instrument, HFC-202 is used for both the anode and the cathode side. However, the range of the flow rate in standard litre per minute (SLPM) is set namely 0 to 1 SLPM for the anode and 0 to 5 SLPM for the cathode. These ranges of gas flow rates are chosen based on the size and performance of the PEM fuel cells which have been used in previous experimental investigation [138]. The active area of the transparent PEM fuel cell used in that investigation is 50 cm^2. Then, a commercial single PEM fuel cell that has the same active area from ElectoChem Inc. (USA) has been used to estimate how much gas flow rate is required for such a size of PEM fuel cell. This commercial PEM fuel cell typically gives 700 mA/cm^2 at 0.60V and requires 0.25 H_2 SLPM at a 1.2 anode gas stoichiometry and 1.37 air

SLPM at a 2.5 cathode gas stoichiometry ratio. Thus, due to this reference commercial PEM fuel cell, a range of gas flow rates has been set between 0 to 1 and 0 to 5 SLPM for the anode and the cathode sides, respectively.

3.2.2 Gas humidification system

In order to humidify the reactant gases, the bubble gas humidifier vessels are installed into the FCTS for both the anode and the cathode side. The reactant gases must flow through the humidifier to be humidified to a certain humidity level. In addition, using an installed two-way valve, the reactant gases could bypass the humidifier to obtain a zero humidity of the reactant gases. The reactant gases are humidified by the vessels through water bubbling. In order to obtain a certain level of humidity, the temperature of the humidifier vessels is set up. This can be obtained using attached electrical heater mats on the vessels and the water temperature inside the vessels is raised to the set temperature. The reactant gas flows through the vessels gas inlet into the bubble dispenser, which is under the water level, and then the dispensed gas flows through the water and flows out with the vaporised water through the vessels gas outlets. The quantity of vaporised water, which humidifies the reactant gas, is controlled at this water temperature and at the water level inside the vessel. It is easier for the water to be vaporised when the temperature of the water is high.

There must be a sufficient amount of water inside the vessel and the operator monitoring the water level from a visor tube on the side of the vessel can ensure this. All the dispensed gases will be in contact with the water and have an adequate retention time if the water level inside the vessel is kept higher than the level of the bubble dispenser. The longer the retention time of the gas, the higher the gas may be humidified and this can be obtained if the water level inside the vessel is high. However, the water level must not be too high to prevent it from spilling out from the vessel through the gas outlet into the gas tube. Apart from that, the use of de-ionised water inside the vessel to humidify the gases is required to minimise the contamination to the gases and the fuel cell.

A photograph of the bubble gas humidifier vessel is shown in Figure 3.4 and a schematic diagram is shown in Figure 3.5. The water level inside the vessel can be monitored accordingly through the water level attached to the vessel, as shown in the photograph in Figure 3.4. In order to heat the vessel and the water inside it, a silicone heater is wrapped on the vessel outer wall. There are two relative humidity sensors installed in the FCTS to measure the anode and the cathode gas inlet relative humidities of the PEM fuel cell. Both of them, model Hygroflex Rotronic, send the reading signals to the relative humidity power unit before sending the signals to be processed by the data acquisition system. Finally, the relative humidity readings are shown on the computer screen through the LabVIEW software program. In addition, the sensors also can provide the gas temperature readings at the location of the sensors and these readings can be manipulated to obtain the exact relative humidity readings at the gas inlet of the PEM fuel cell, where the temperatures are controlled and measured by the temperature controllers and the thermocouples.

Figure 3.4: A photograph of the bubble gas humidifier installed in the FCTS.

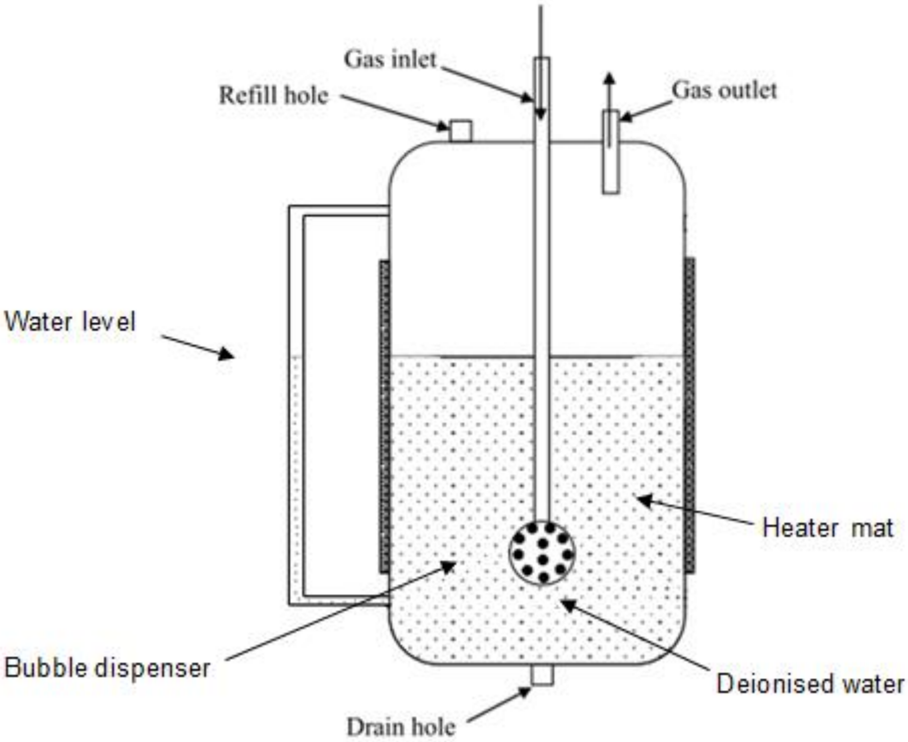

Figure 3.5: A schematic diagram of the bubble gas humidifier installed in the FCTS [138]

3.2.3 Temperature control and measurement system

A multi-zone temperature controller controls all the temperature parameters, namely, the temperature of the PEM fuel cell, the temperature of the gas humidifiers and the temperature of the reactant gases, model Omega CN1500 Series. There are up to seven channels offered by the temperature controller to control and measure the temperature inside the PEM fuel cell, the temperatures of the anode and the cathode gas inlets and outlets and the temperatures of the anode and the cathode bubble humidifiers. The temperature of the humidifier vessels are measured by the two thermocouples that have been set up in the gas humidifiers. Then, the temperatures of the reactant gases are measured by four thermocouples, model Omega TC-J-BSPT, two thermocouples at the anode and the cathode gas inlets and two thermocouples at the anode and the cathode gas outlets of the PEM fuel cell. All the thermocouples send the reading signals to the main temperature controller in the FCTS and to the data acquisition system where the signals are processed.

The in-house FCTS has been designed to enable a very accurate measurement of the gas inlets and outlets of the PEM fuel cell. Thus, all the thermocouples that have been setup in the FCTS are located as close as possible to the PEM fuel cell. This is one of the improvements compared to the commercial FCTSs, which have their thermocouples inside the body of the FCTS to measure the gas inlet temperature of the PEM fuel cell. Using this arrangement of thermocouples, an inaccurate reading of the gas temperature may be obtained due to the rapidly changing gas temperature along the gas tube that connects the thermocouple to the gas inlet of the PEM fuel cell. Thus, this improvement in the design of the in-house FCTS enables accurate measurements that are essential for the experimental investigations.

There is a heating element, which is an electrical heating cord, model Omega-HTC, wrapped around the gas tubes between the humidifier and the PEM fuel cell. The heating cord starts from the humidifier's gas outlet to the gas inlet of the PEM fuel cell to provide heat to the gas tubes and to the flowing gases as well. The heated tubes maintain the temperature of the gases and provide adequate heat to avoid the vaporised water from condensing. The set temperature of the gas inlet in the temperature controller controls the heat along the gas tubes. It is vital to avoid the condensation of the liquid water inside the gas tubes, particularly at the locations of the relative humidity sensors. If not, it is difficult to obtain accurate measurements for the relative humidity readings at the gas inlet of the PEM fuel cell. The liquid water that results from the condensation of the water vapour due to the temperature falling is difficult to quantify and this is why it is very important to heat the gas tubes. The range of the readings of the relative humidity sensors is from 0%RH (percentage of relative humidity) to 100% RH. Hence, even the presence of a small or high amount of liquid water at the location of the sensors, still gives a 100%RH reading. Thus, to avoid such a thing from occurring, the temperature of the gas in the tubes is always kept higher than the temperature of the gas humidifier. In this investigation, the temperature of the cathode gas inlet of the transparent PEM fuel cell is typically set at 75 °C so that the maximum temperature of 70°C can be set to the cathode gas humidifiers.

3.2.4 Electric control system

In order to control and measure the operating voltage and current of the PEM fuel cell, high-performance USB potentiostats from GAMRY, model Reference 3000^{TM} and Reference 30k Booster, are connected directly to the PEM fuel cell in the FCTS. The Reference 3000^{TM} potentiostat provides a maximum current of ±3 amps and a maximum voltage of ±32 volts. Meanwhile, the Reference 30k Booster^{TM}, which is an external hardware option, could increase the current limit of the Reference 3000^{TM} by a factor of 10 to ±30 amps. Further, the Reference 3000^{TM} with the Reference 30k Booster is an ideal system for the evaluation of energy technologies such as batteries and fuel cells. Moreover, the compliance limits of the Reference 30k enable a complete discharge and can accurately measure impedance values below 100 μΩ. These potentiostats are developed specifically to be used in applications for energy storage and conversion devices. A photograph of these potentiostats is shown in Figure 3.6.

These high-performance potentiostats are used to replace the previous electronic load system, model TTi LD300 DC Electronic Load used previously [137]. The operator had to change the setup manually using the previous electronic load system in order to investigate the constant-voltage or constant-current discharge mode while it can be set automatically using the high-performance potentiostats. This gives more flexibility to the operator while running the fuel cell for long time operating experiments.

Moreover, the previous electronic load system could not be used to measure the impedance value of the PEM fuel cell. All the reading signals by the potentiostats could be analysed using the GAMRY software installed in the computer.

Figure 3.6: A photograph of the Reference 3000TM and the Reference 30k Booster potentiostats.

3.2.5 Data acquisition system

A data acquisition system is used to record all the important parameters of the PEM fuel cell, such as the relative humidity, pressure, differential pressure and temperature. It consists of the National Instrument device, model NI-DAQ-9176 and commercial software, LabVIEW. The received voltage signals from the National Instrument device are converted to the correct units and scales of the parameters by the use of the LabVIEW software. All the various signals in the FCTS are received by two types of modules in the National Instrument package, namely NI 9205 and NI 9219. The gas inlet relative humidity, gas inlet pressure, PEM fuel cell differential pressure and gas inlet mass flow rates are received by the NI 9205 while the gas inlet and outlet temperatures are received by the NI 9219. Then, all the signals are shown on the computer screens in real time by an interface program.

In order to present the data on the computer screens, a program interface which was developed by using the LabVIEW software is used. This interface allows the operator of the FCTS to easily monitor and control the parameters through the computer screen. The main parameters, including the gas inlet pressures, gas inlet relative humidities, gas inlet temperatures and PEM fuel cell temperatures, are shown on the screen. All of these main parameters need to be monitored frequently to ensure that there are no occurring major changes. A photograph of the program interface is shown in Figure 3.7.

3.2.6 Water visualization system

As mentioned in Section 2.4.2, a direct visualization technique has been used to obtain the visuals of the water inside the flow channels of the transparent PEM fuel cell in the FCTS that enables the transparent PEM fuel cell to be visualized by a camera at both sides of the anode and cathode. There are two windows at the centre of the FCTS where the transparent PEM fuel cell is located and this enables the camera to directly visualize both of the sides simultaneously.

In the experimental investigation, a high quality digital camera, model Casio EX-F1, is used to record real-time videos inside the anode flow field gas channel of the transparent PEM fuel cell while another high quality digital camera, model Canon EOS 80D, is used to record real-time videos inside the cathode flow field channel of the transparent PEM fuel cell. The videos are analysed in order to obtain snapshot photographs at specific times. Using these cameras, it provides options of the captured images of the whole anode and cathode flow field gas channel to be taken at high speed shots or as a full resolution high definition (HD) video. In this experimental investigation, the camera was set at standard quality video that produces a quality of 640 x 480 pixels at 30 frames per second video. This is due to the limitations of the memory card to save a large video file because of the long operating time of the experimental investigations.

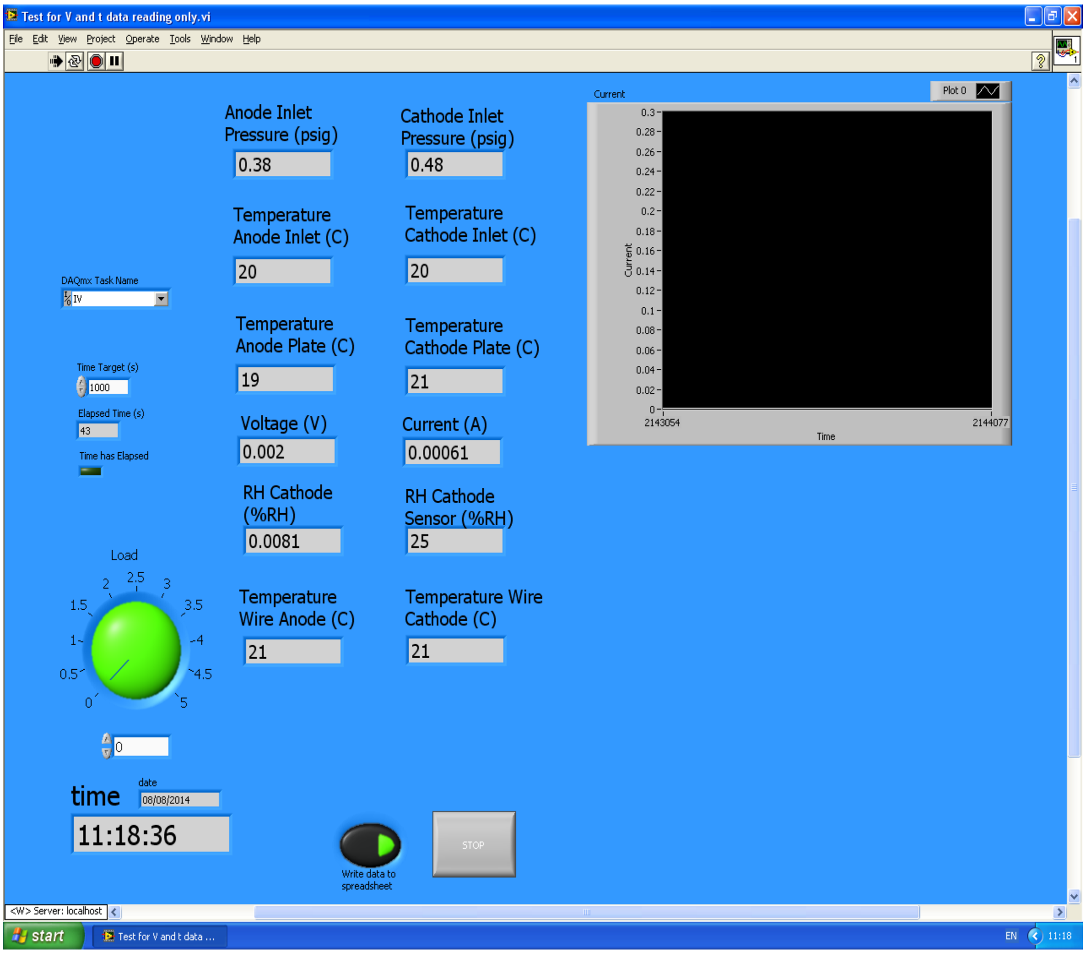

Anode Inlet Pressure (psig) 0.38
Cathode Inlet Pressure (psig) 0.48
Temperature Anode Inlet (C) 20
Temperature Cathode Inlet (C) 20
DAQmx Task Name IV
Temperature Anode Plate (C) 19
Temperature Cathode Plate (C) 21
Time Target (s) 1000
Elapsed Time (s) 43
Voltage (V) 0.002
Current (A) 0.00061
RH Cathode (%RH) 0.0081
RH Cathode Sensor (%RH) 25
Temperature Wire Anode (C) 21
Temperature Wire Cathode (C) 21
0
time 11:18:36
date 08/08/2014

Figure 3.7: A photograph of the program interface developed using the LabVIEW software.

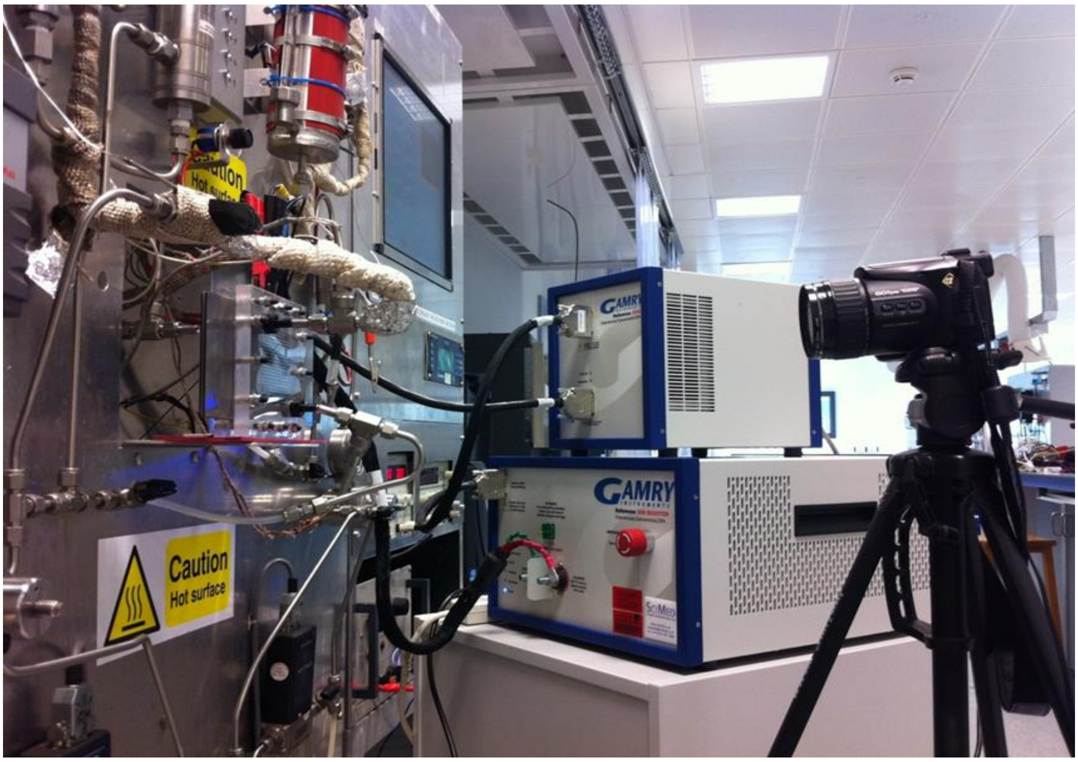

Figure 3.8: A photograph of the high quality digital camera, model Casio EX-F1 used for the visualization technique.

3.3 THERMAL IMAGING AND PEM FUEL CELL MODIFICATION

The distribution of temperature at the cathode side has been recorded using a thermal camera (FLIR T650sc), see Fig. 3.9. The camera used is sensitive to a range of infrared wavelength between 8 and 12 µm. To allow for more accurate thermal imaging of the cathode side of the fuel cell, where most of the heat is generated, the thickness of the two outermost transparent plates has been reduced from 20 to 4 mm using a milling machine; see Fig. 3.10. The material of the transparent plate is polymethyl methacrylate (PMMA) which has a relatively low thermal conductivity, k namely 0.19 $Wm^{-1}K^{-1}$ [139]. Therefore, the above thinning of the transparent plates has been necessary in order to minimize the thermal resistance and allow for the surface of the plate to be as reflective and as close as possible to the magnitude and distribution of the temperature of the MEA.

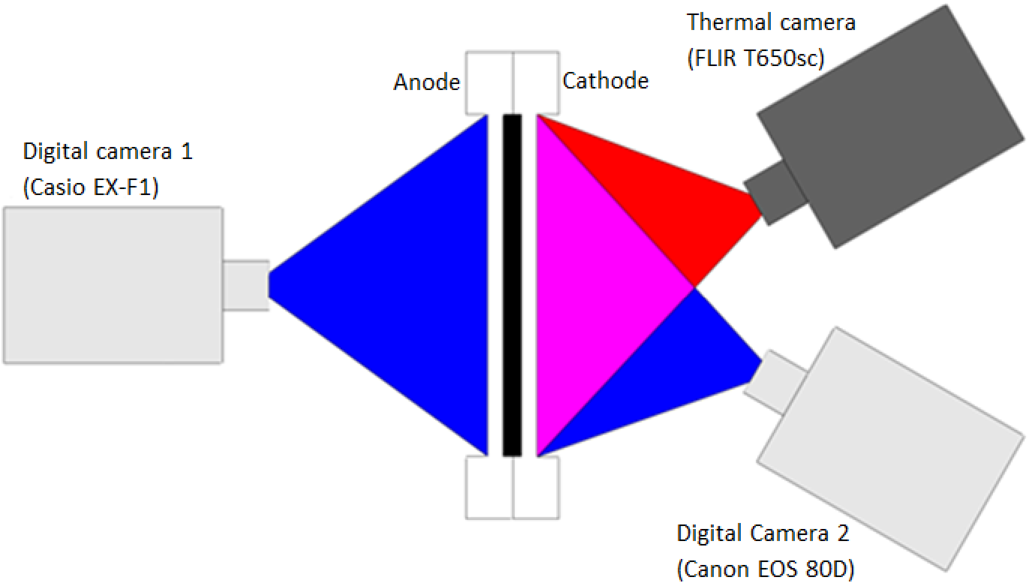

Figure 3.9: Schematic diagram of the temperature distribution experimental setup (top view).

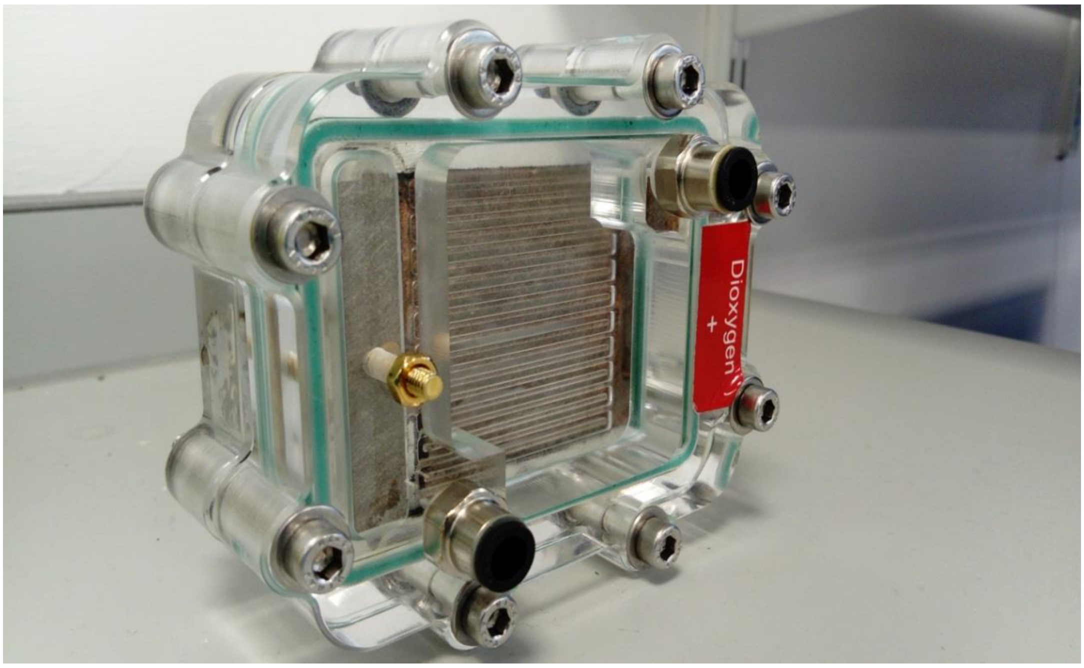

Figure 3.10: PEM fuel cell with reduced in thickness transparent plates.

3.4 GAS PERMEABILITY SETUP

The experimental setup and procedures for the measurement of the through-plane gas permeability are described in this section. Figure 3.11 shows the in-house experimental setup used to measure the through-plane gas permeability of the tested GDL samples.

Figure 3.11: A photograph of the in-house gas permeability setup.

Consisting of upstream and downstream fixtures, this setup requires the GDL sample to be positioned between the upper and lower fixtures, see Figure 3.12. Nitrogen gas flows at a fixed rate (set by the flow controller) through the GDL sample and the resulting pressure drop is measured by a pressure sensor (Omega, UK). It should be noted that the GDL samples were circular and of 25 mm diameter.

However, after placing the sample between the two fixtures of the setup, the area exposed to flow of nitrogen is only 20 mm.

As a result of the clamping of the sample between the two fixtures, some compression is imparted on the outer circumference of the GDL sample and the through-plane permeability of the sample may be affected. However, the sensitivity of the through-plane permeability to the tightness of fixing, whether the fixtures are loosely or tightly fixed, is insignificant as investigated previously by Ismail et al. [130].

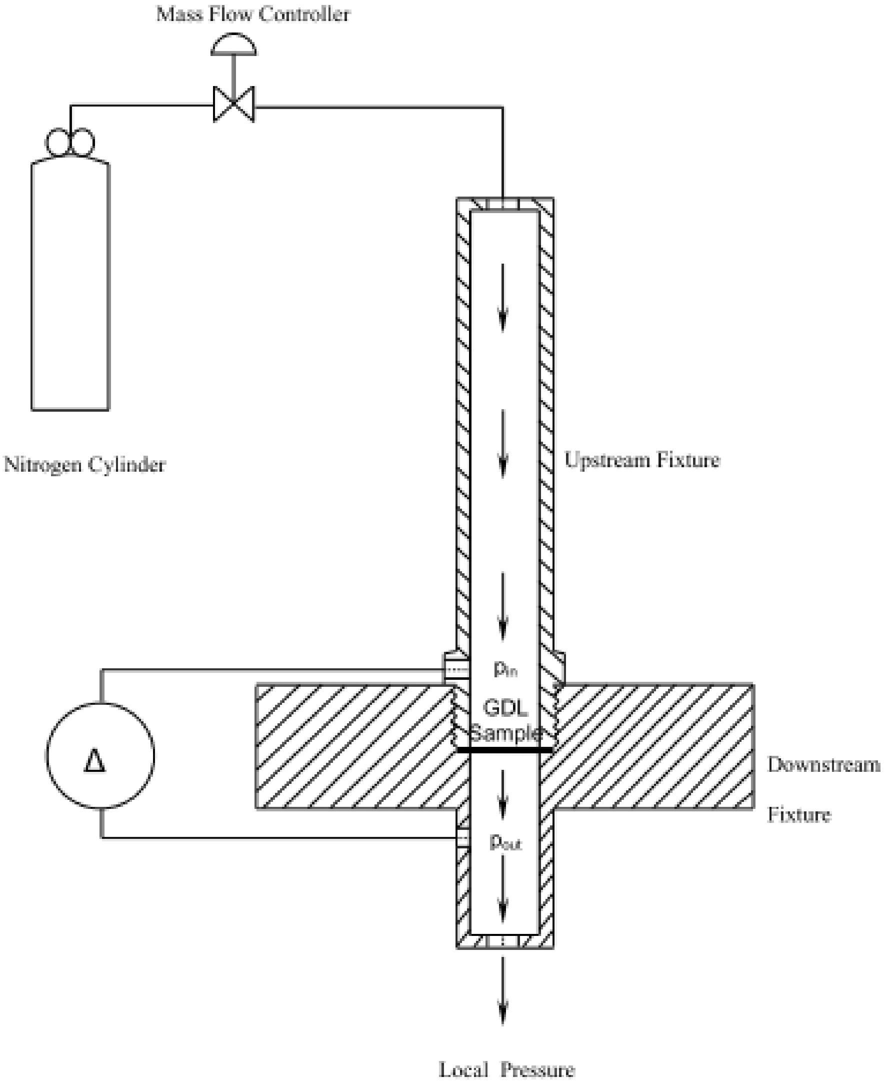

Figure 3.12: Schematic diagram of the experimental setup [133].

Eight flow rates were performed for each GDL sample, and the pressure drop across the sample was then measured for each flow rate. An MPL-coated GDL sample, such as SGL 10BC must be normally tested at a lower range of flow rate as the relatively low porosity of the MPL causes the pressure sensor to reach its limit (i.e. 12.5 Pa) with substantially lower flow rates compared to the carbon substrates (e.g. 10 CA). In this experimental setup, the flow controller, (HFC-202, Teledyne Hastings, UK) with a range of 0.0-0.5 SLPM and the differential pressure sensor, PX653 (Omega, UK) with a range of ±12.5 Pa were employed.

The experimental work focuses on the through-plane gas permeability of the GDL samples before and after heat treatment at relatively high temperatures are namely 200 °C, 500 °C and 800 °C.

3.4.1 Data Analysis

The main cause for the pressure drop across the sample with a sufficiently small gas velocity is the viscous resistance to the fluid flow and this can be described by Darcy’s Law [128]. Darcy’s law is an equation that relates the flow rate across the porous medium to the pressure resulting from that flow rate. The relationship is proportional and the proportionality constant includes the gas permeability as shown in Equation (3.1):

$$\frac{\Delta P}{L} = \frac{\mu}{k} v \tag{3.1}$$

The velocity of the gas can be obtained as follows:

$$v = \frac{Q}{\pi \frac{D^2}{4}} \tag{3.2}$$

It is evident from Equation (3.1), the permeability (k) can be obtained as follows:

$$k = \frac{\mu v L}{\Delta P} \tag{3.3}$$

where ΔP is the pressure drop across the sample, L is the thickness of the sample, μ is the dynamic fluid viscosity of the nitrogen gas at the test temperature, v is the velocity of the flowing gas, Q is the volumetric flow rate and D is the diameter of the sample exposed to the flow. Nonetheless, at higher gas velocities, it is important to consider the inertial resistance as it becomes significant. The modified version of Darcy's law, which also known as the Forchheimer equation, is used to account for the inertial pressure loses,

$$\frac{\Delta P}{L} = \frac{\mu}{k} v + \beta \rho v^2 \tag{3.4}$$

where ρ is the density of the flowing nitrogen and $\beta$is the inertial (also called the non-Darcy or Forchheimer) coefficient. In this thesis, Darcy's law is employed since the flow rate used were sufficiently low (Reynolds number < 3) that the relationship between the pressure drop and the flow rate was almost linear [140]. It should be noted that the calculated values of the through-plane gas permeability reported in this investigation are the result of averaged values of six samples for each GDL material with the 95% CI around the mean value.

3.4.2 Heating setup

Figure 3.12 shows the tube furnace (VCTF, Vecstar Ltd, UK) used to heat the GDL samples. The maximum temperature available for the furnace is 1200 °C. All the six samples for each GDL material were heated at 200 °C, 500 °C and 800 °C for one hour. Nitrogen gas was flowed through the tube of the furnace to avoid any oxidation for the samples. The gas permeability of the GDL samples was experimentally measured before and after the heating process at the above temperatures to evaluate the effects of high temperatures.

To justify the change in the gas permeability after heat-treatment, the GDL samples were imaged using the scanning electron microscope (SEM) to capture the superficial morphological changes. The model of the SEM was JEOL JSM-601LA, see Figure 3.13.

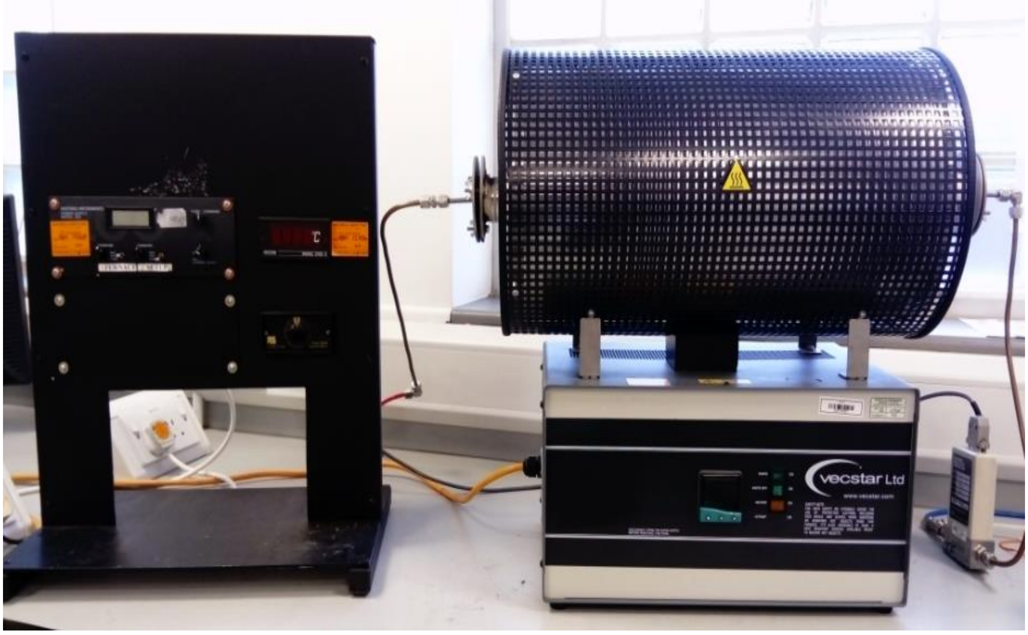

Figure 3.13: A photograph of the tube furnace used for heat treatment.

Figure 3.14: Photograph of the SEM equipment used for image-processing.

3.5 CHAPTER SUMMARY

To summarize, this chapter provides the research objectives and methodology employed in the water and thermal management inside transparent PEM fuel cell experimental investigations. The description of the main equipment used in the experimental investigation, namely the FCTS, visualization equipment and gas permeability were the main subjects in this chapter.

CHAPTER 4

VISUALIZATION OF THE LIQUID WATER

In this chapter, the PEM fuel cell has been operated and tested in order to investigate the effect of various operating conditions on the performance of the PEM fuel cell. There has been a great deal of research to experimentally and numerically investigate the effects of the operating conditions on the performance of PEM fuel cell [57], [72]–[80]. However, to the best of my knowledge, there has been no investigation that has qualitatively and quantitatively related the operating conditions to water formation and dynamics in both the cathode and anode flow channels in a simultaneous manner. Also, in this thesis, a new parameter, termed the wetted bend area ratio, has been introduced. This parameter has been used as an indicator of how flooded are the serpentine flow channels. It is defined as the ratio between the number of the bends flooded with water and the total number of bends in a serpentine flow field channel. The formation and accumulation of water was found to be more profound at the bends of the serpentine flow channels and this is mainly due to the relatively large contact area between the water and the walls which subsequently results in an increased viscosity force of water [159].

Notably, most of the visualization studies have been limited to a quantitative description of liquid water, e.g. mist, droplet, slug and film; see for example [85], [94]–[101]. There have been very few investigations that were attempted to provide a quantitative indicator on how flooded the channels are and they are limited to specific PEM fuel cell designs and configurations. Furthermore, the investigations which have simultaneously visualized the cathode and the anode fuel cells under various operating conditions are very few [60], [84], [155], [156]. Rahimi-Esbo et al. [88] designed a transparent PEM fuel cell to study the water management and contact resistance under dead-end and open-end modes of operation. They showed that, for the dead-end mode of operation, the intervals between the purge time should be short enough, say less than 5 seconds in order not to allow liquid water to accumulate in the flow channels and degrade the fuel cell performance. Bhaskar et al. [149] visualized the transport of liquid water in a transparent bio-inspired PEM fuel cell. They found that the bio-inspired fuel cell performed better than the conventional one. Hussaini et al. [157] visualized water flooding at the cathode using direct optical photography. They introduced a quantitative indicator that has been termed as the "wetted area ratio". However, in their investigation, they limited the time of operation to 30 minutes, which may not be sufficient to reach steady state operation. Yamauchi et al. [158] estimated the water content in the flow channels under different levels of humidity using a 3-pass serpentine type-flow channel flow configuration. They analysed the water flooding phenomena at the anode side and found that it mainly occurs because of water diffusion from the cathode electrode to the anode electrode through the membrane under the condition of low humidity. Ous et al. [82] estimated the amount of water in the flow channels at the cathode and anode sides of a transparent PEM fuel cell under different operating conditions. They did so by estimating the contact angles and the diameter of the water droplets through image processing, and subsequently substituting them into Young's equation to calculate the volume of liquid water. They reported that the air and hydrogen flow rates contributed similarly to the water formation at the cathode channels but differently to the water extraction. Bozorgnezhad et al. [85] investigated two-phase flow in the cathode side at different operating conditions. They focussed on the analysis of the pattern of the two-phase flow i.e. droplets, film, slug and plug, and how their formations are affected by the operating conditions. Another recent investigation that employs direct utilization was performed by Yuan et al. [156]. The fuel cell used was a direct methanol fuel cell (DMFC) and they investigated the effects of different flow fields on the fuel cell performance. They found that the oxygen flow rate has a negligible effect with the cathode serpentine flow field but produces clearer performance differences in the case of a parallel flow field.

Hence in this chapter, the newly-introduced parameter, i.e. the wetted bend ratio, will be employed to give an indication on how flooded the flow channels are and subsequently explain the variations in the performance of the fuel cell as the operating conditions of flow rates, operating pressure and relative humidity at both sides change. To achieve this, direct optical photography, which is characterised by excellent spatial and temporal resolution [14], will be employed.

4.1 EXPERIMENTAL TEST SETUP

All the visualization experiments were carried out using a commercial transparent PEM fuel cell, CPK202 ClearPak (Pragma Industries). It is a single cell with a single-pass serpentine and the active area is 25 cm^2. The current collectors of the above fuel cell were made from gold plated copper. According to the manufacturer, the electrolyte used is Nafion with a thickness of 25 µm, and the catalyst loading is 0.3 mg Pt/cm^2 at the anode and 0.6 mg Pt/cm^2 at the cathode. The temperature of the fuel cell was not controlled and therefore it was assumed to be similar to that of the room temperature. An in-house fuel cell test station is used to operate the PEM fuel cell, see Fig. 3.3. Bubble humidifiers have been used in the test station. Such types of humidifiers are characterised by: ease of operation and the demand of small power. However, the main issue with such humidifiers is that the gas-vapour mixture may condense along the gas tube before entering the fuel cell. This could be prevented by making the temperature of the downstream gas tube slightly higher than that of the bubble humidifier. The humidifier is made from stainless steel and has a capacity of 0.5 litre. The range of operation in terms of temperature and pressure are 20 to 85 °C and 0 to 2.5 barg, respectively. The pressures at the two compartments of the fuel cell are controlled by the mass flow controllers (HFC 202, Teledyne Hasting Instrument) installed at the upstream section of the fuel cell test station. The performance of the PEM fuel cell, in the form of potentiostatic, galvanostatic and polarisation curves was captured using GAMRY 3000 coupled with 30k GAMRY booster. In order to simultaneously visualize the formation, accumulation and transport of liquid water in both the cathode and anode flow channels, two high-resolution digital cameras (Casio EXF1 and Canon EOS 80D) were used.

In this study, as mentioned above, a new parameter, called the wetted bend ratio, is introduced, and the wetted area ratio adopted from [157] is also utilized. Fig. 4.1 shows a schematic diagram of the experimental setup. Before concluding this section, I would like to emphasize that all the experiments were repeated at least twice in order to confirm the repeatability of the results and the reliability of the findings.

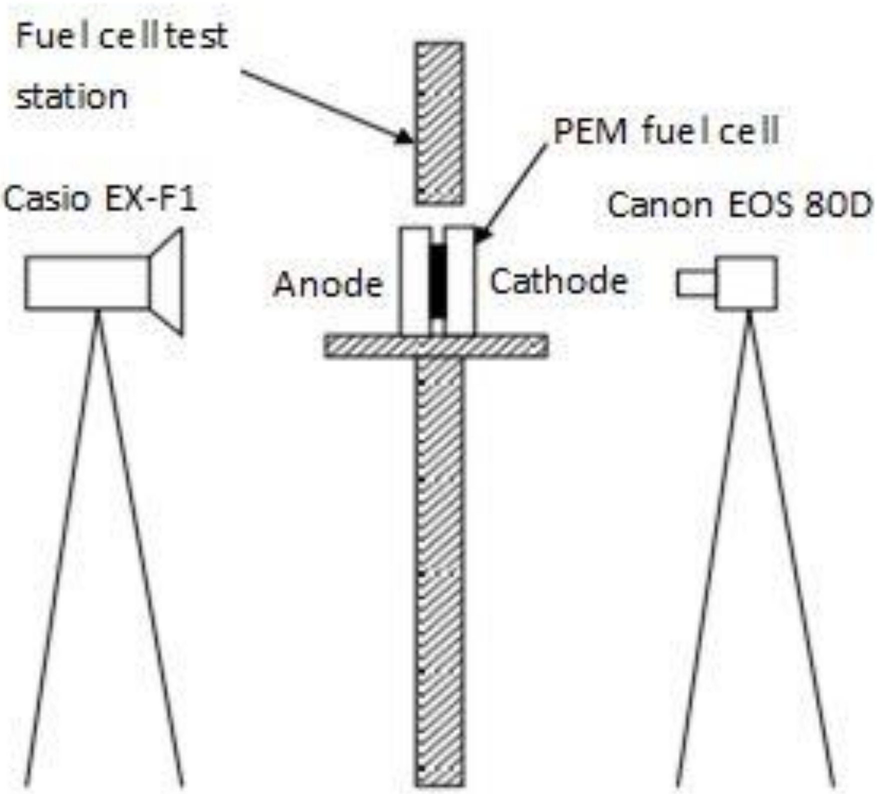

Figure 4.1: Schematic diagram of the experimental setup used to visualize the liquid water.

4.2 WETTED BEND RATIO AND WETTED AREA RATIO

A new parameter extracted from the captured images, the wetted bend ratio has been introduced as an indicator of the amount of liquid water present at the bend of the flow channel. This parameter, along with wetted area ratio [157] is used to explain the variation in the fuel cell performance as the operating conditions of flow rates, operating pressure and relative humidity change. The wetted bend ratio can be simply calculated by counting the bends that are occupied by liquid water and then dividing them by the total number of bends, i.e. 20. On the other hand, the wetted bend area ratio is calculated by measuring the total length of the water-covered areas of the channel and then dividing it by the entire length of the channel; see Fig. 4.2.

The estimation of the wetted bend ratio is clearly easier than the estimation of the wetted area ratio. It should be noted that, for simplification, we consider the bend or the portion of the channel to be wet when there is an existence of a considerable amount of liquid water in these regions.

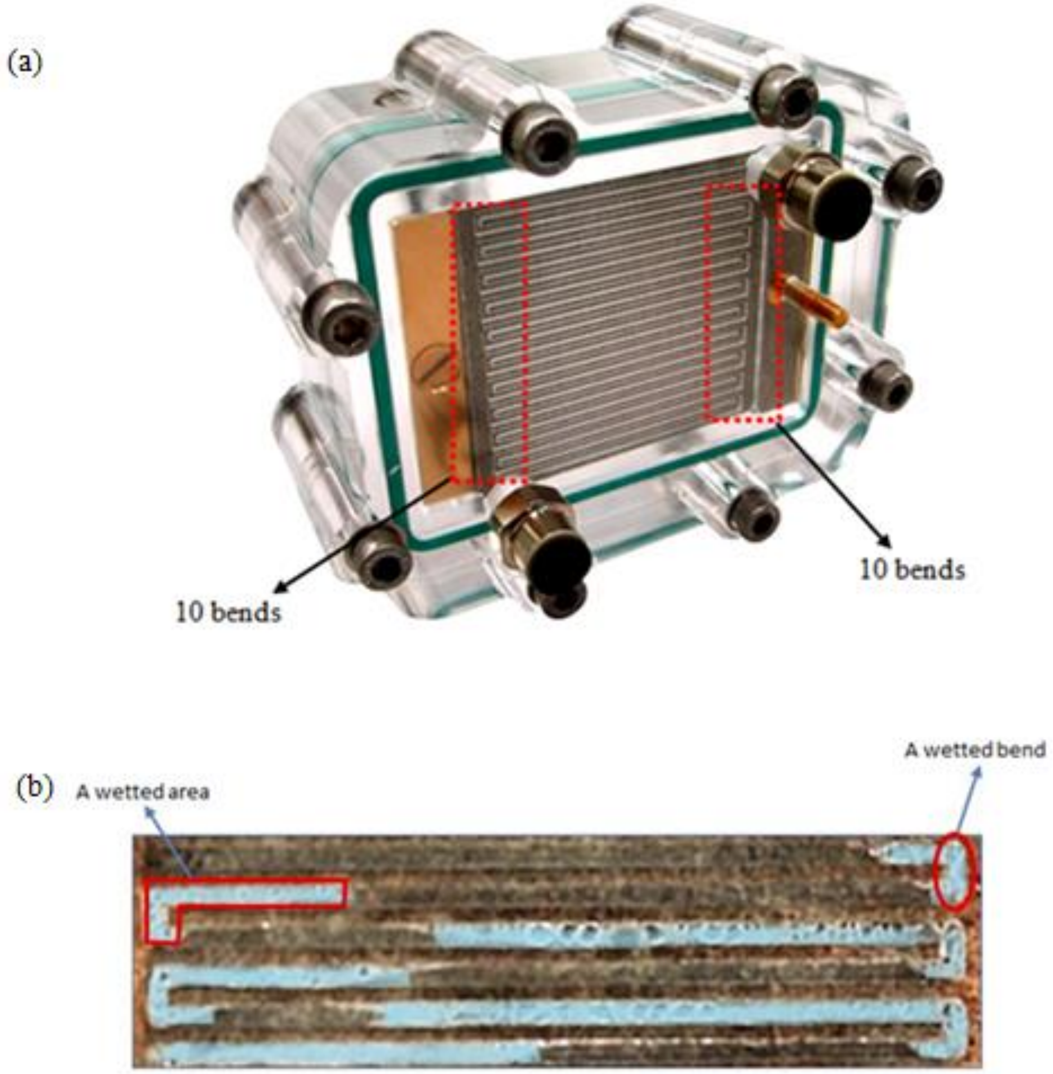

Figure 4.2: (a) A photo of the used transparent fuel cell showing the number of the total bends, i.e. 20 [160] and (b) an image that shows how wetted areas in the flow channel.

4.3 EFFECT OF THE FLOW RATES

Two sets of experiments were carried out to study the effect of the gas flow rates on the PEM fuel cell performance and the status of the liquid water in the flow channel. The first set of experiments is concerned with the effects of the air flow rate; the set of air flow rates used were: 0.10, 0.15, 0.20 and 0.25 Standard Litre Per Minute (SLPM) while the hydrogen flow rate has been kept constant at 0.05 SLPM which is the theoretical hydrogen flow rate calculated based on a total current of 8 A and stoichiometric ratio of 1.5. The second set of experiments is concerned with the effects of the hydrogen flow rate; the set of hydrogen flow rates used were: 0.03, 0.05, 0.07 and 0.09 SLPM while the air flow rate has been kept constant at 0.20 SLPM which is the theoretical air flow rate calculated based on a total current of 8 A and stoichiometric ratio of about 1.3. During the experiments, the operating conditions of temperature, pressure and relative humidity, were kept constant. The gas inlet temperature and pressure on both sides were at room temperature and 1 barg, respectively. A humidity sensor as 75 % and 85 %, respectively recorded the anode and cathode gas relative humidity. The polarization and potentiostatic curves of each set of experiments have been recorded. Images for the cathode and anode flow channels for each case were taken from the recording at the same moment to examine the status of the liquid water at both sides simultaneously.

Fig. 4.3 shows the polarization curves for the cases in which the air flow rate has been changed from 0.10 to 0.25 SLPM. In general, the fuel cell performance improves as the air flow rate increases from 0.10 to 0.20 SLPM. When increased to 0.25 SLPM, the fuel cell performance has been compared to the 0.15 and 0.20 SLPM cases, and was found to be lower for the fuel cell potential above 0.60 V. However, the flow rate of 0.25 SLPM was shown to give the highest limiting current density amongst the investigated cases.

Based on the above, one can see that, for the given operating conditions, there is an existence of an optimum air flow rate, namely 0.20 SLPM. The air flow rates 0.10 and 0.15 SLPM appear to be not sufficiently high to drive the excess liquid water away from the flow channel, thus causing undesirable water accumulation that limits the performance of the fuel cell at relatively high current densities. On the other hand, the air flow rate 0.25 SLPM appears to be so high, and this affects the level of hydration needed for the membrane. These findings will be confirmed later in this section through the recorded images of the flow channels and the calculated water ratio numbers.

To investigate the status of the liquid water in the flow channels, the potentiostatic curves were generated at 0.70 V which was found to be the minimum reasonable cell voltage for all the cases before the introduction of the mass transport losses, see Fig. 4.4. As with the corresponding polarization curve, it can be seen that, after reaching almost the ‘pseudo’ steady-state condition, the best fuel cell performance is when the air flow rate is 0.20 SLPM and is the worst when the air flow rate is 0.10 SLPM.

The wetted bend ratio and wetted area ratio for both sides have been calculated from the captured images, see Fig. 4.5 and Fig. 4.6, and plotted in Fig. 4.7 and Fig. 4.8. It can be seen that they both decrease as the air flow rate increases. As indicated earlier, this is most likely to be due to the increase in the ability to remove liquid water from the flow channel with increasing air flow rate. Since water is produced at the cathode, the wetted ratio numbers at the anode are smaller than those of the cathode. However, their trends are similar to each other even though the hydrogen flow rate has been kept constant. This may be attributed to the net water transport across the membrane through the electro-osmotic drag and the back diffusion. This indicates that the wetted ratio numbers at the anode side can also be employed to interpret the relationship between the fuel cell performance and the air flow rate.

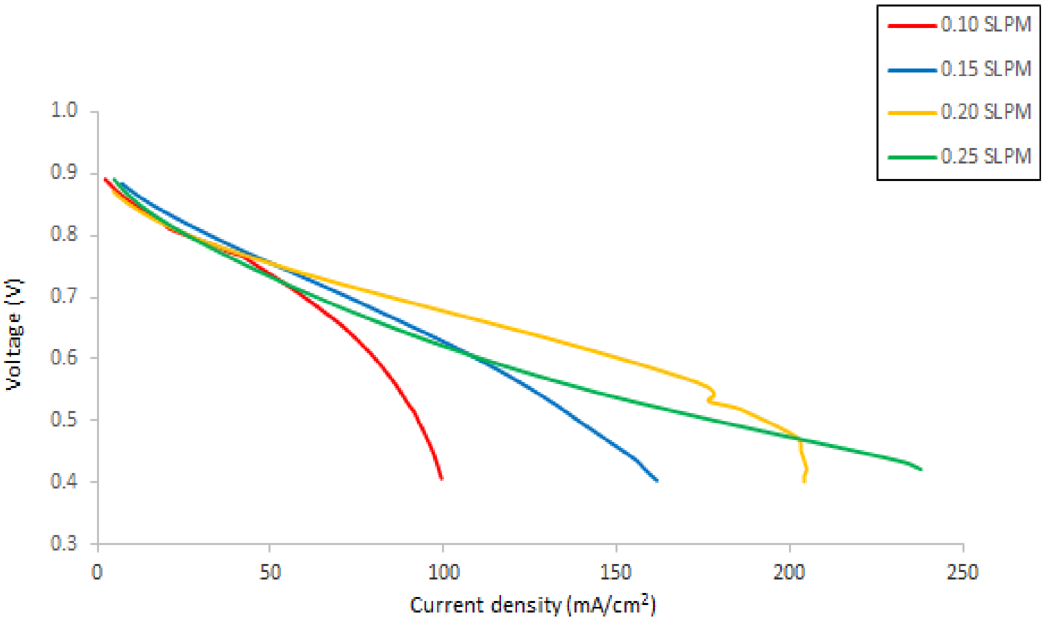

Figure 4.3: The polarization curves for all the investigated air flow rates.

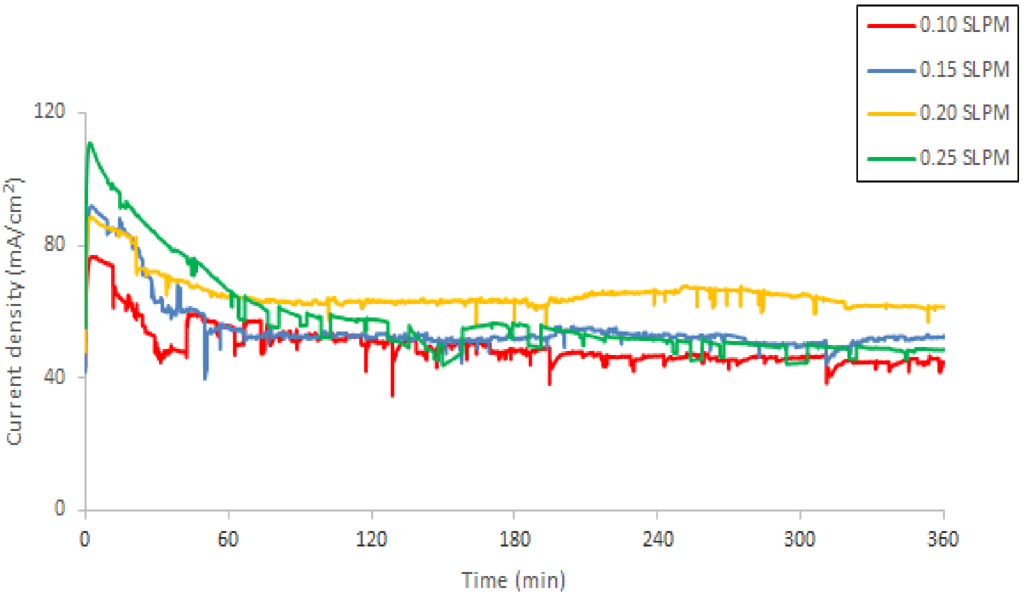

Figure 4.4: The measured current density at 0.70 V as a function of time for all the investigated air flow rates.

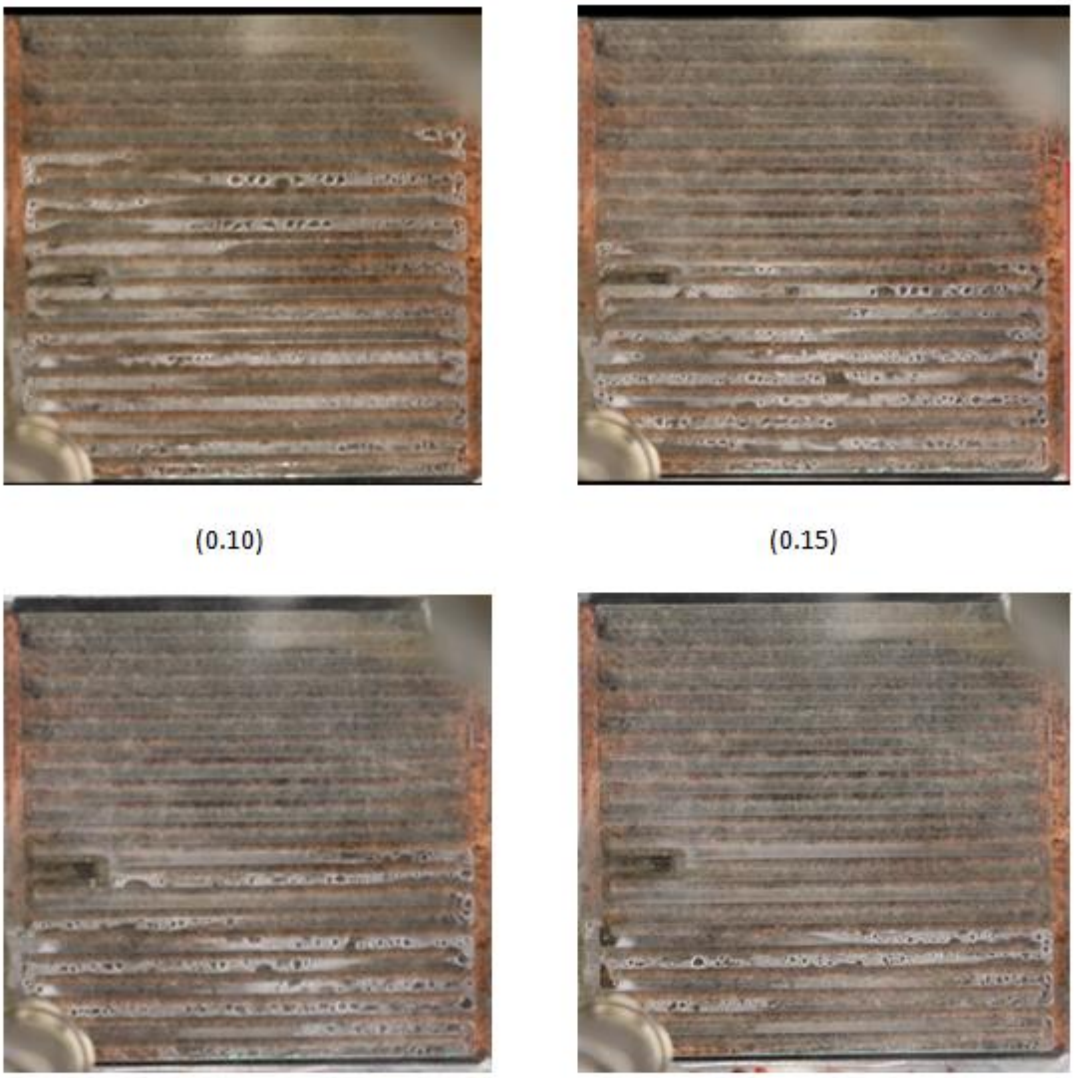

(0.10) (0.15)

(0.20) (0.25)

Figure 4.5: The captured images at the cathode side for all the investigated air flow rates.

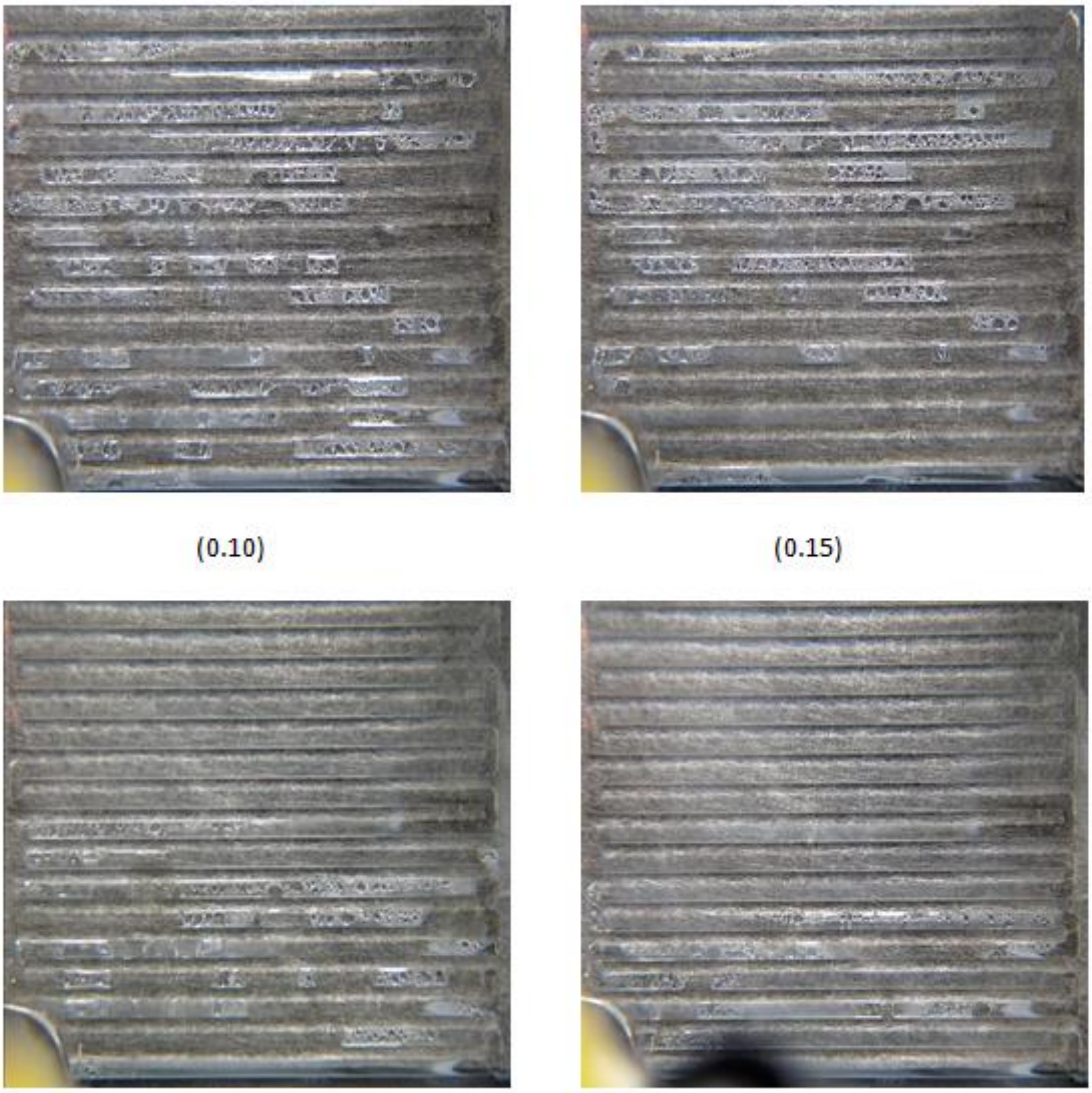

(0.10)

(0.15)

(0.20)

(0.25)

Figure 4.6: The captured images at the anode side for all the investigated air flow rates.

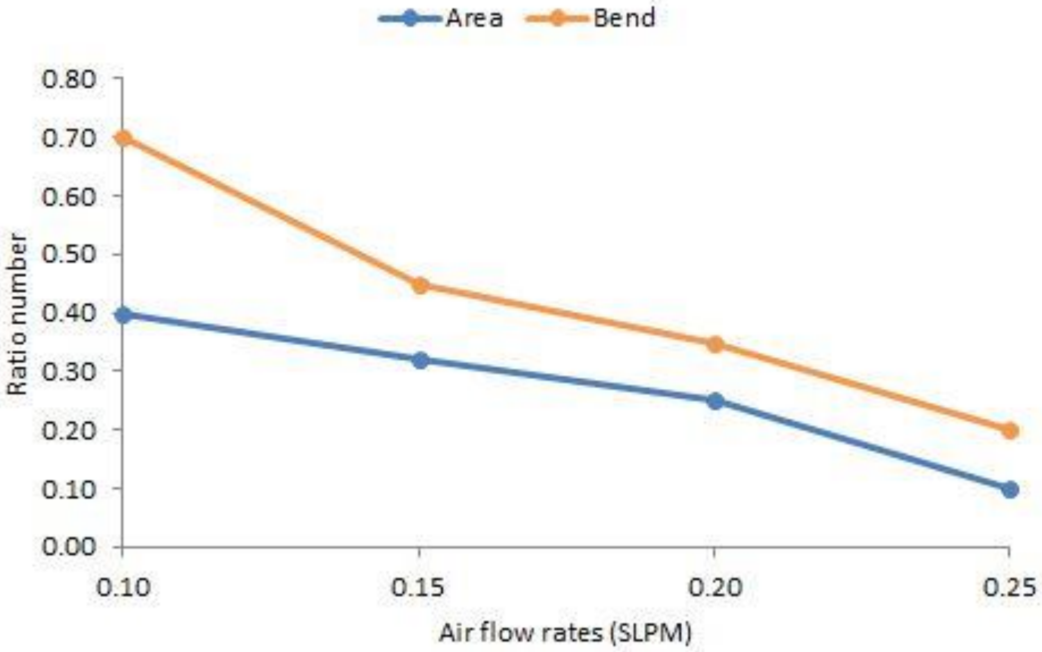

Figure 4.7: The wetted area and bend ratio numbers for the cathode side.

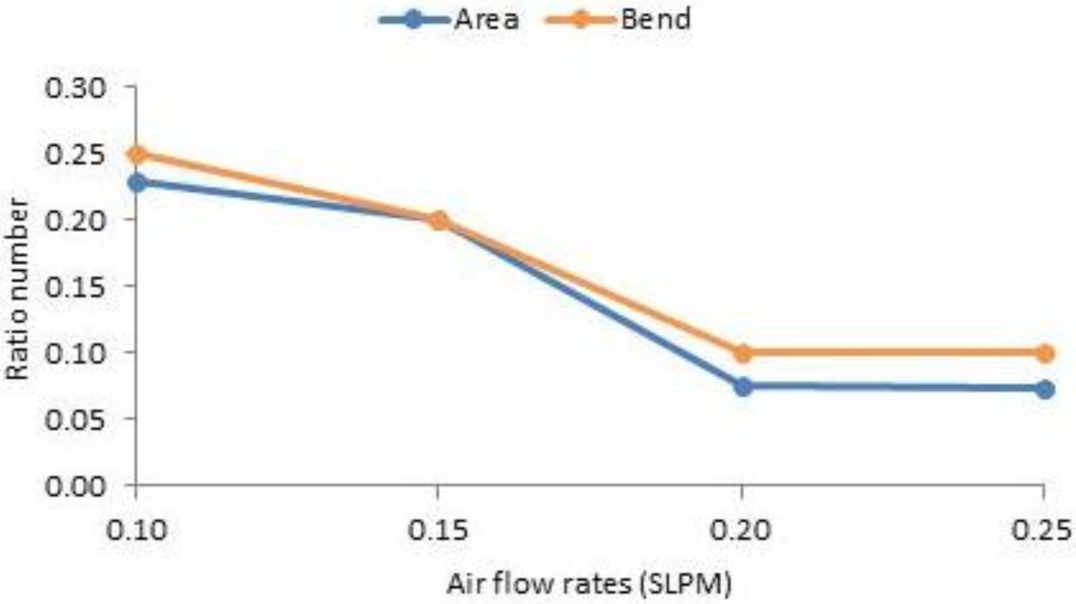

Figure 4.8: The wetted area and bend ratio numbers for the anode side.

Fig. 4.9 shows the polarization curves for the cases in which the hydrogen flowrate has been changed from 0.03 to 0.09 SLPM. It can be seen from the figure that the hydrogen flow rate of 0.07 SLPM gives the maximum limiting current density amongst all the investigated cases; this is probably due to the observation that the number of flooded bends in this case is the minimum.

Also, the hydrogen flow rate of 0.03 and, to a less extent, 0.05 SLPM appear to be insufficient to maintain the fuel cell operating after 100 and 200 mA/cm^2, respectively. Futher, ignoring the limiting current densities, the best performance was shown when the fuel cell was supplied with 0.05 SLPM hydrogen gas. As with the cathode side, the potentiostatic curves for all the cases were recorded at 0.70 V in order to investigate the status of the liquid water in the flow channels, see Fig. 4.10. In accordance with the polarization curves at 0.70 V, the highest current density, at pseudo steady-state conditions, was shown when the fuel cell was run with a hydrogen flow rate of 0.05 SLPM and the lowest current density was when it was run with a hydrogen flow rate of 0.07 SLPM.

Fig. 4.13 and 4.14 show the wetted ratio numbers calculated from the captured images, see Fig. 4.11 and Fig. 4.12 for the cathode and anode flow channels at 0.70 V for the cases in which hydrogen flow rate has been changed from 0.03 to 0.09 SLPM. The wetted ratio numbers at the cathode, Fig. 4.13 can be somewhat related to the trends shown in the potentiostatic curves, see Fig. 4.10: the larger is the current density at 0.70 V, the higher are the wetted ratio numbers (either for the entire channel or the bends) at the cathode side. This is expected since more water is generated as the current produced increases. However, there are almost no apparent trends that can be deduced from the wetted ratio numbers at the anode side (Fig. 4.14) as the hydrogen flow rate increases; the wetted bend ratio is the same for all the flow rates and the change of the wetted area ratio with the hydrogen flow rate is almost negligible.

Overall, for all the given operating conditions mentioned earlier, the optimum hydrogen flow rate at 0.70 V is 0.05 SLPM. It is not very clear why the current density is at a maximum with 0.05 SLPM hydrogen flow rate at 0.70 V; it may be the flow rate that supplies a sufficient amount of hydrogen to the anode electrode without removing away a subtantial amount of water from the entire membrane electrode assembly (MEA).

As a general observation, the wetted ratio numbers calculated for the bends in all the previous cases are larger than those calculated for the entire channel. This is, as explained in the introduction, attributed to the ease of accumulation of liquid water at the bends. This finding compliments the findings that have been reported in [84] and [157] as it highlights the importance of considering the design of the flow field when quantifying the liquid water in the flow channels.

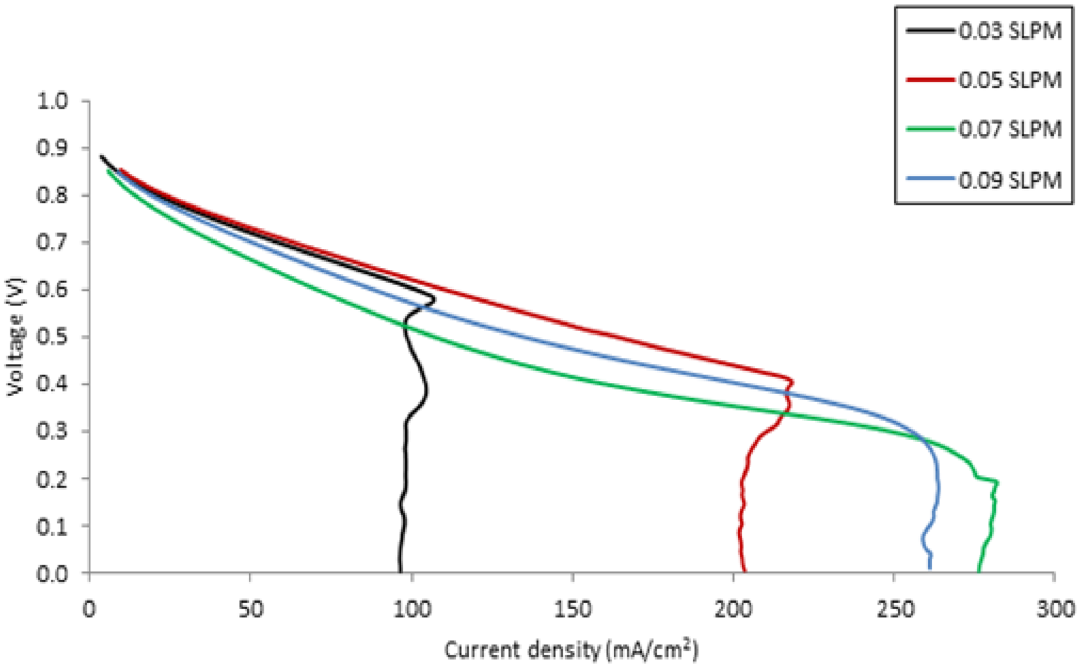

Figure 4.9: The polarization curves for all the investigation hydrogen flow rates.

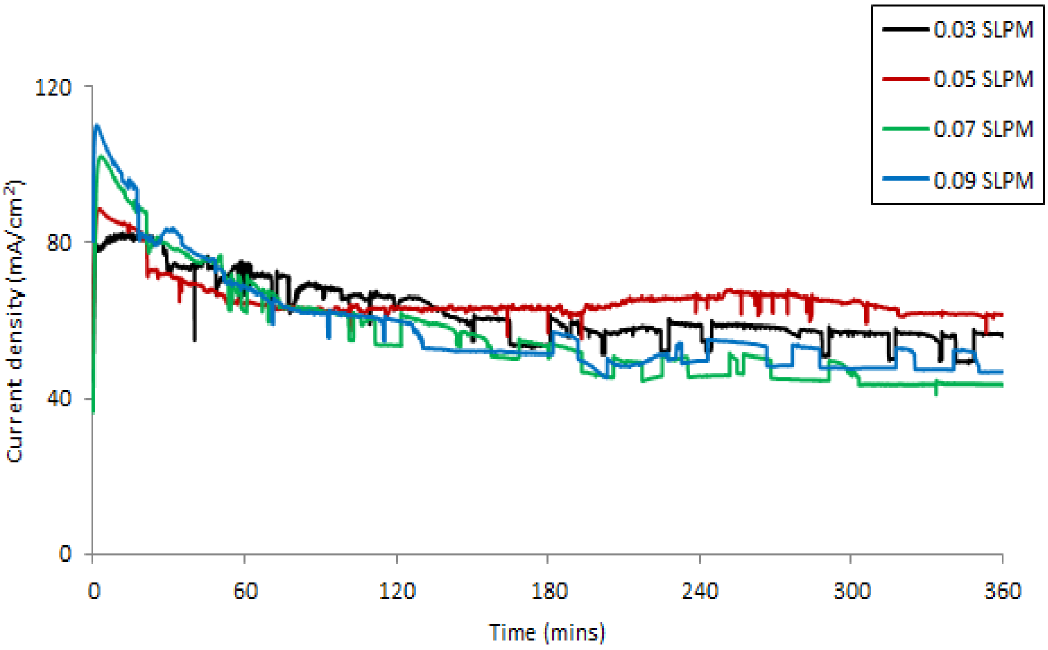

Figure 4.10: The measured current density at 0.70 V as a function of time for all the investigated hydrogen flow rates.

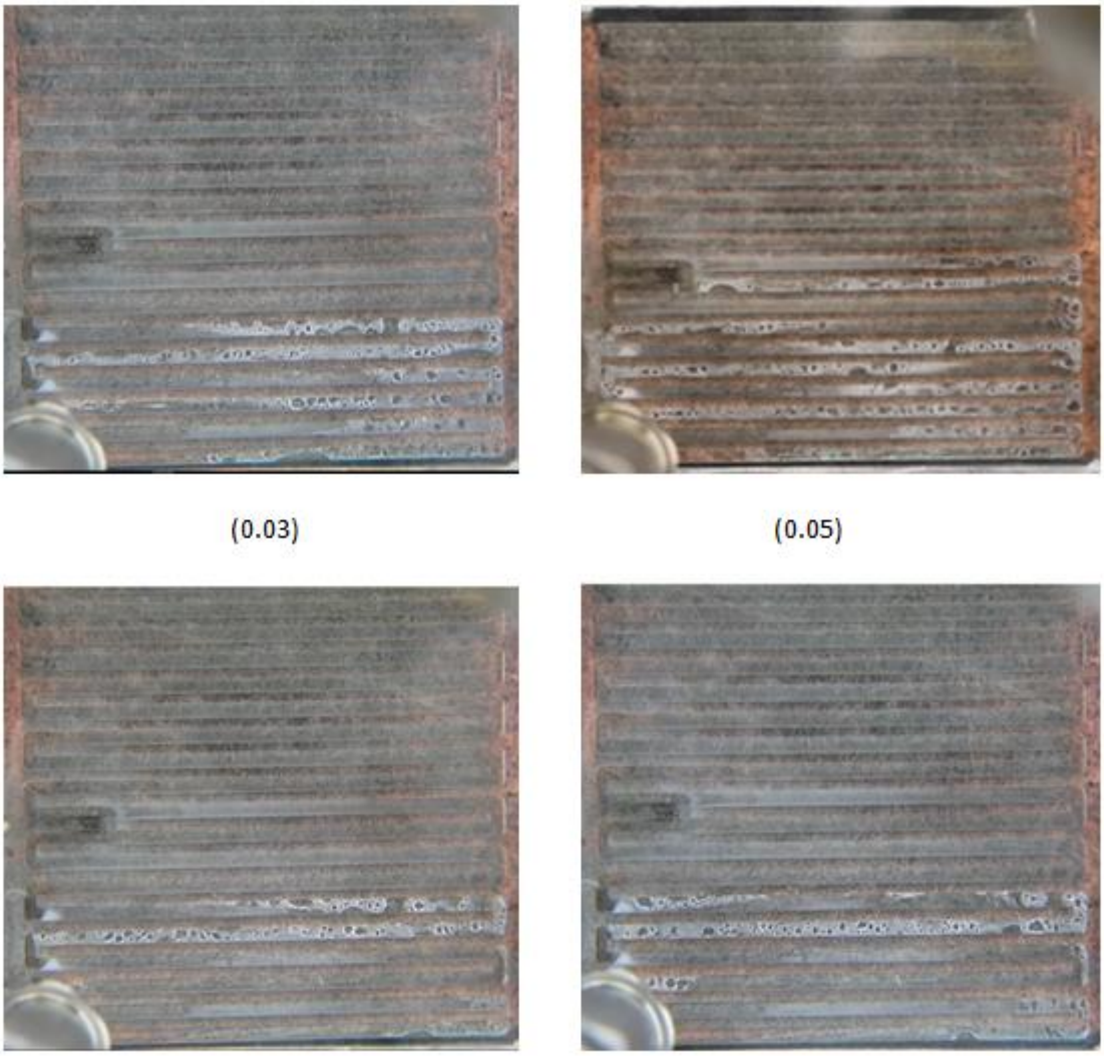

(0.03) (0.05)

(0.07) (0.09)

Figure 4.11: The captured images at the cathode side for all the investigated hydrogen flow rates.

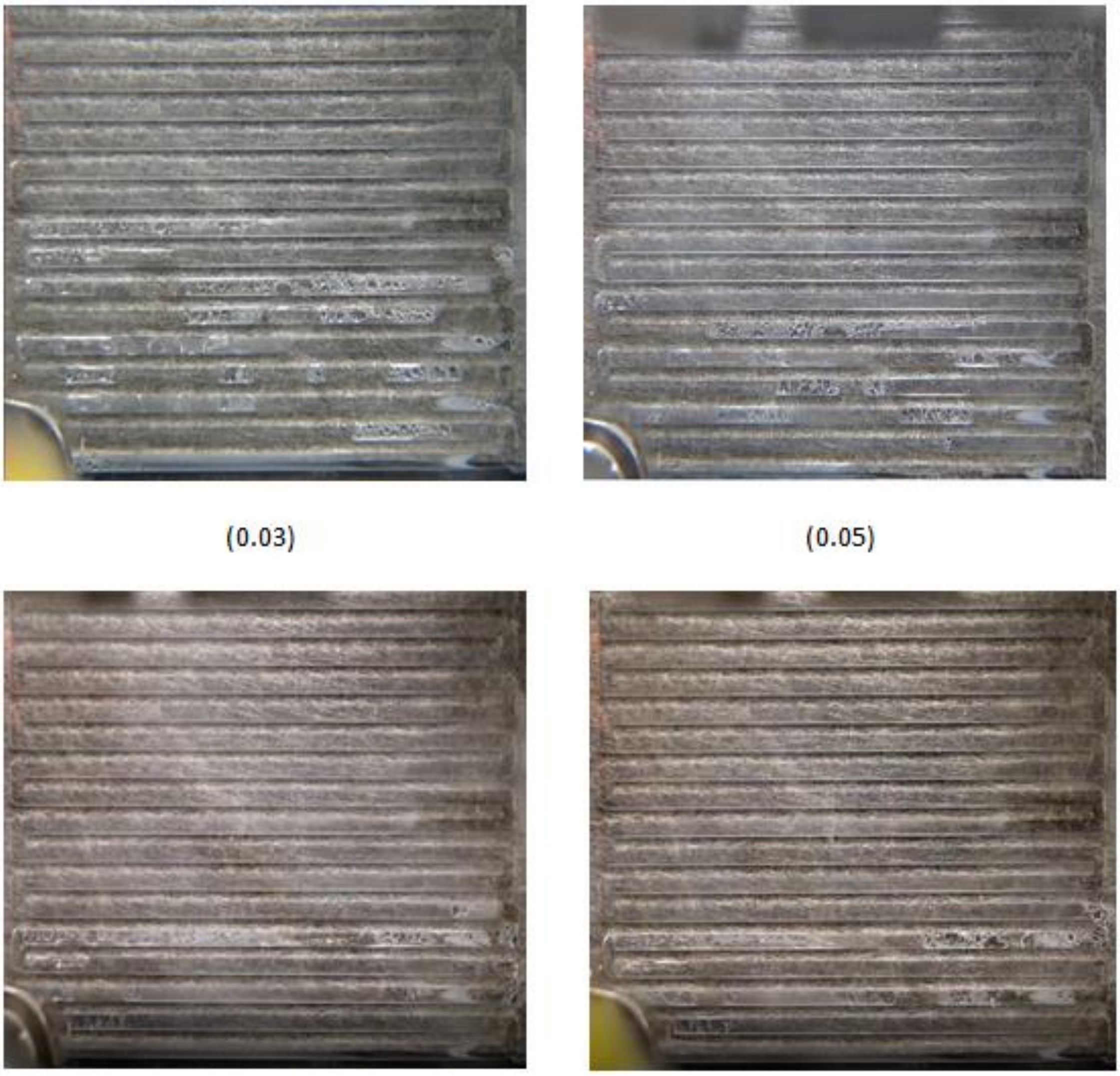

(0.03)

(0.05)

(0.07)

(0.09)

Figure 4.12: The captured images at the anode side for all the investigated hydrogen flow rates.

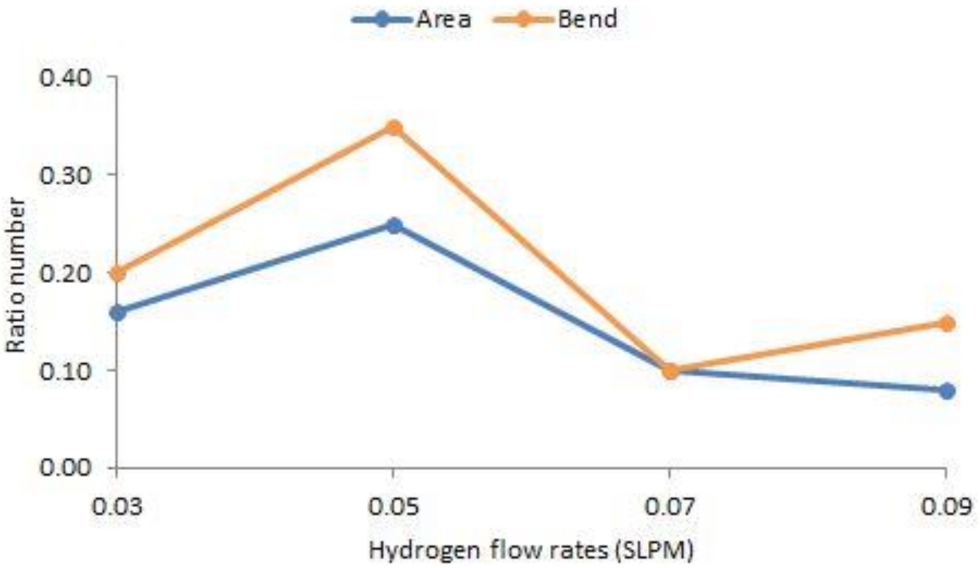

Figure 4.13: The wetted area and bend ratio numbers for the cathode side.

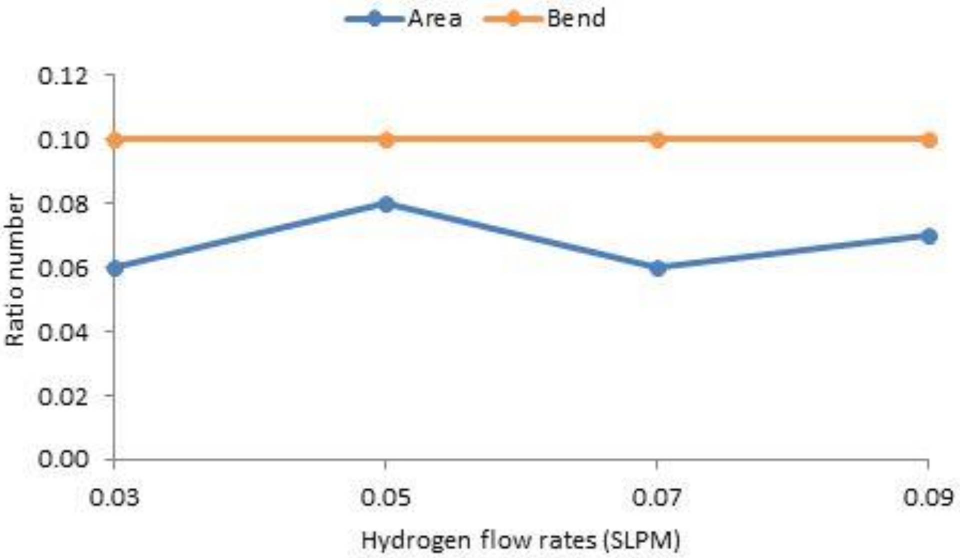

Figure 4.14: The wetted area and bend ratio numbers for the anode side.

4.4 EFFECT OF OPERATING PRESSURE

The effect of operating pressure on the fuel cell performance has been investigated. The set of pressures investigated were 0, 0.5, 1.0 and 1.5 barg on both the cathode and anode sides. It should be noted that 0 barg means that the back-pressure regulator has been set to 0 and consequently there is hardly any increase in the gauge pressure of the fuel cell. The effect of the pressure has been demonstrated in the form of the polarization and galvanostatic curve, see Fig. 4.15 and 4.16 respectively. The galvanostatic test, rather than the potentiostatic test, has been adopted in this investigation as it was shown to give more stable readings with this investigation. The constant current that has been set when performing the galvanostatic tests was 2.5 A.

As with the previous investigation of flow rates, all the other parameters were kept constant. The flow rate of air and hydrogen were 0.20 and 0.05 SLPM, respectively. From Fig. 4.15, one can see that the fuel cell performance in general enhances as the operating pressure increases; this is in accordance with the previous findings reported in [114] and [145]. This is attributed to the increase in the partial pressure of the reacting gases (e.g. air and hydrogen) which subsequently increases the open circuit (or the starting) potential of the fuel cell; this is evident from the Nernst equation which is used to calculate the maximum open circuit potential [16]. Also, it can be noted that as the current density increases, the cell potentials for the cases 1.0 and 1.5 barg approach each other. Also, the same comment applies to the cases 0 and 0.5 barg. This could be explained by the increase in the mass transport losses in the former two cases, i.e. 0.5 and 1.5 barg, due to the increase in the amount of water generated at relatively high current densities.

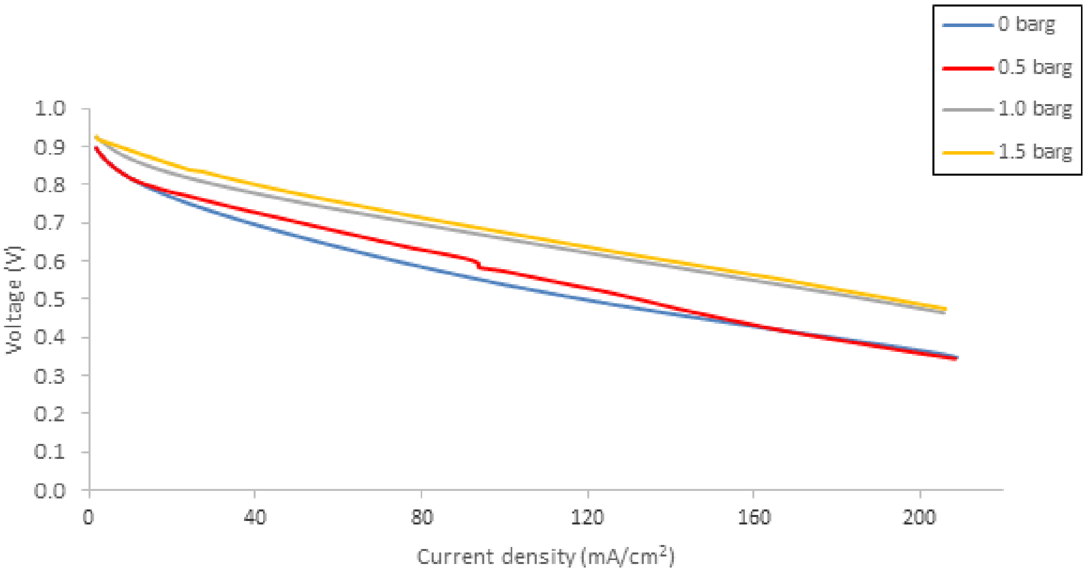

Figure 4.15: The polarization curves for all the investigated operating pressures.

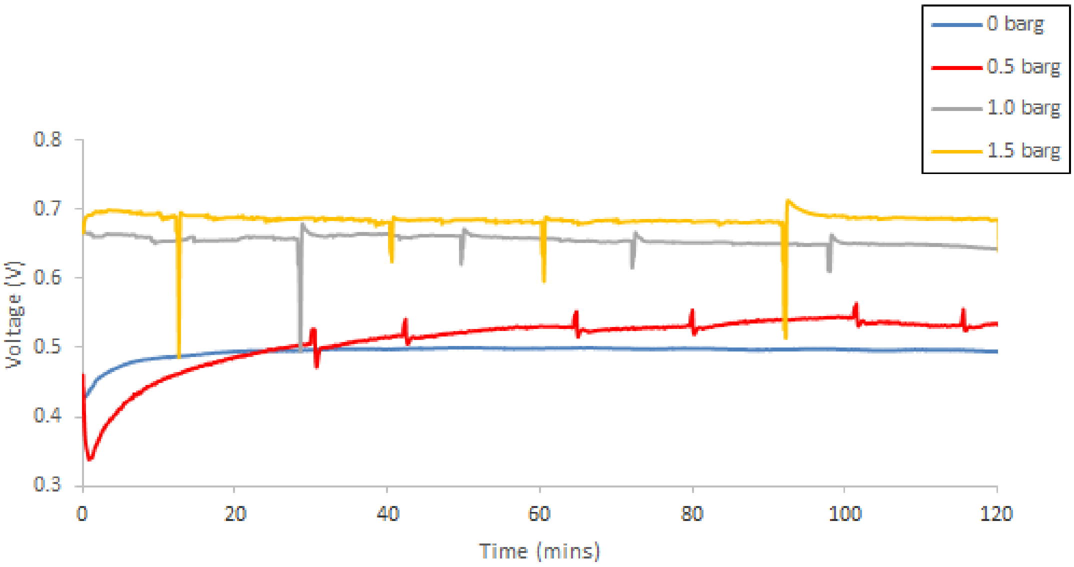

Figure 4.16: The measured cell potential at 2.5 A as a function of time for all the investigated operating pressures.

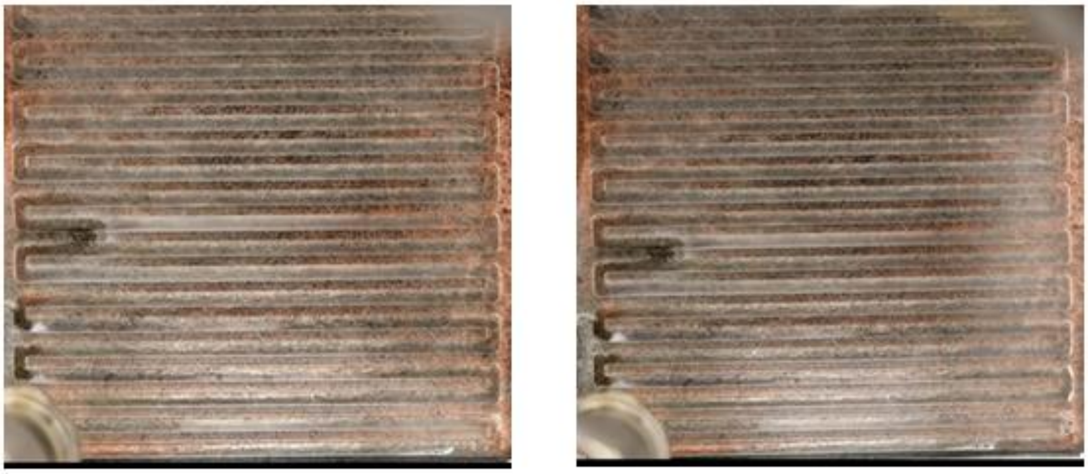

(0 Barg) (0.5 Barg)

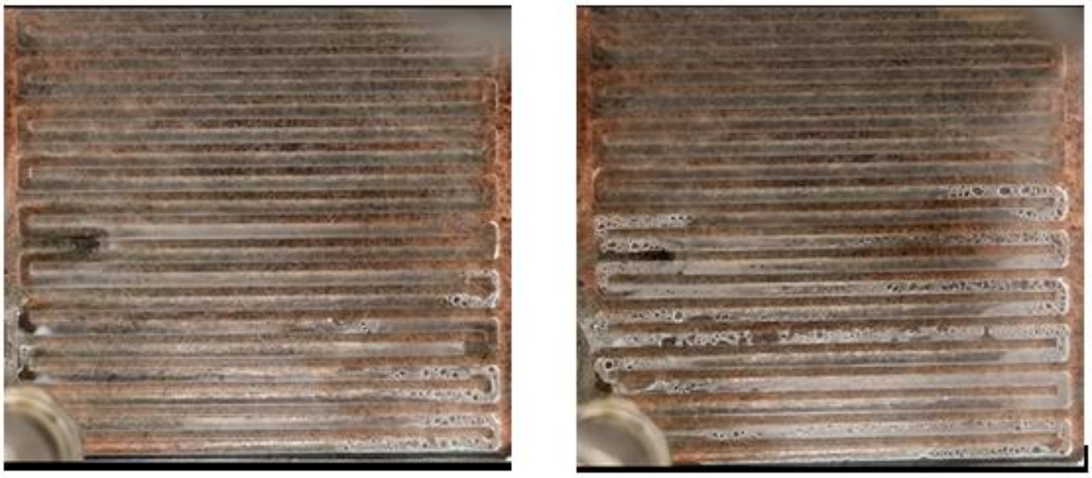

(1.0 Barg) (1.5 Barg)

Figure 4.17: The captured images at the cathode side for all the investigated operating pressures.

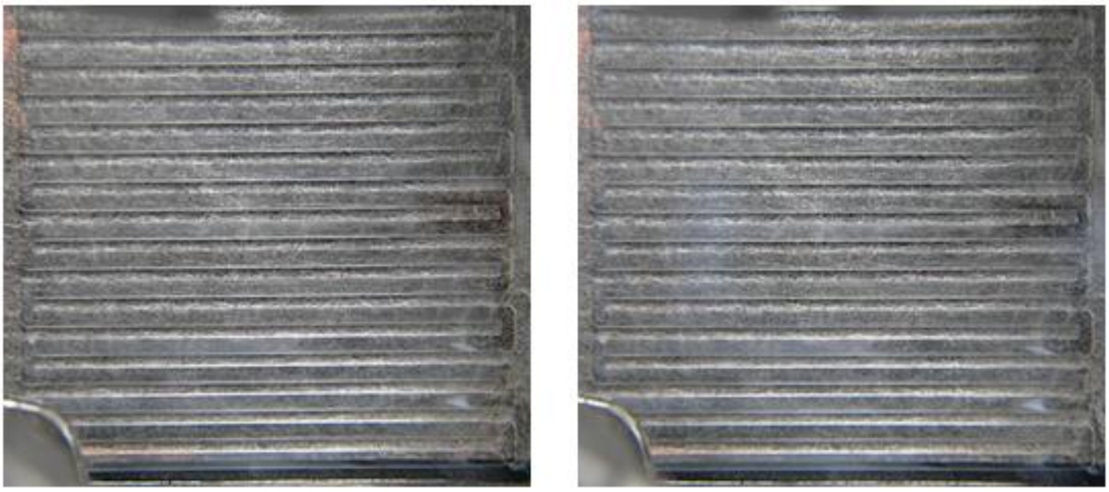

(0 Barg) (0.5 Barg)

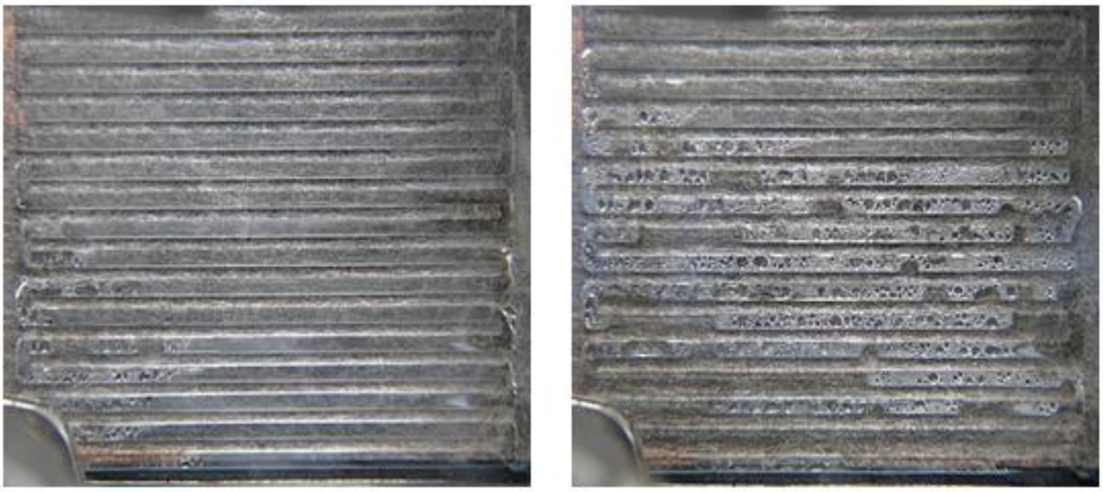

(1.0 Barg) (1.5 Barg)

Figure 4.18: The captured images at the anode side for all the investigated operating pressures.

Fig. 4.19 and 4.20 show the wetted ratio numbers calculated based on the captured images, see Fig. 4.17 and Fig. 4.18 for the cathode and the anode flow channels at 2.5 A for the cases in which the operating pressure has been changed from 0 to 1.5 barg. It can be seen from the graphs that the wetted ratio numbers increase as the operating pressure increases. As the current has been kept constant, the amount of water generated is the same for all cases. However, it is well-known that as the operating pressure, controlled by a backpressure regulator, decreases, the ability to purge liquid water from the flow channel increases.

As with the previous investigation, the similarity of the trends of the wetted ratio numbers at both the cathode and the anode indicates that these numbers at the anode side can also be employed to interpret the relationship between the fuel cell performance and the operating pressure of the fuel cell.

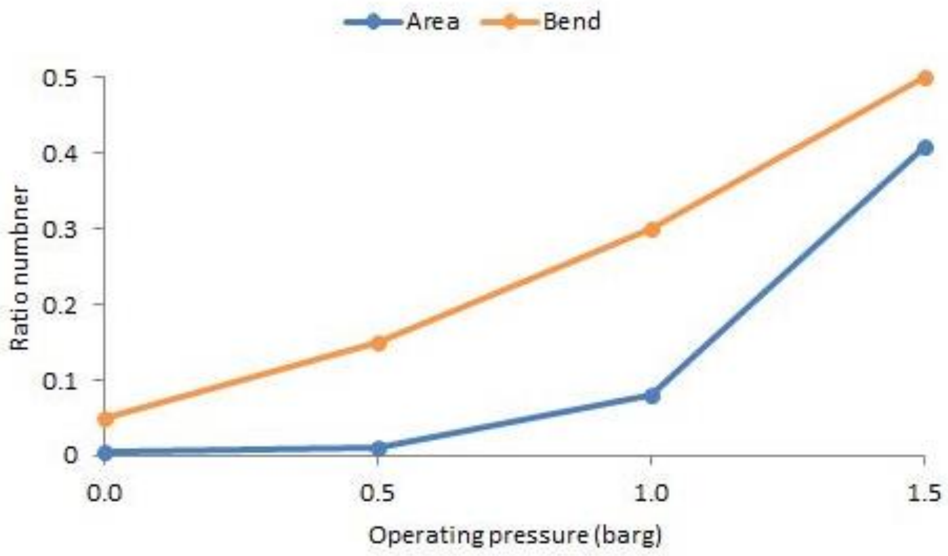

Figure 4.19: The wetted area and bend ratio numbers for the cathode side.

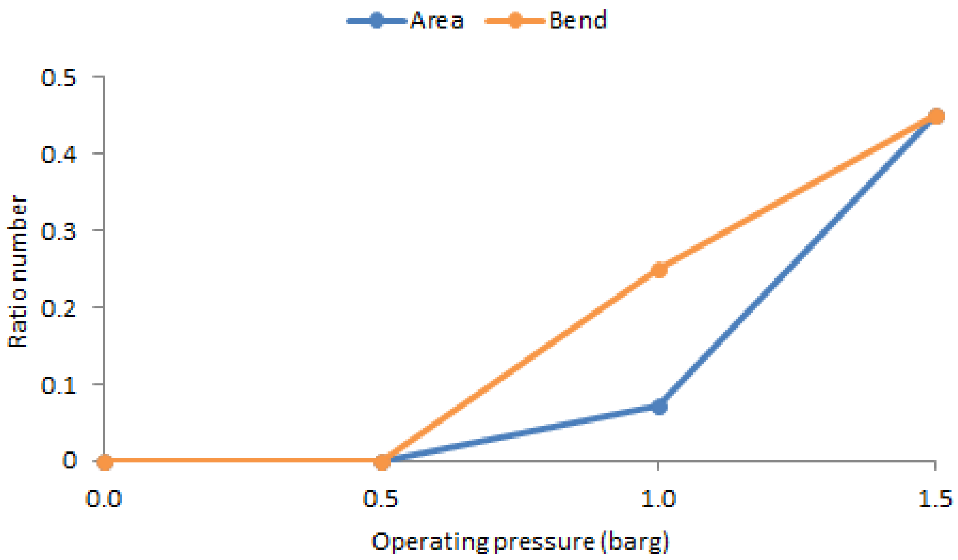

Figure 4.20: The wetted area and bend ratio numbers for the anode side.

4.5 EFFECT OF RELATIVE HUMIDITY

The effect of inlet relative humidity on the fuel cell performance has also been investigated. To achieve this, the hydrogen has been kept dry while investigating the effect of the inlet relative humidity of air and vice versa. The relative humidity data is changed by changing the temperature of the bubble humidifier while keeping the temperature of the inlet gas constant. Tables 1 and 2 list the values of the inlet relative humidity used for the cathode and anode sides, respectively.

Table 4.1: Cathode inlet relative humidity for various temperatures of the cathode bubble humidifier and a constant inlet air temperature of 45 °C.

Bubble Humidifier Temperature (°C)	Relative Humidity (%)
30	10
40	40
50	88
60	95

Table 4.2: Anode inlet relative humidity for various temperatures of the anode bubble humidifier and a constant inlet hydrogen temperature of 30 °C.

Bubble Humidifier Temperature (°C)	**Relative Humidity (%)**
40	10
50	20
55	35
60	48
70	100

Fig. 4.21 and 4.22 show the polarization and potentiostatic curves for the cases in which the relative humidity of air has been varied to investigate its effects. It can be seen from the polarization curves of all the conditions investigated, the optimum fuel cell performance was obtained at an air relative humidity of 88%; it might be the trade-off value (amongst the investigated values) between the positive effect of membrane hydration and negative effect of water accumulation. As expected, the wetted ratio numbers at the cathode side increases as the air relative humidity increases, see Fig. 4.25. A similar trend is shown at the anode side and this is due to diffusion of water from the cathode to the anode, see Fig. 4.26. These ratio numbers were calculated based on the captured images for both sides, see Fig. 4.23 and Fig. 4.24.

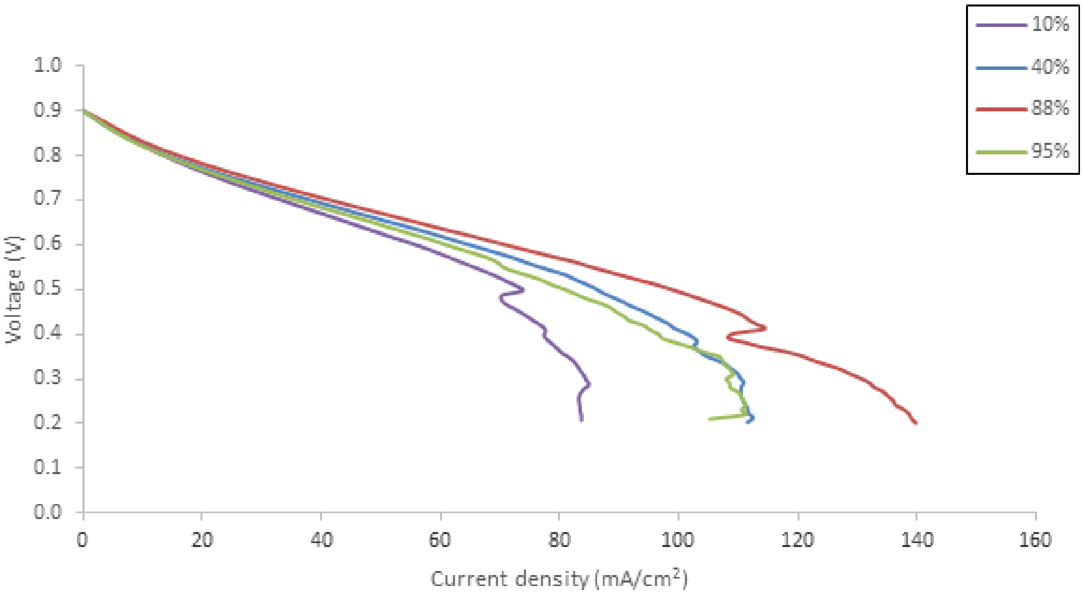

Figure 4.21: The polarization curves for all the investigated air relative humidity.

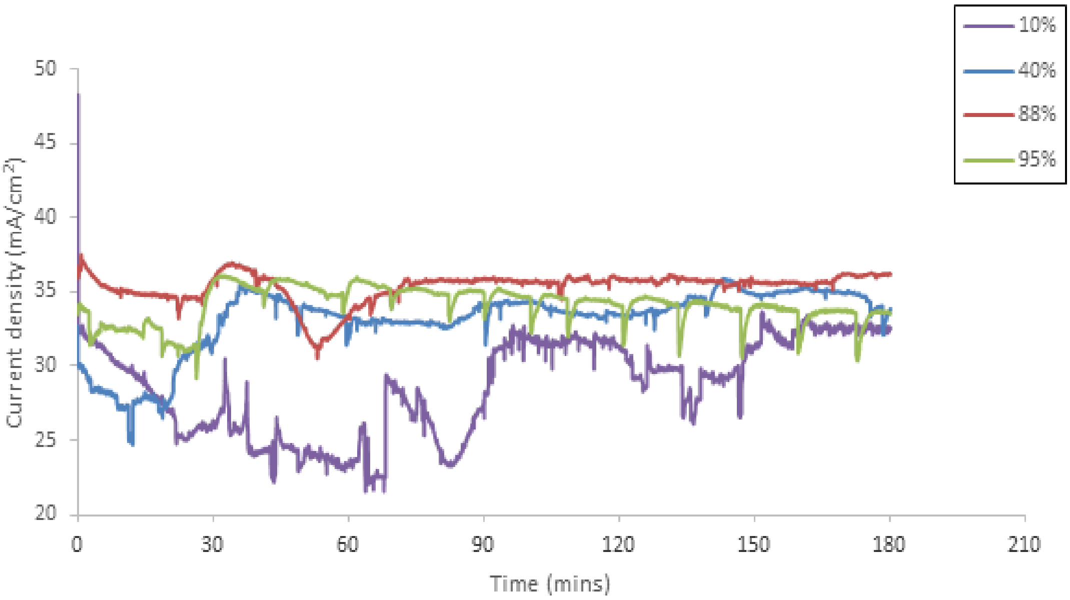

Figure 4.22: The measured current density at 0.70 V as a function of time for all the investigated air relative humidity.

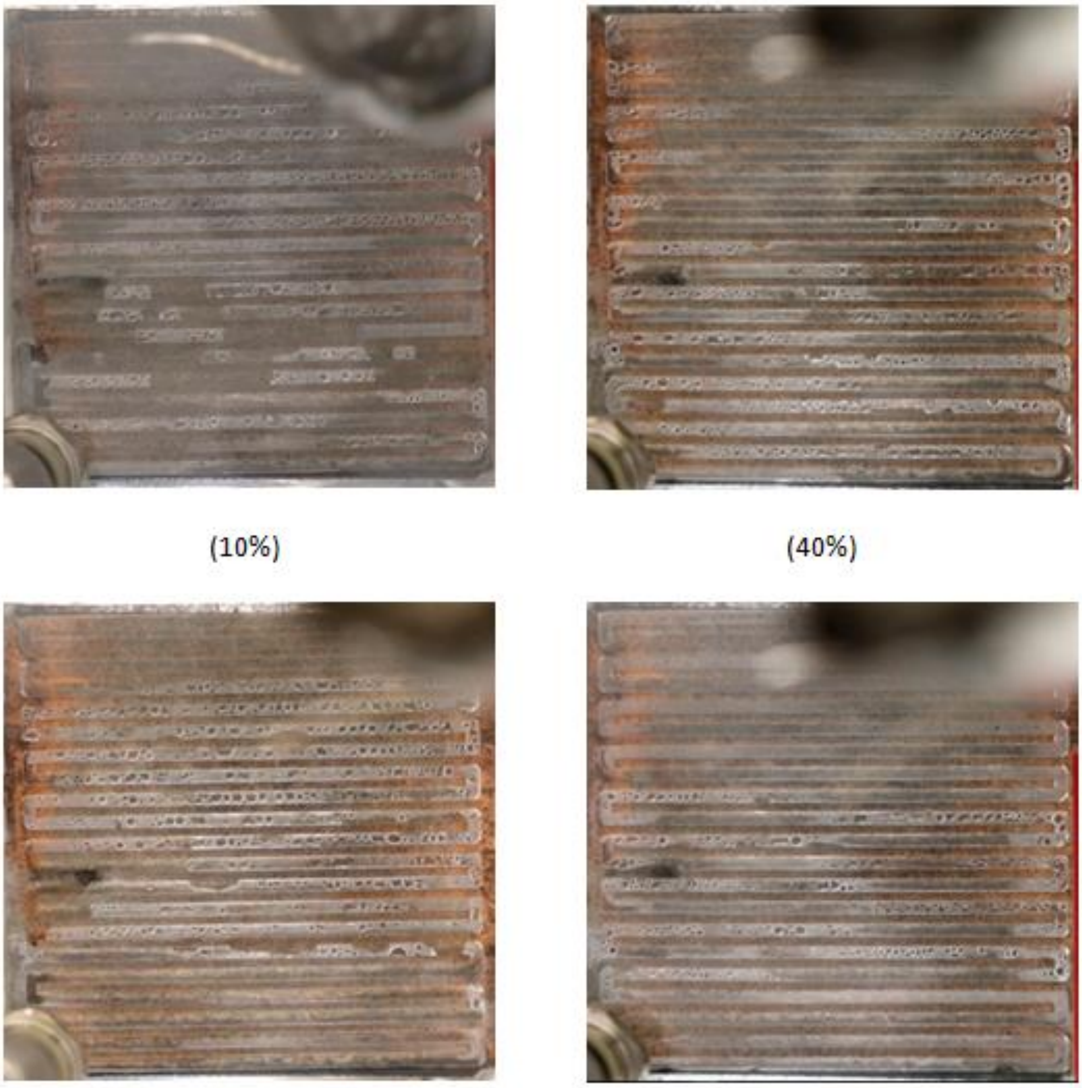

(10%)

(40%)

(88%)

(95%)

Figure 4.23: The captured images at the cathode side for all the investigated air relative humidity.

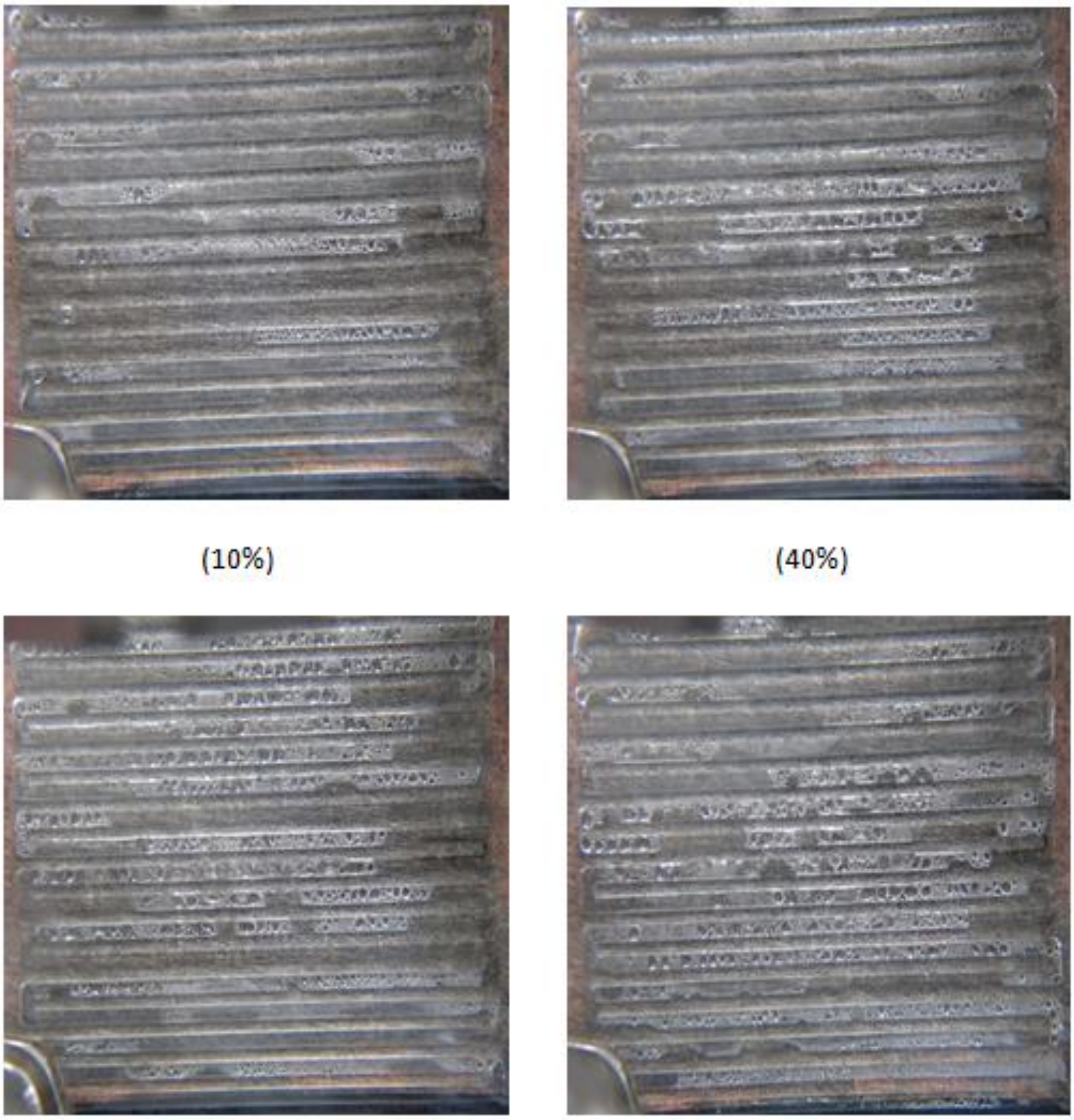

(10%) (40%)

(88%) (95%)

Figure 4.24: The captured images at the anode side for all the investigated air relative humidity.

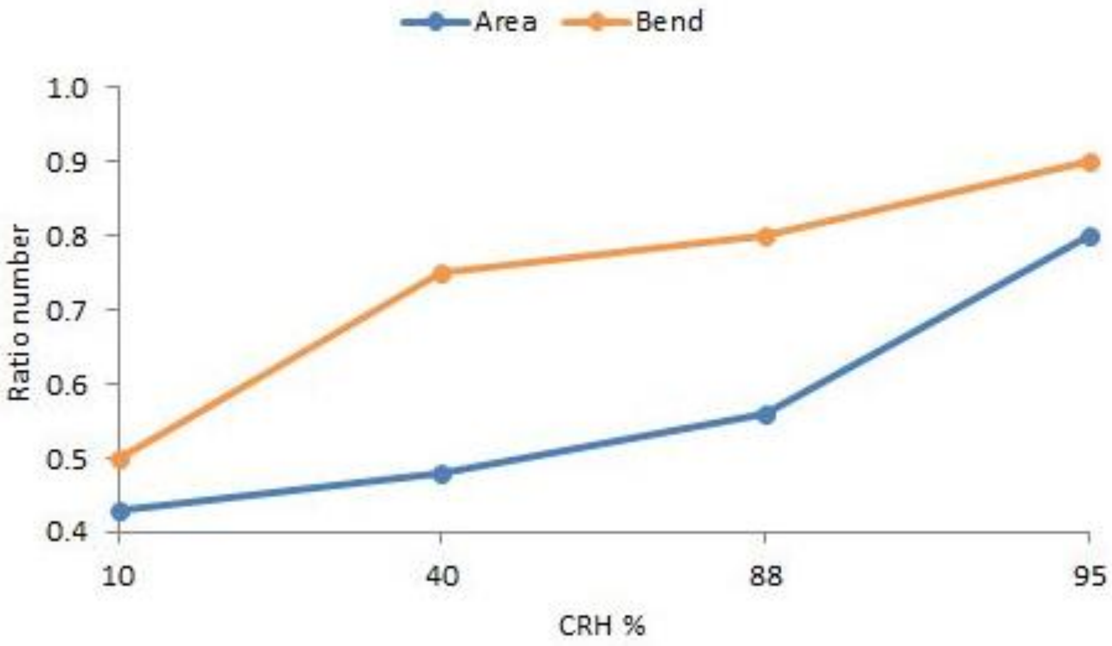

Figure 4.25: The wetted area and bend ratio numbers for the cathode side.

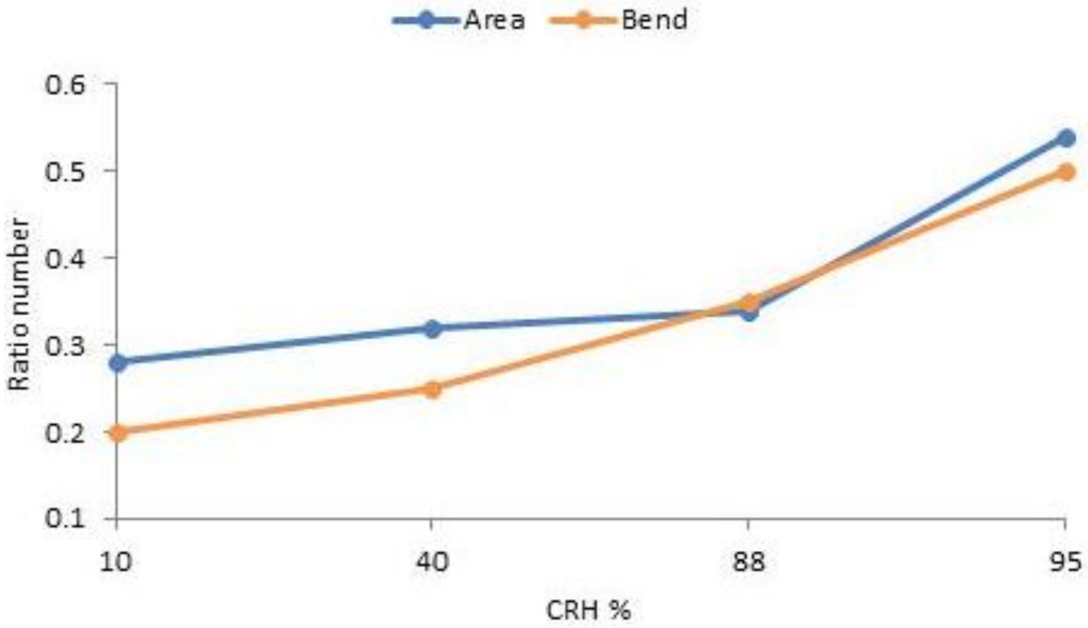

Figure 4.26: The wetted area and bend ratio numbers for the anode side.

Fig. 4.27 and 4.28 show the polarization and potentiostatic curves for the cases in which the relative humidity of hydrogen has been varied to investigate its effect. One can clearly see that the fuel cell performance for all the investigated cases is relatively low. This could be attributed to the use of dry air. Also, it can be observed that the fuel cell performance increases as the hydrogen relative humidity increases, leading to better membrane hydration and enhanced ionic conductivity. Notably, the potentiostatic curves of the cases, at 0.70 V, are highly erratic. This is apparently due to the high dynamics of liquid water at the anode side which has been confirmed through the corresponding recordings. However, towards the end of the timeline, the order of the cases in terms of the current density has been found to be in line with that of the polarization curve at 0.70 V.

Fig. 4.31 and 4.32 show the wetted ratio numbers calculated for the cathode and anode flow channels at 0.70 V for the cases in which the hydrogen relative humidity has been changed from 10 to 100%. These ratio numbers were calculated based on the captured images for both sides, see Fig. 4.29 and Fig. 4.30. As expected, the wetted ratio numbers increase as the relative humidity of hydrogen increase.

As with the previous investigation, the similarity of the trends of the wetted ratio numbers at both the cathode and the anode indicates that these numbers at the anode side can also be used to interpret the relationship between the fuel cell performance and the relative humidity of the inlet gases.

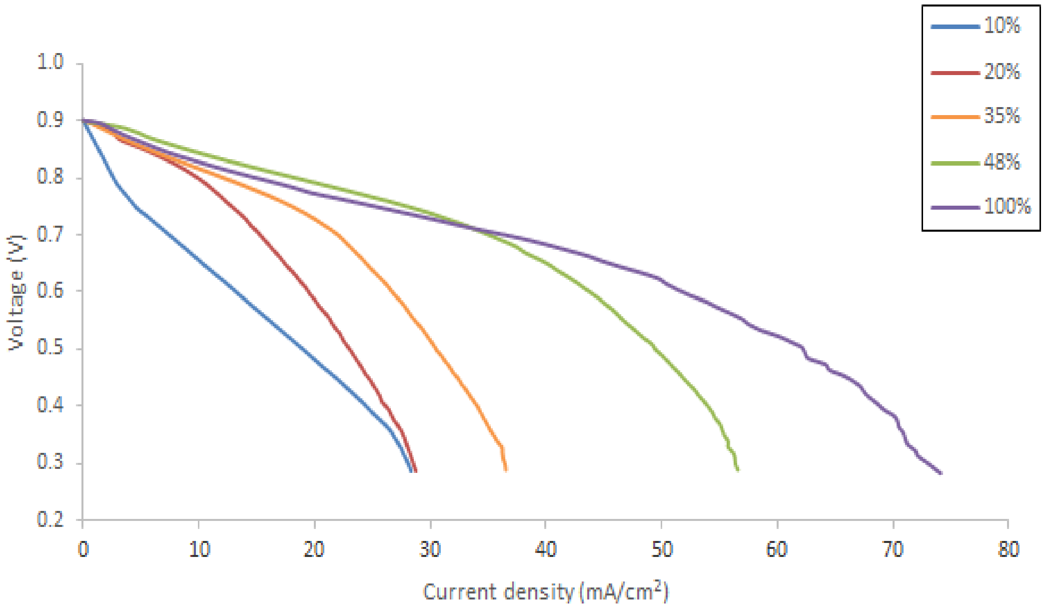

Figure 4.27: The polarization curves for all the investigated hydrogen relative humidity.

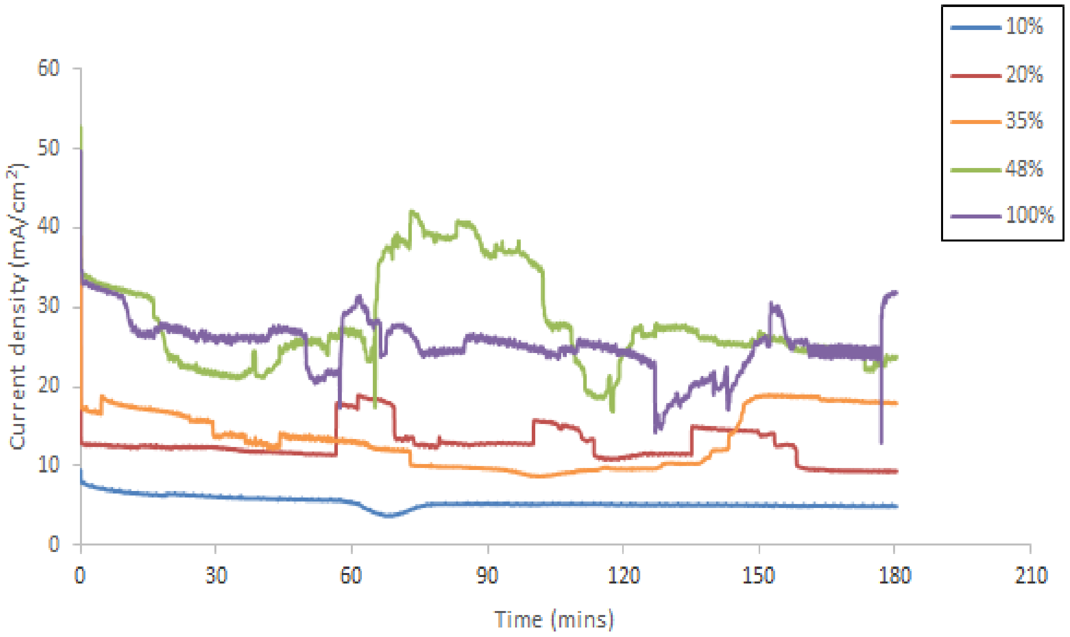

Figure 4.28: The measured current density at 0.70 V as a function of time for all the investigated hydrogen relative humidity.

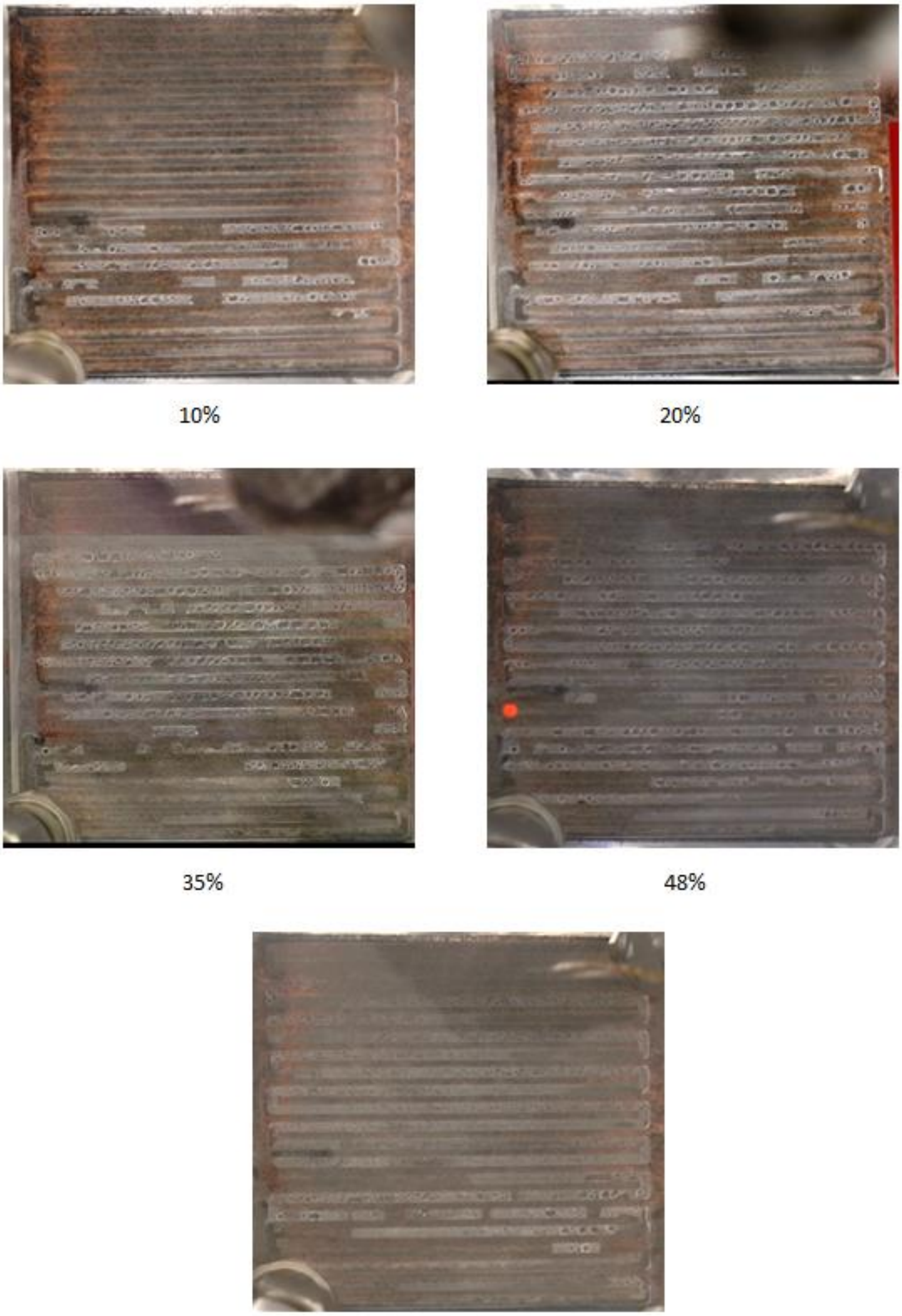

10%

20%

35%

48%

100%

Figure 4.29: The captured images at the cathode side for all the investigated hydrogen relative humidity.

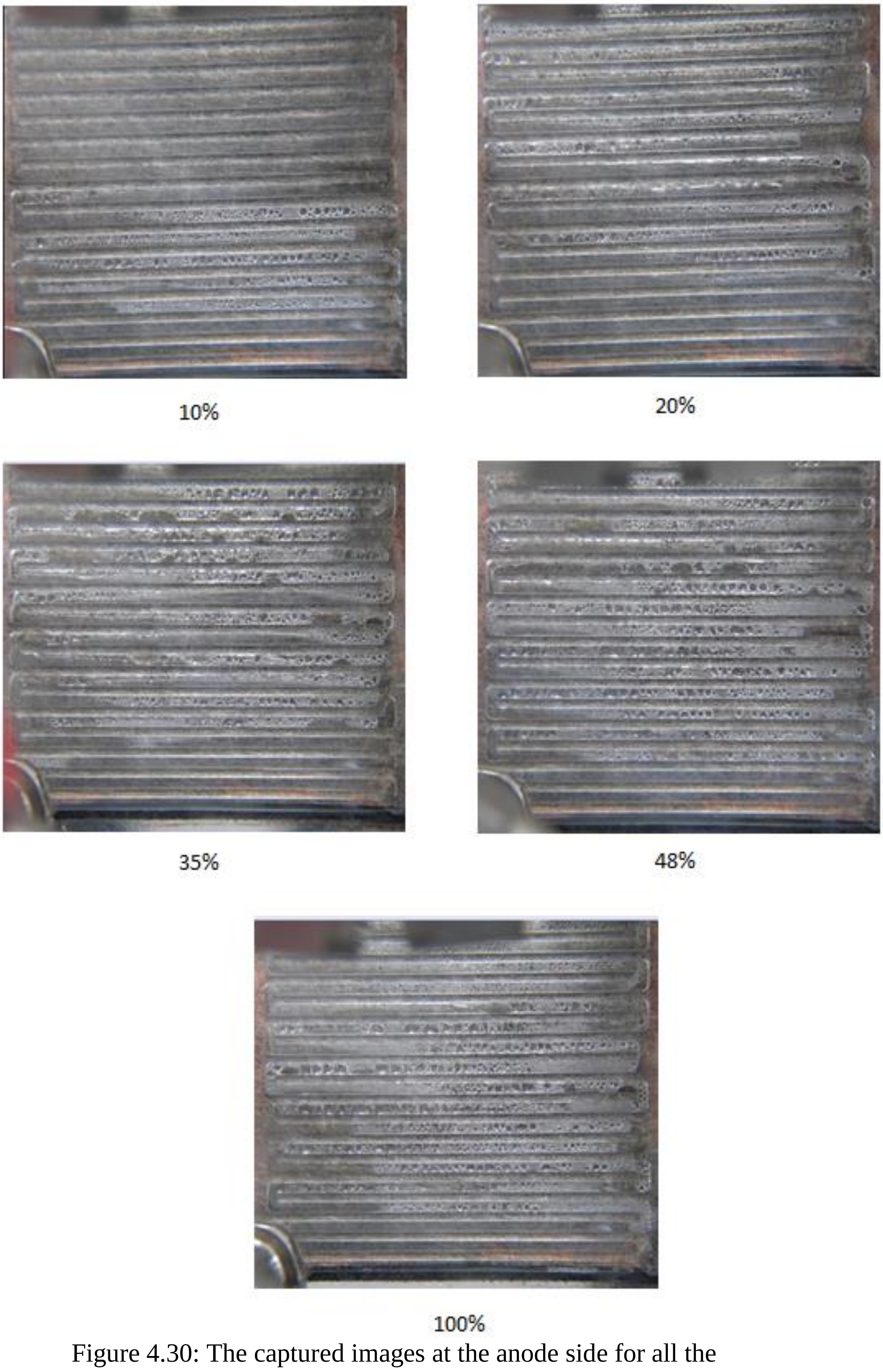

10%

20%

35%

48%

100%

Figure 4.30: The captured images at the anode side for all the investigated hydrogen relative humidity.

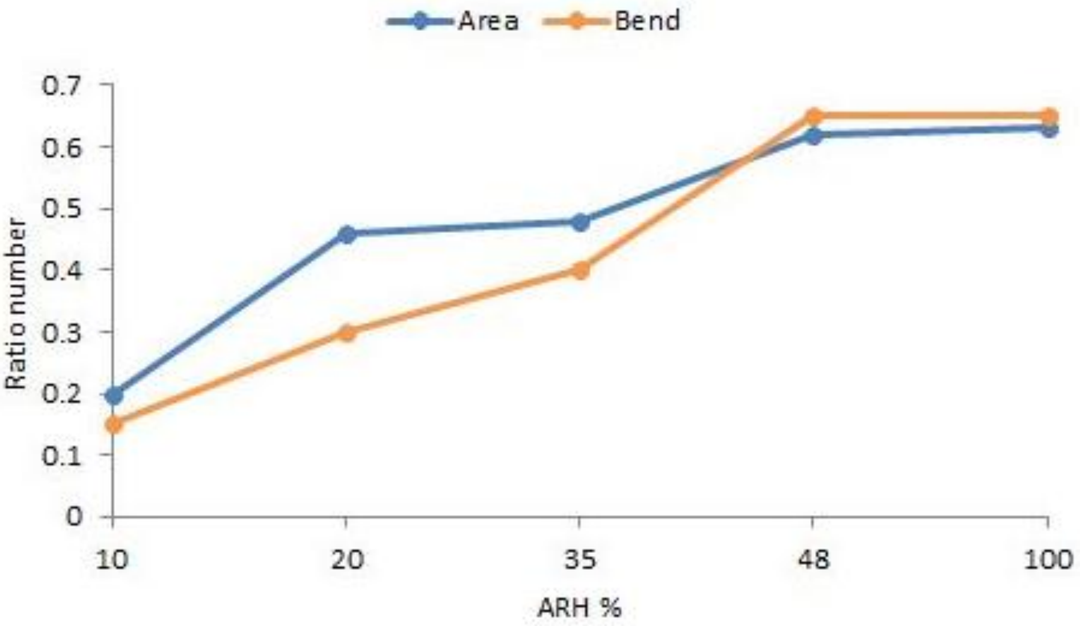

Figure 4.31: The wetted area and bend ratio numbers for the cathode side.

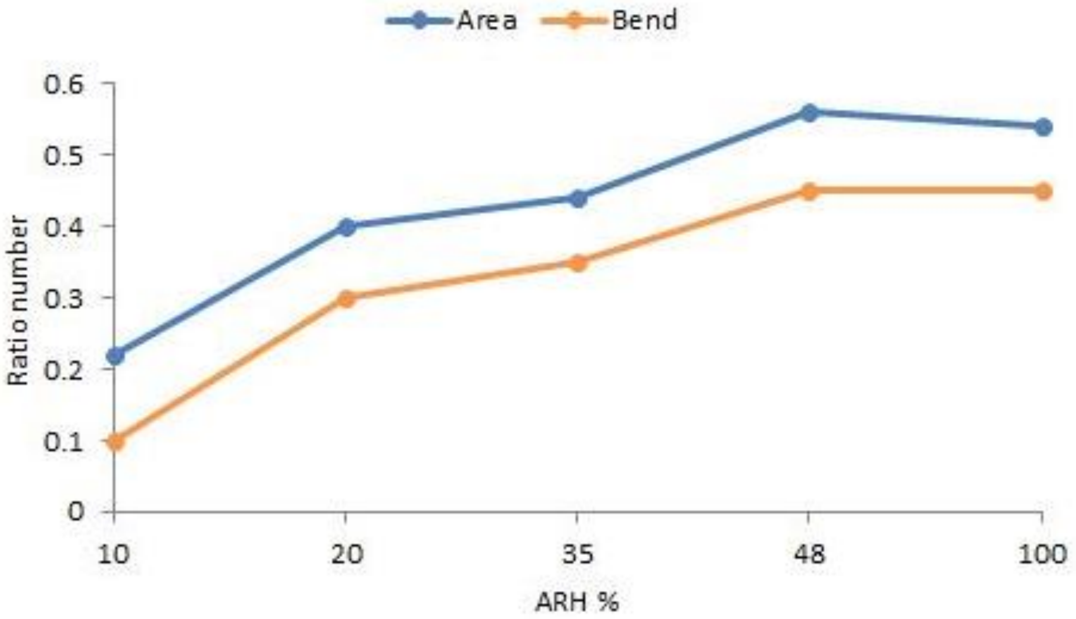

Figure 4.32: The wetted area and bend ratio numbers for the anode side.

4.6 CHAPTER SUMMARY

In this chapter, a direct visualization of the flow channels at both the cathode and anode of a transparent PEM fuel cell has been performed simultaneously. A new parameter, wetted bend ratio, which gives an indication of how the bends of the serpentine flow channels are flooded, has been introduced. It has been used to elucidate the variation in the fuel cell performance as a number of operating conditions (i.e. the flow rates, the operating pressure and the relative humidity) are changed. The following are the main findings:

- There is an existence of optimum values for the air and hydrogen flow rates. These values form the trade-off between the positive effect of purging the liquid water from the flow channel and the negative effect of the membrane dry-out.
- As the operating pressure increases, the fuel cell performance and the wetted bend ratio increase.
- There is an existence of optimum value for the air relative humidity which is the trade-off between the positive effect of membrane hydration and negative effect of water flooding. On the other hand, the fuel cell performance was found to increase with increasing hydrogen relative humidity. As expected, the wetted bend ratio was found to increase as the relative humidity of either air or hydrogen increases.

- In most of the investigations, it has been shown that the trends of the wetted ratio numbers for both the cathode and anode have been similar. This implies that the anode side, where there is no water production, can also be used to explain the relationship between the fuel cell performance and the operating conditions.

CHAPTER 5

VISUALIZATION OF THE LIQUID WATER AND TEMPERATURE DISTRIBUTION SIMULTANEOUSLY

In chapter 5, the PEM fuel cell has been operated to investigate the effect of gas flow rates on the liquid water and temperature distribution. The status (i.e. vapour or liquid) and amount of water is highly affected by temperature as saturation pressure, which is used to determine saturation of water, is a strong function of temperature. The sources of heat in PEM fuel cells are (i) entropic (ii) irreversible due to the voltage losses (i.e. activation, ohmic and concentration losses) and (iii) due to phase change through condensation/evaporation [71], [94] and [95]. Due to the strong relation between the amount and status of water and temperature, the simultaneous investigation of the distribution of liquid water and temperature will be of great benefit and interest to the designers and modellers of PEM fuel cell. Namely, such investigations will assist in obtaining better understanding on how liquid water is correlated to the distribution of temperature within the fuel cell. Eventually, this will provide insights on how liquid water and temperature could be both managed to prevent undesirable phenomena of water flooding and membrane dehydration. As discussed earlier in Chapter 3, Section 3.3, the modification of the transparent PEM fuel cell has been performed which involved thinning the plate. This is due to the material characteristic of PMMA which is entirely opaque to infra-red transmission. Thus, in this experiment, the temperature measurement captured by the thermal camera is outside temperature of the plastic plate. However, it should be noted that the MEA, where the heat is generated, is adjacent to the transparent plate.

Hence, the thinning of the transparent plate process is performed in order to reduce the thermal resistance between the side of the MEA facing the internal surface of the transparent plate and the outside surface of the transparent plate. Therefore, it is expected for the distribution of the external temperature to be similar, but slightly less due to thermal resistance of the transparent plate, to that of the MEA.

5.1 EXPERIMENTAL TEST SETUP

All the visualization experiments were carried out using the same commercial transparent PEM fuel cell, CPK202 ClearPak (Pragma Industries) in Chapter 4. As the authors were more interested in PEM fuel cells powering small portable devices and featuring no active heating means, the fuel cell was not heated; therefore, its temperature was, in general, slightly higher than room temperature, e.g. 22-24°C.

5.2 VISUAL AND THERMAL IMAGING

The distribution of temperature at the cathode side and the liquid water at both the cathode and the anode sides have been simultaneously recorded using thermal and digital cameras; see Fig. 3.9 in Section 3.3. As mentioned in the introduction, a parameter extracted from the captured images of the flow channels, the wetted bend ratio, has been employed as an indicator of the amount of liquid water present in the flow channels [157]. This parameter, along with the wetted bend ratio [163], will be used to explain the performance and thermal variations of the fuel cell. The wetted bend ratio and wetted area ratio are calculated similarly as explained in Chapter 4; see Fig. 4.2 in section 4.2. For simplicity, we consider the bend to be wet when it is occupied by liquid water.

5.3 EFFECTS OF THE GAS FLOW RATE

The air flow rate has been changed to investigate its effect on the distributions of the liquid water and temperature in the modified PEM fuel cell as mentioned in Section 3.4. The set of flow rates used were 0.10, 0.15, 0.20 and 0.25 Standard Litre per Minute (SLPM), which corresponds to stoichiometry ratios of 2, 3, 4 and 5, respectively. The hydrogen flow rate has been kept constant at 0.05 SLPM, which is the theoretical hydrogen flow rate calculated based on a total current of 8 A and stoichiometry ratio of about 1.5. During the experiment, the operating pressure was kept constant: 1 barg. A humidity sensor (Hyroflex Rotonic, Switzerland) has recorded the relative humidity of the gases entering the fuel cell at both sides as 80% and the polarization and potentiostatic results have been recorded for each air flow rate. As described in the previous section, the visual imaging of the liquid water and thermal imaging have been performed simultaneously.

Fig. 5.1 shows the polarization curves for the corresponding cases in which the air flow rate has been changed between 0.10 and 0.25 SLPM. It can be seen that the fuel cell performance, in general, slightly decreases as the air flow rate increases from 0.10 to 0.25 SLPM and this is most likely due to the decrease in the level of the humidification of the membrane with increasing flow rate. As it can be inferred from the captured images shown in Fig. 5.3 and Fig. 5.4, the level of water available at the flow channels decreases as the air flow rate increases, thus potentially decreasing the amount of liquid water required for adequate humidification of the membrane. Also, it should be noted when compared to the results presented that in a previous work [163], the fuel cell performance is low. This could be attributed to the poor contact between the MEA and the current collectors of the fuel cell resulting from the thinning of the transparent plates. One of the possible ways to resolve this problem is to use substantially stiffer transparent plates than used in the current investigation.

To investigate the status of the liquid water in the flow channels, the potentiostatic curves were generated at 0.60 V, see Fig. 5.2. As with the corresponding polarization curves, it can be seen that, after reaching almost the 'pseudo' steady-state condition, the best fuel cell performance is when the air flow rate is 0.10 SLPM and it decreases as the air flow rate increases.

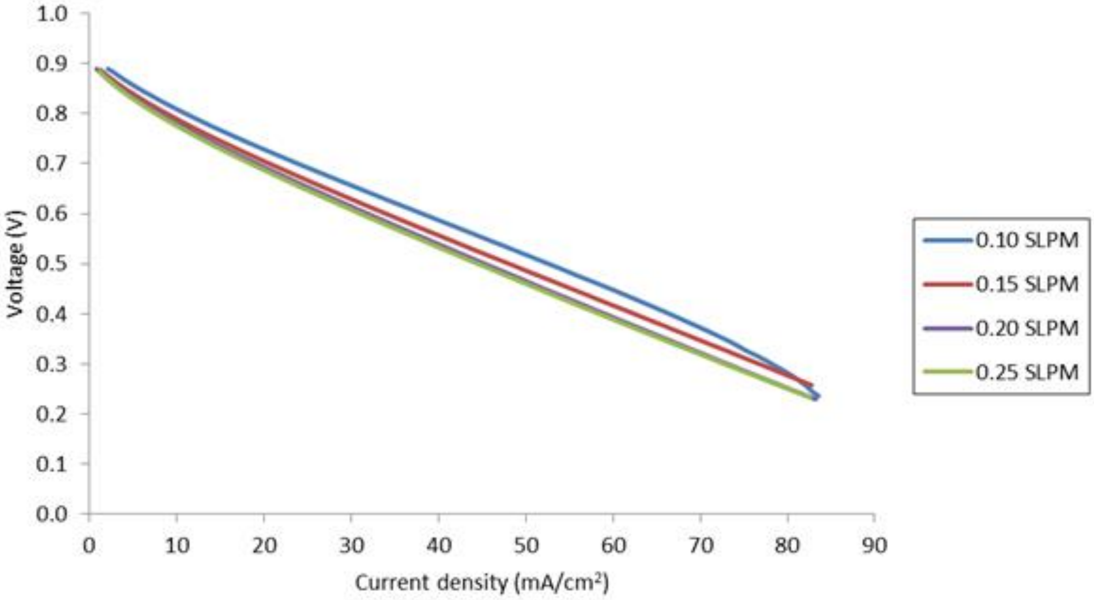

Figure 5.1: The polarization curves for all the investigated air flow rates.

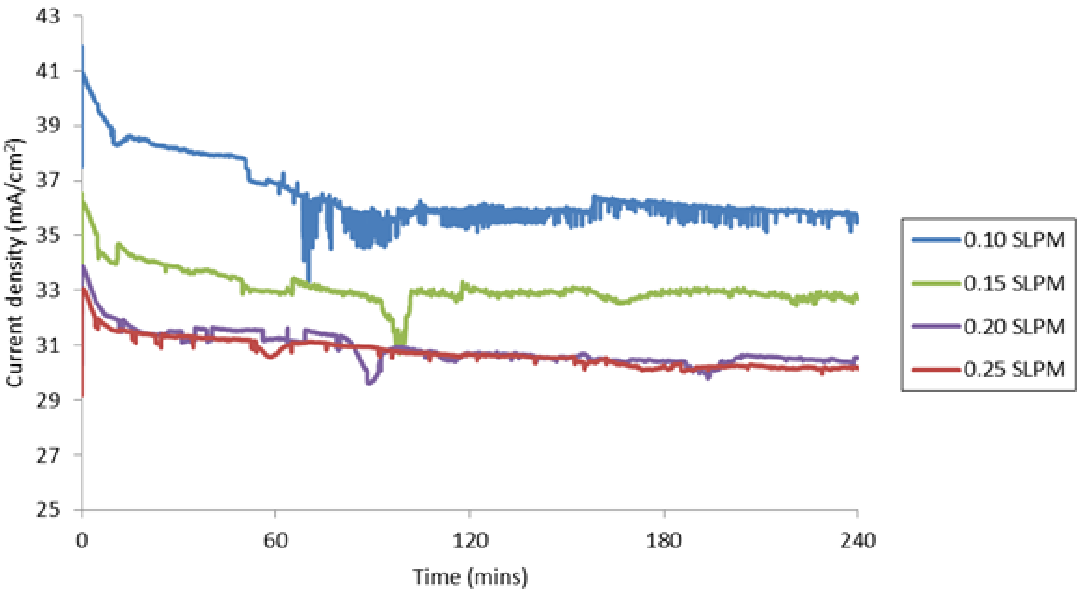

Figure 5.2: The measured current density at 0.60 V as a function of time for all the investigated air flow rates.

The wetted bend ratio and wetted area ratio for both sides of the fuel cell have been calculated from the captured images, see Fig. 5.3 and Fig. 5.4 and are plotted in Fig. 5.5. It can be seen that both ratios decrease as the air flow rate increases and this is most likely due to the increase in the ability to remove liquid water from the flow channel with an increasing air flow rate. The wetted ratio numbers at the cathode are larger than those of the anode and this is most likely because the hydrogen flow rate has been kept constant and the curves of the wetted ratios at the anode side are similar to those at the cathode side. This could be attributed to the back diffusion of liquid water from the cathode side to the anode side that apparently decreases with increasing air flow rate. This signifies that the wetted ratio numbers at the anode side can also be used to interpret the relationship between the fuel cell performance and the air flow rate.

Fig. 5.6 shows the thermal images at the cathode side of the fuel cell as the air flow rate increase from 0.10 to 0.25 SLPM. The gas inlet is at the upper right corner of the thermal image and the gas outlet is at the lower left corner. As it can be seen from the images, the uniformity in the temperature distribution decreases as the air flow rate increases. Specifically, a ‘hot-spot’ at the downstream of the flow channel near the cathode outlet starts to form and become larger and ‘stronger’ as the air flow rate increases. This is most likely due to the observation that the amount of liquid water present in the flow channels is the highest and the most uniformed with the 0.10 SLPM flow; see Fig. 5.3 and Fig. 5.4. The thermal conductivity of the liquid water is one order of magnitude higher than that of air [16]. To this end, the higher the amount of liquid water present at the cathode, more heat is conducted to the transparent plate and, subsequently, more uniformed is the temperature distribution recorded by the thermal camera.

0.10 SLPM 0.15 SLPM

0.20 SLPM 0.25 SLPM

Figure 5.3: The images taken for the cathode side at 0.60 V for the cases at which the air flow rate has been changed incrementally from 0.10 to 0.25 SLPM.

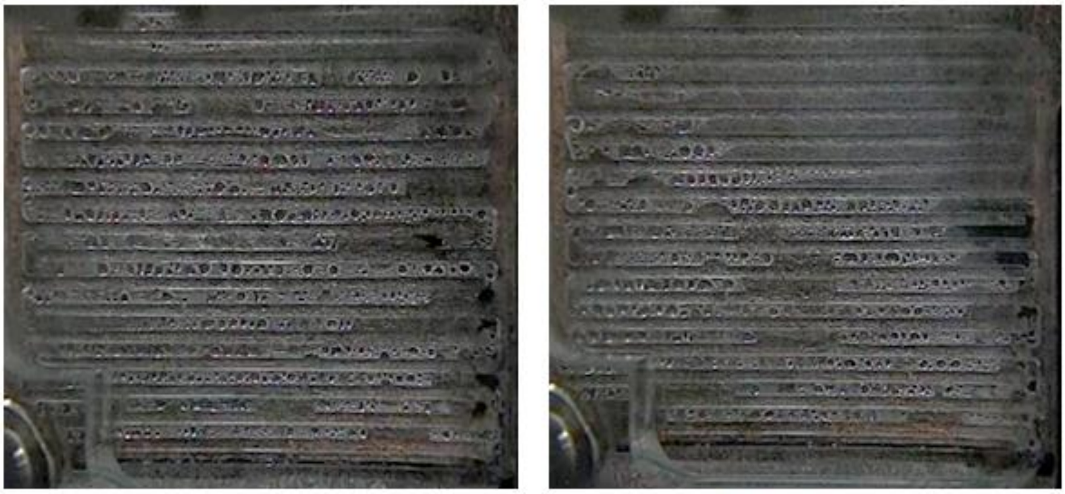

0.10 SLPM

0.15 SLPM

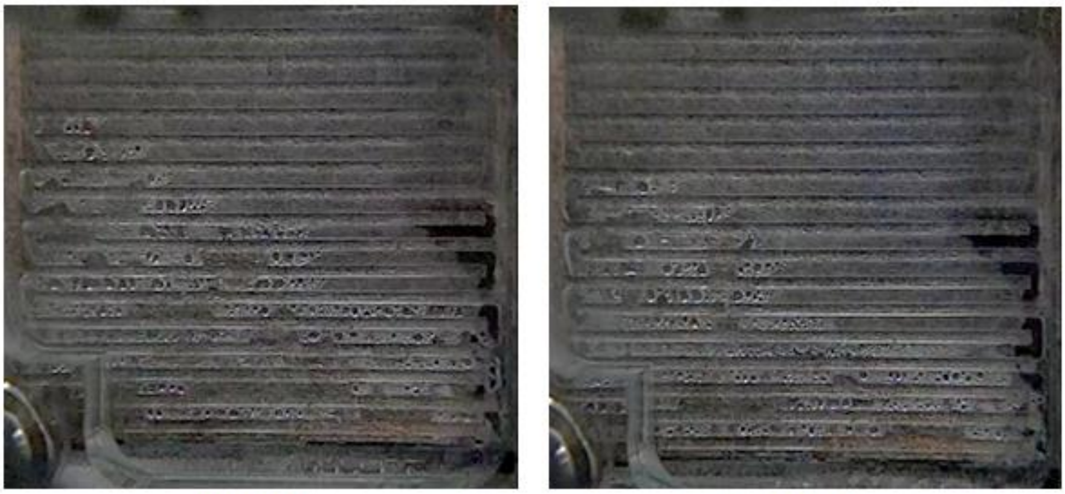

0.20 SLPM

0.25 SLPM

Figure 5.4: The image taken for the anode side at 0.60V for the cases at which the air flow rate has been changed incrementally from 0.10 to 0.25 SLPM.

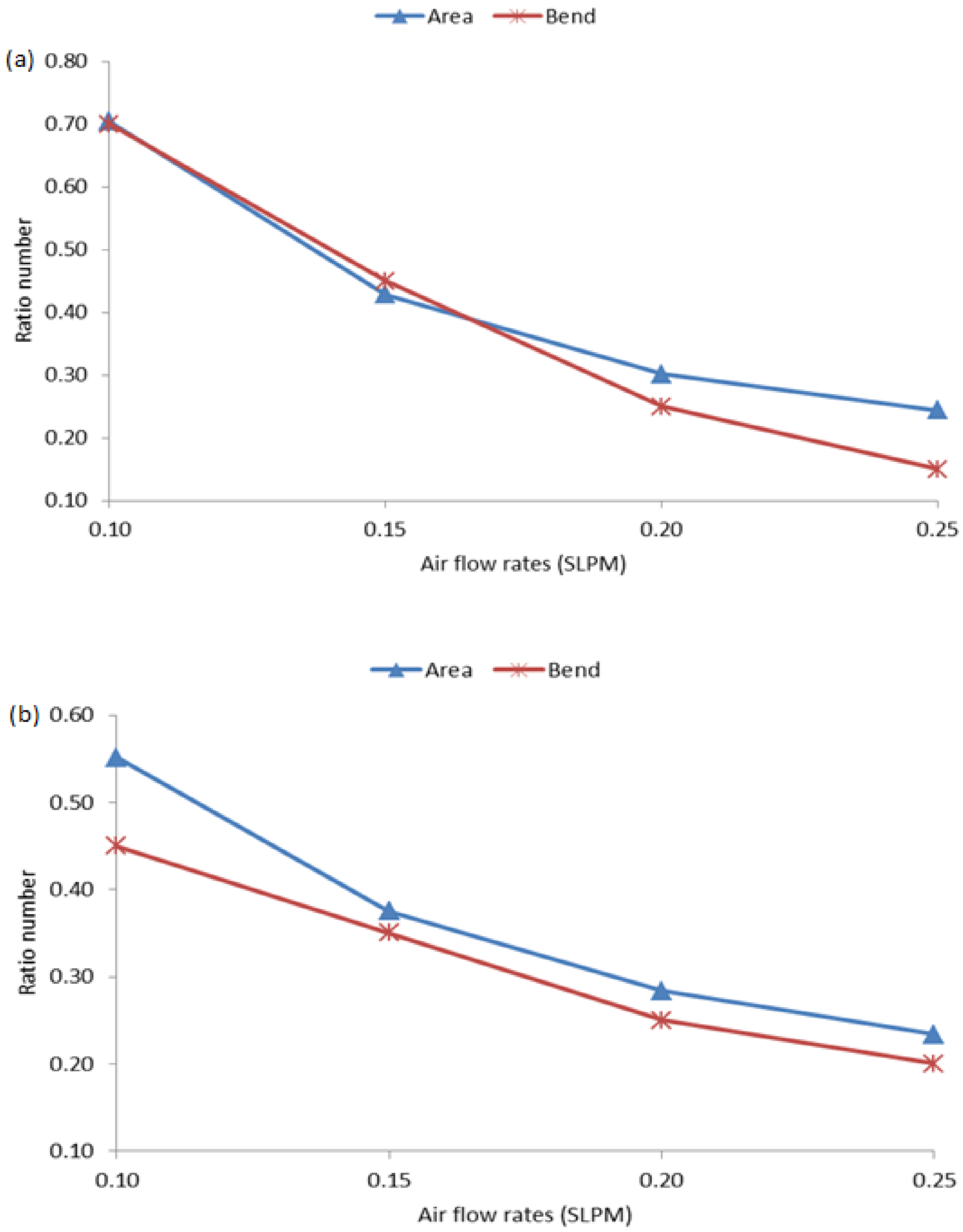

Figure 5.5: The wetted area and bend ratio numbers at 0.6 V for the (a) cathode and (b) anode sides.

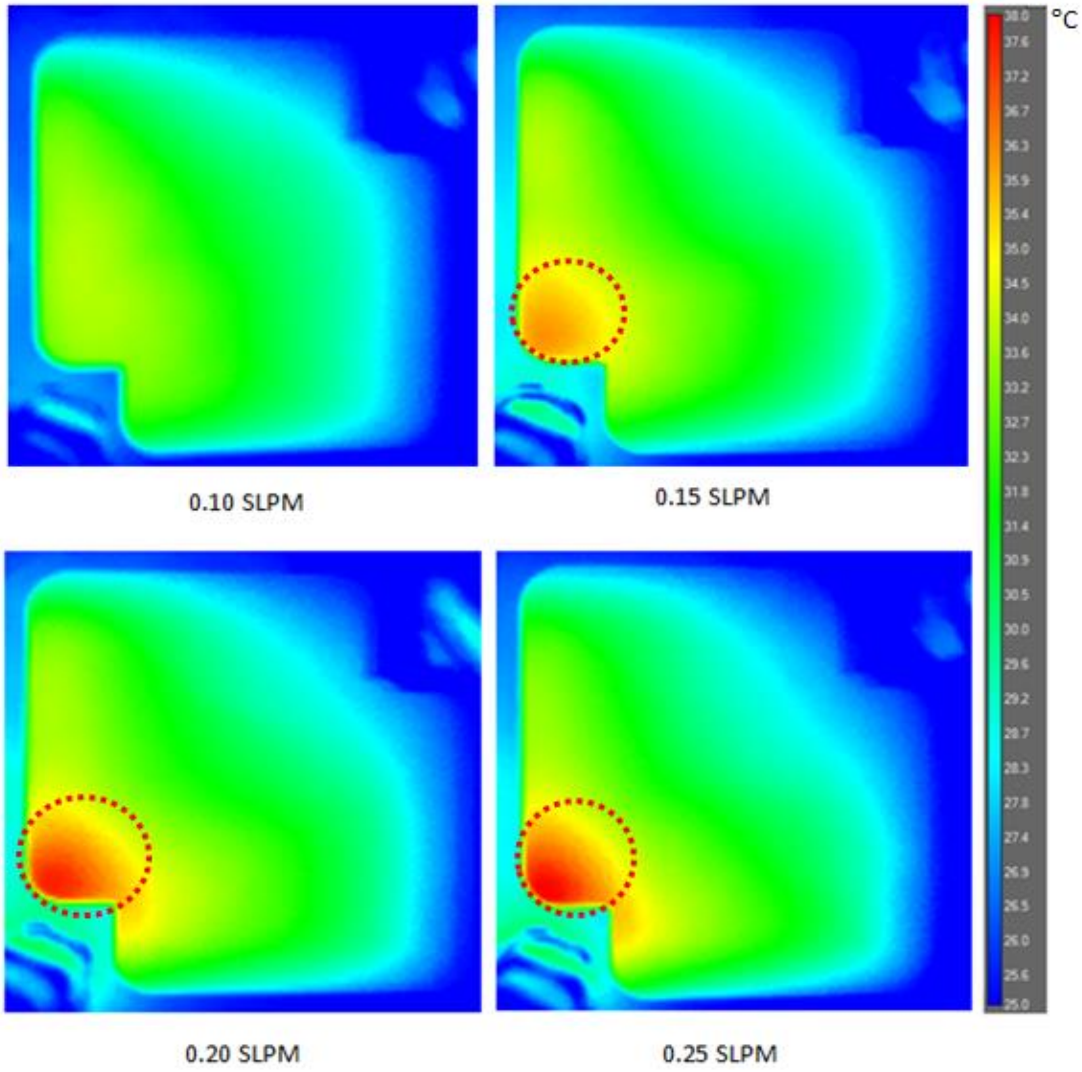

0.10 SLPM

0.15 SLPM

0.20 SLPM

0.25 SLPM

Figure 5.6: The thermal images taken for the cathode side at 0.6 V for the investigated cases in which the air flow rate has been changed incrementally from 0.10 to 0.25 SLPM.

5.4 CHAPTER SUMMARY

In this chapter, a transparent PEM fuel cell has been simultaneously visually and thermally imaged using high-resolution digital and thermal camera in order to explore the relation between the distributions of both liquid water and temperature. The focus has been at the cathode side as it is the side at which water is produced. To investigate the viability of the proposed experimental procedure, a parametric study, in which the air flow rate has been incrementally changed, has been conducted. The following are the main observations and/or findings:

- The temperature distribution along the MEA at the cathode side becomes more non-uniformed as air flow rate increases. This could be attributed to the observation that the liquid water (which has significantly larger thermal conductivity than air) in the cathode flow channels becomes less as the air flow rate increases, thus resulting in less efficient heat dissipation.
- The above findings could be alternatively expressed more quantitatively: the temperature distribution across the MEA becomes less uniformed as the wetted ratio number decreases.
- For the given in-house modified transparent fuel cell, the fuel cell performance decreases as the air flow rate increases. This was attributed to the increases in the rate of water removal from the cathode with increasing air flow rate, leading to the availability of less water to adequately humidify the membrane electrolyte.

CHAPTER 6

THE EFFECT OF HEAT TREATMENT ON THE THROUGH-PLANE GAS PERMEABILITY OF THE GAS DIFFUSION MEDIA

In this chapter, the through-plane gas permeability of the GDLs samples after heat treatment at different temperatures has been investigated. Three type of GDL samples namely, two different SGL samples (10CA and 10BC) and one Toray sample (TGP-H-060) have been chosen as the materials tested in the investigation. These types of GDLs are chosen to have further insight on the difference of coated and uncoated sample (SGL 10CA and SGL 10BC) and different manufacturer of GDL sample (SGL and Toray) have on the gas permeability after heat treatment process. Two manufacturers, namely SGL Technologies GmbH, Meitingen, Germany and Fuel Cell Earth, USA provided the samples.

6.1 EXPERIMENTAL TEST SETUP

There are three main pieces of equipment involved in this investigation namely, the tube furnace for heat treatment process, the in-house gas permeability setup for the measurement process and finally the SEM for image processing. All of this equipments has been described in Section 3.4 in Chapter 3. The experimental procedures are as follows:

I. Sample preparation. (6 samples for each type of GDL)
II. Gas permeability measurement before heat treatment process for each type of GDL.
III. Heat treatment at 200 °C, 500 °C and 800 °C for an hour.
IV. Gas permeability measurement after heat treatment at each temperature.
V. Image processing.

6.2 EFFECT OF HEAT TREATMENT

Three sets of experiment were carried out to study the effect of heat treatment process on the through-plane gas permeability of the GDL samples. In order to obtain further understanding on the factors that affect the gas permeability of the GDL, it is vital to define the test cases in a well-constructed manner. Table 6.1 summarises of all the samples tested and the parameters studied in the investigation.

Table 6.1: Samples tested in the gas permeability investigation.

Sample Material	**PTFE Loading (wt.%)**	**MPL Coating**	**Parameter Investigated**
SGL 10CA	10	No	Effect of MPL
SGL 10BC	20-25	Yes	Effect of MPL
Toray 060	5	No	Different manufacturer

Table 6.2 records the experimental data of the through-plane gas permeability for each GDL samples at different heat treatment temperatures while Figure 6.1, 6.2

and 6.3 shows the plotted graph of the experimental data for SGL 10CA, SGL 10BC and Toray 060, respectively. Notably, the values of the gas permeability are the average of six samples of each sample material, and the error bars shown in Fig. 6.1 to 6.5 represent plus or minus one standard deviation based on these measurements.

Table 6.2: The through-plane gas permeability of GDL materials at different heat treatment temperatures.

Sample Material	**Through-plane gas permeability (m^2)**			
	RT	**200 °C**	**500 °C**	**800 °C**
SGL 10CA	2.34×10^{-11}	2.35×10^{-11}	2.41×10^{-11}	2.51×10^{-11}
SGL 10BC	4.87×10^{-13}	4.86×10^{-13}	4.96×10^{-13}	3.76×10^{-13}
Toray 060	7.19×10^{-12}	7.18×10^{-12}	7.37×10^{-12}	7.39×10^{-12}

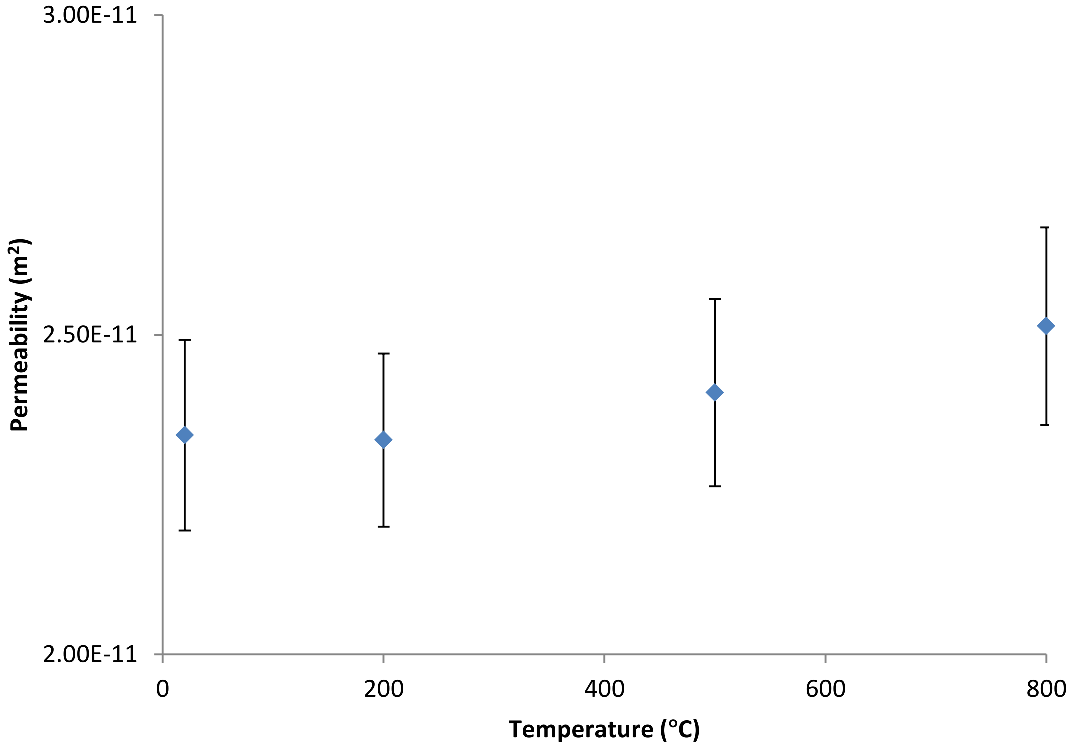

Figure 6.1: Through-plane gas permeability of the SGL 10CA as a function of heat-treatment temperature.

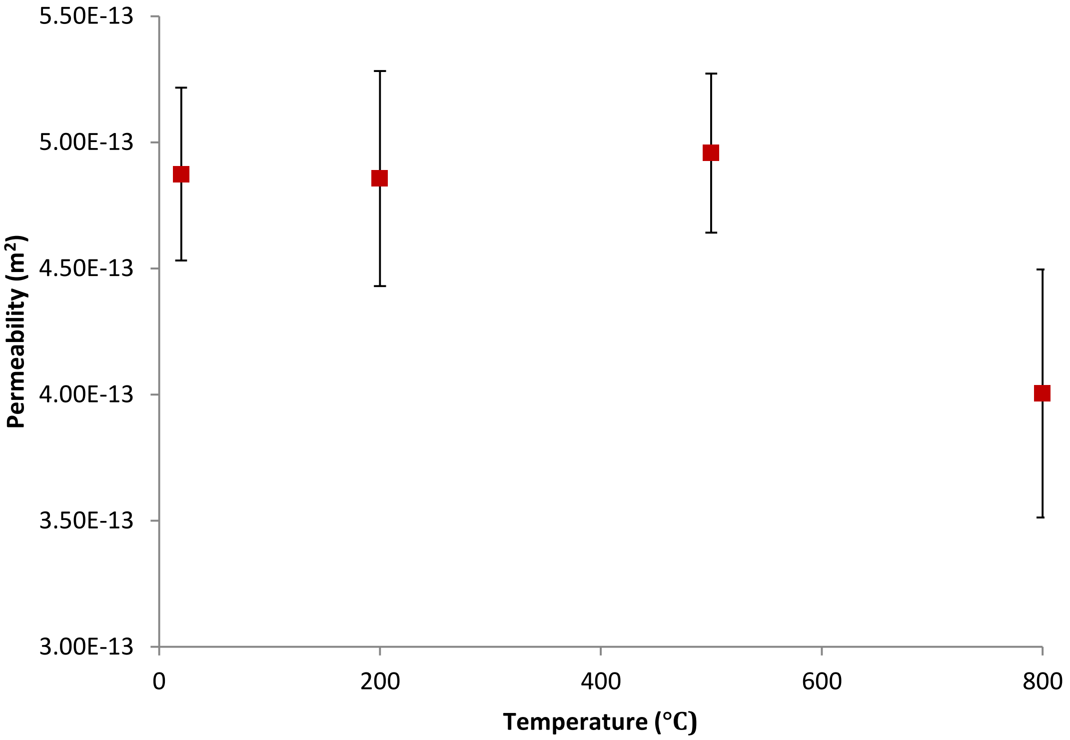

Figure 6.2: Through-plane gas permeability of the SGL 10BC as a function of heat-treatment temperature.

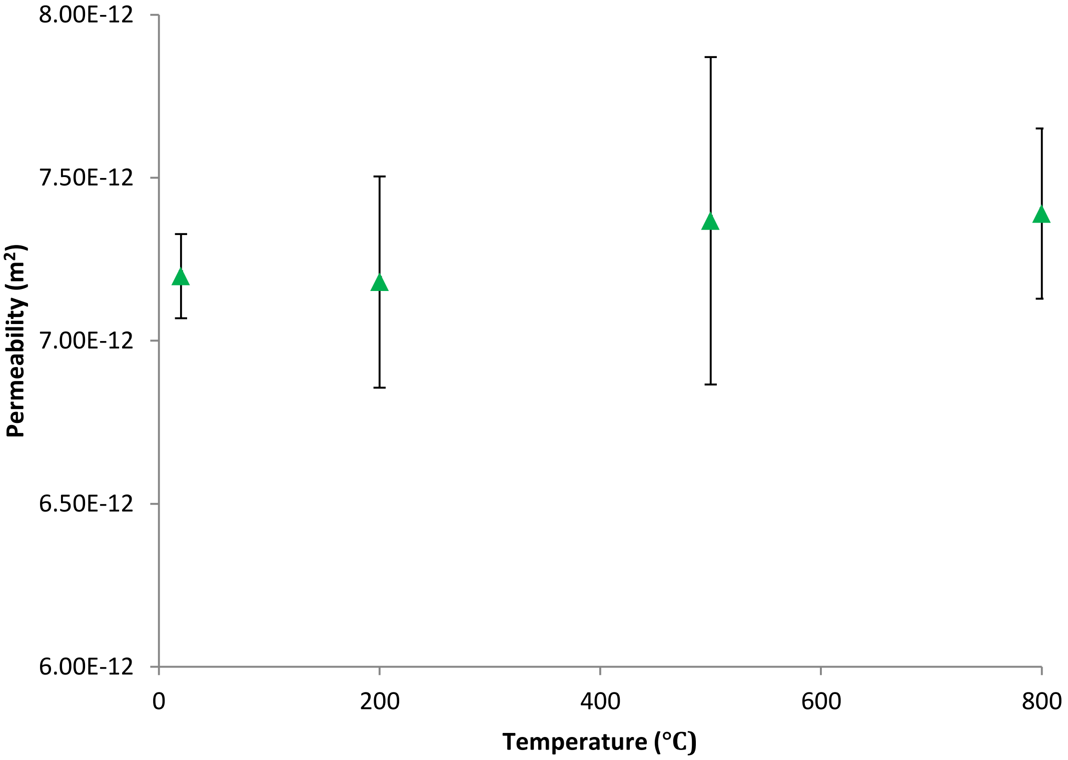

Figure 6.3: Through-plane gas permeability of the Toray 060 as a function of the heat-treatment temperature.

Generally, the through-plane gas permeability for all types of GDL samples increases as the heat treatment temperature increases. However, for SGL 10BC, the increment of the gas permeability occurs from room temperature to 500 °C and this is not the case when heat-treated at 800 °C. In addition, there is an insignificant change shown in the gas permeability for all GDL samples from room temperature to 200 °C. This might be due to the unchanged surface morphology at that temperature where the melting point of the PTFE is at 327 °C [164]. Another graph plotted in Figure 6.4 to show the comparison of the through-plane gas permeability of all type of GDL samples after been heat-treated at higher temperatures. It can be seen that the through-plane gas permeability of SGL 10BC is relatively low compared to the other GDL samples as it has been coated with the MPL.

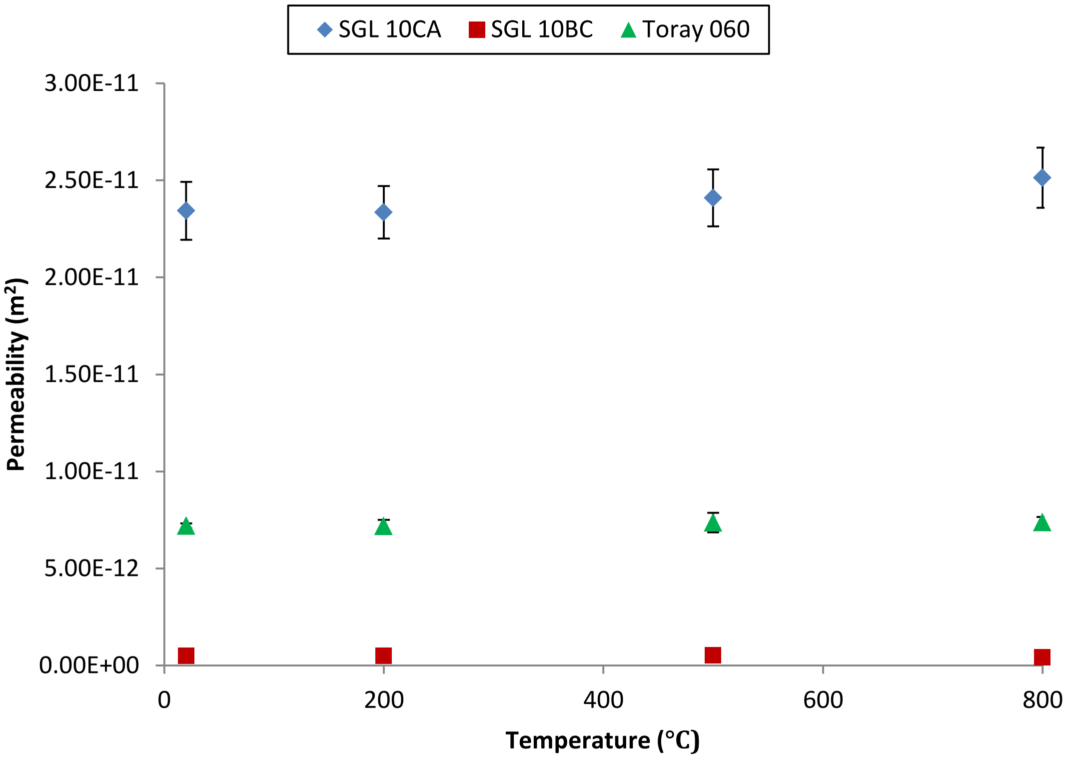

Figure 6.4: Through-plane gas permeability of all the GDL samples as a function of the heat-treatment temperature.

SGL 10BC shows the lowest through-plane gas permeability due to the introduction of a microporous layer to the GDL. The introduction of the microporous layer results to the fillings in gaps between adjacent carbon fibres, hence the surface porosity of the material reduces. Comparison of the obtained through-plane gas permeability of the SGL 10CA and SGL 10BC sample at room temperature, for example, with the previous researchers show good agreement. Ismail et al. [130] found that the through-plane gas permeability for SGL 10CA to be 2.22 x 10^{-11} m^2 and in another research [133], they measured the through-plane gas permeability for SGL 10BC to be 4.97 x 10^{-13} m^2.

Further investigation through image processing is performed to investigate the morphology changes of the GDL sample after going through the heat treatment process. All of the GDL samples were imaged through the SEM before and after heating at each temperature. Figures 6.6, 6.8 and 6.10 show the images of SGL 10CA, SGL 10BC and Toray 060 at lower magnification, which is 50 times, respectively. Meanwhile, Figures 6.7, 6.9 and 6.11 show the images of SGL 10CA, SGL 10BC and Toray 060 at higher magnification, which is 300 times, respectively. These magnifications were used to analyse the morphology changes of the GDL material as a whole and in depth.

As shown in Figures 6.6 and 6.7, the morphology changes of the SGL 10CA before and after heat treatment process is noticeable. However, only a few differences are shown especially at 500 °C and 800 °C for example, Figures 6.6(c) and (d) show the carbon fibres are less connected compare to Figures 6.6(a) and (b). This could be confirmed with the images in Figures 6.7(c) and (d) where it shows the carbon fibres at higher temperatures seems to be less intact compared to Figures 6.7(a) and (b). This may explained the increment in the through-plane gas permeability of SGL 10CA at 500 °C and 800 °C and negligible changes at 200 °C. Also, it could be explained due to the melting point of PTFE which is 327 °C as mentioned earlier [164]. As the PTFE content in SGL 10CA is 10% (wt. %), the high temperature which above its melting point have caused alterations and defects in the surface structure. This probably could also explained why the number of ‘bright’ material which is the PTFE [165] on the surface is reduced as the temperature increases.

Meanwhile, Figures 6.8 and 6.9 show the morphology changes of the SGL 10BC before and after heat treatment process clearly. It is visible from Figures 6.8 and 6.9 that the number and size of cracks on the surface of the sample increases as the temperature increases. As the PTFE content in the SGL 10BC is significant i.e. 20-25% (wt. %) and with the introduction of MPL which is held in a suspension of PTFE binder on the sample, it is expected that the high temperatures especially above 327 °C would cause noticeable surface changes and increase the through-plane gas permeability. However, it should be noted that the through-plane gas permeability for SGL 10BC decreases at 800 °C. It is quite challenging to explain and require further investigation i.e. further heating process beyond 800 °C to compare the trend. Hence, another experiment involving only SGL 10BC was performed. The sample has been heat-treated at room temperature, 200, 500, 800 and 1000 °C to obtain further insight on the through-plane gas permeability.

As shown in Figure 6.5, the through-plane gas permeability of SGL 10BC decreases as the temperature increases to 1000 °C. This reveals that there is a threshold value for the heat-treatment temperature of SGL 10BC, which in the range of 500-800 °C before the through-plane gas permeability starts to decreases. The SEM image of the SGL 10BC at 1000 °C was taken to investigate any morphology changes, see Figure 6.12 and 6.13. Notably, it appears from Figure 6.12 that the SGL 10BC surface as a whole at 1000 °C to be less porous compared to the lower temperatures. In addition, the sizes of the cracks are smaller as shown in Figure 6.13. This might be the reason why the through-plane gas permeability decreases at 1000 °C due to the porosity decreasing.

Table 6.3: The through-plane gas permeability of SGL 10BC at different heat treatment temperatures.

Sample Material	**Through-plane gas permeability (m^2)**				
	RT	**200 °C**	**500 °C**	**800 °C**	**1000 °C**
SGL 10BC	4.37×10^{-13}	4.41×10^{-13}	4.70×10^{-13}	3.07×10^{-13}	2.96×10^{-13}

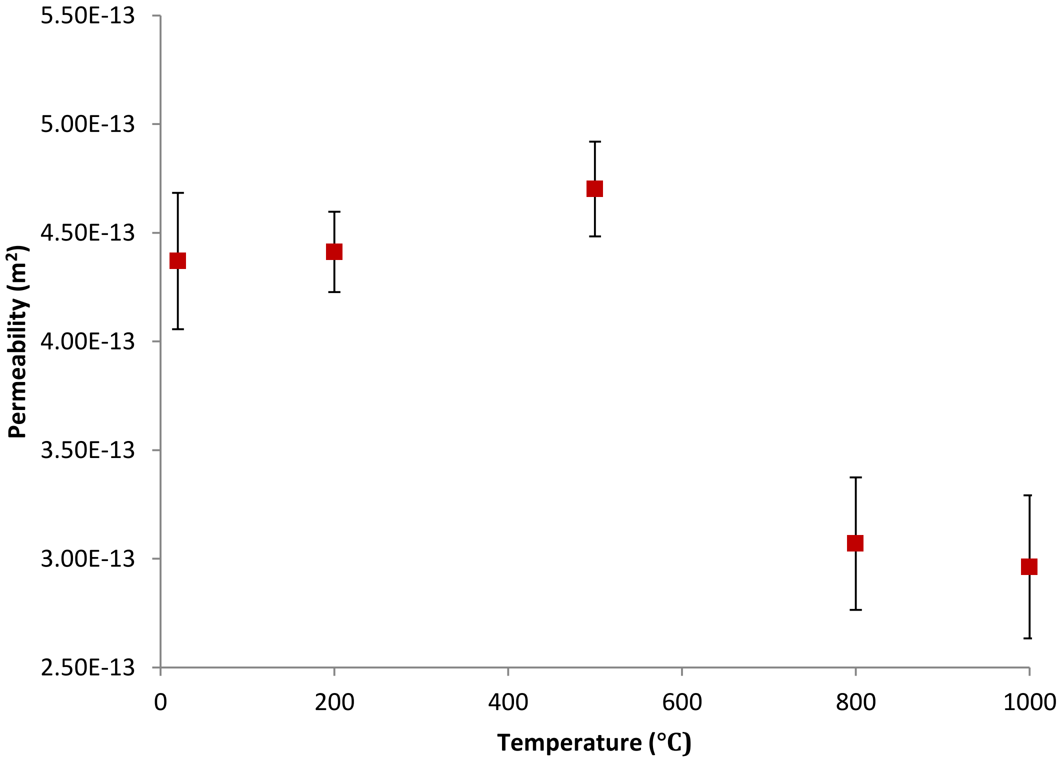

Figure 6.5: Through-plane gas permeability of the SGL 10BC as a function of heat-treatment temperature.

Figures 6.10 and 6.11 show the surface images of Toray 060. As PTFE content on Toray 060 is relatively low compared to the SGL 10CA and SGL 10BC, it is expected that the morphology changes are difficult to notice. In addition, the structure of Toray GDL is more uniform compared to SGL GDL. However, it is still noticeable that the ‘bright’ material i.e. PTFE, which tends to cluster at the intersection of carbon fibres, reduces in number as the temperature increases as shown in Figure 6.10. This could explain the increment of the through-plane gas permeability of Toray 060 as the temperature increases to 800 °C.

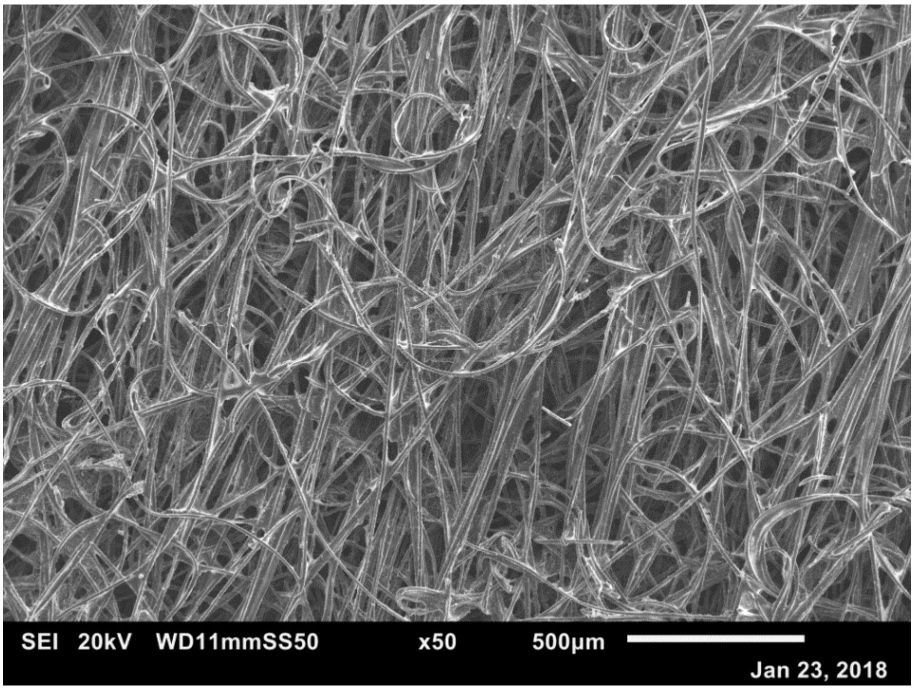
SEI 20kV WD11mmSS50 x50 500µm
Jan 23, 2018

(a)

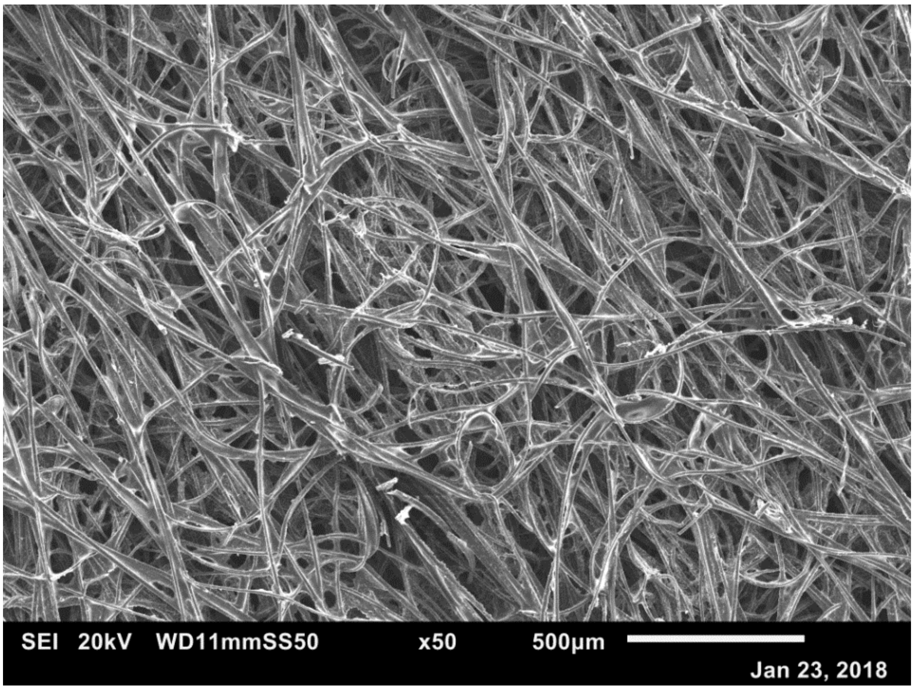
SEI 20kV WD11mmSS50 x50 500µm
Jan 23, 2018

(b)

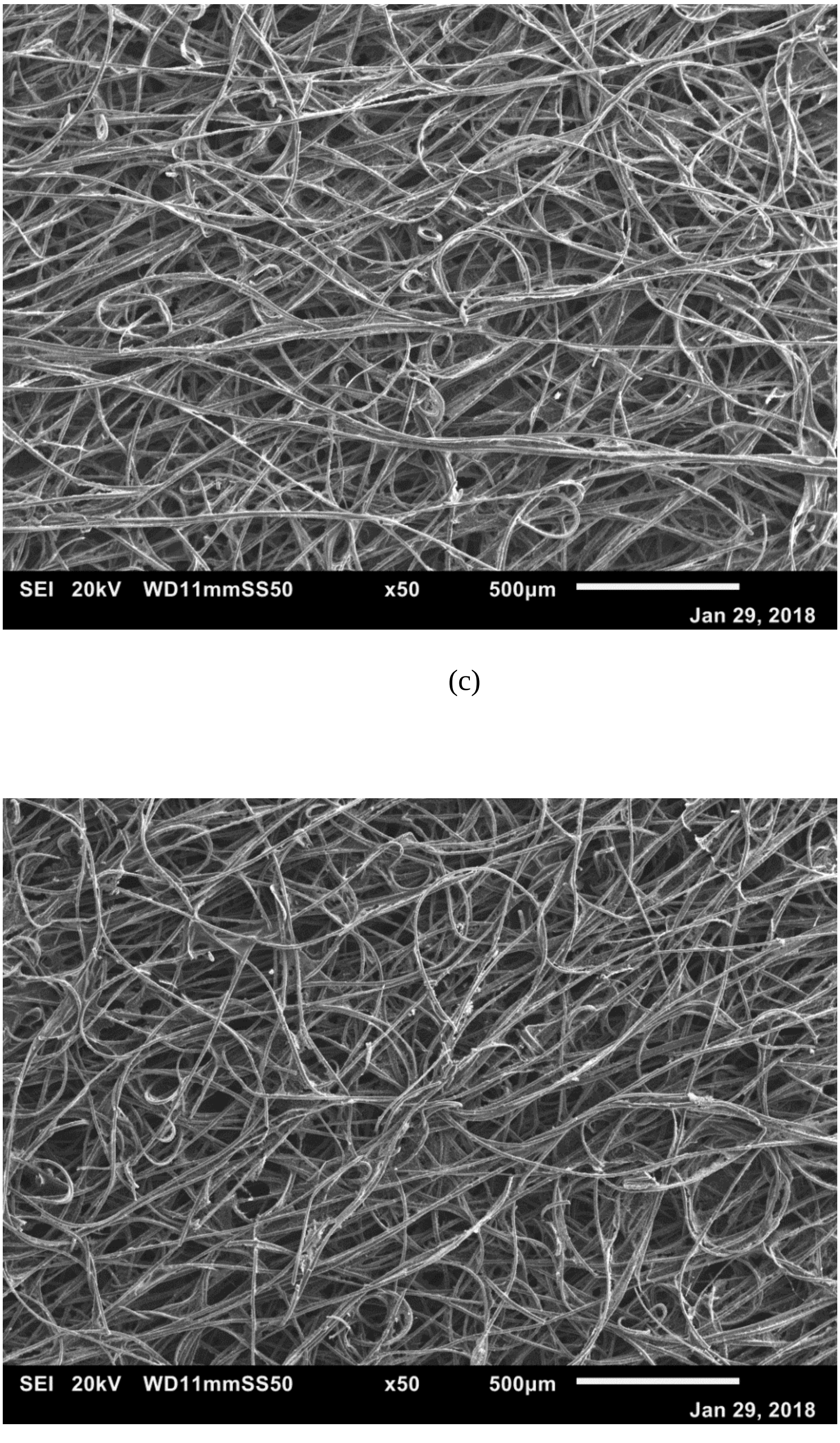

(c)

(d)

Figure 6.6: SEM images of SGL 10CA at 50x magnification (a) room temperature, (b) 200 °C, (c) 500 °C and (d) 800 °C.

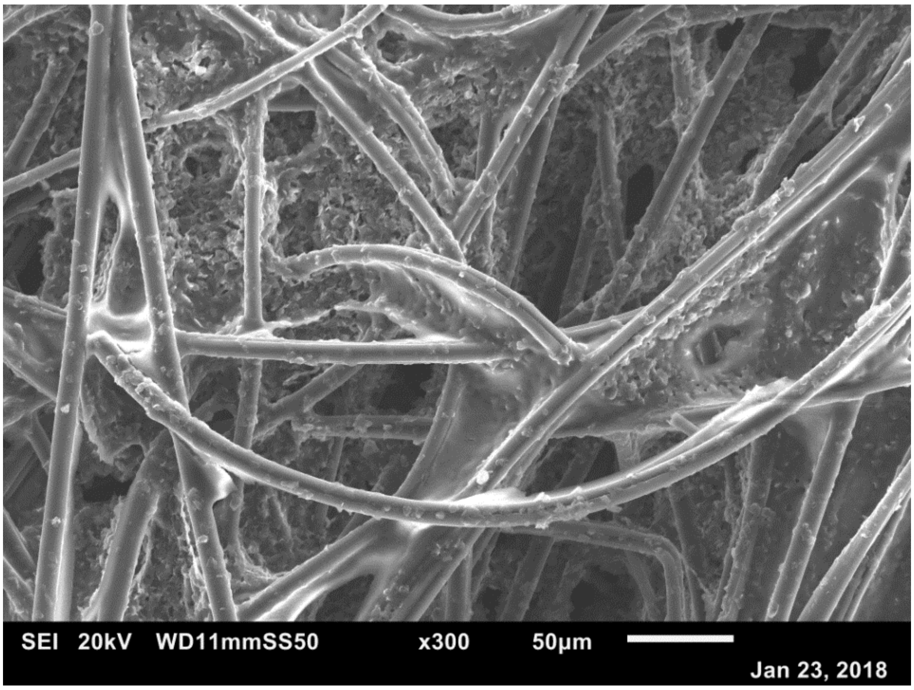
SEI 20kV WD11mmSS50 x300 50µm
Jan 23, 2018

(a)

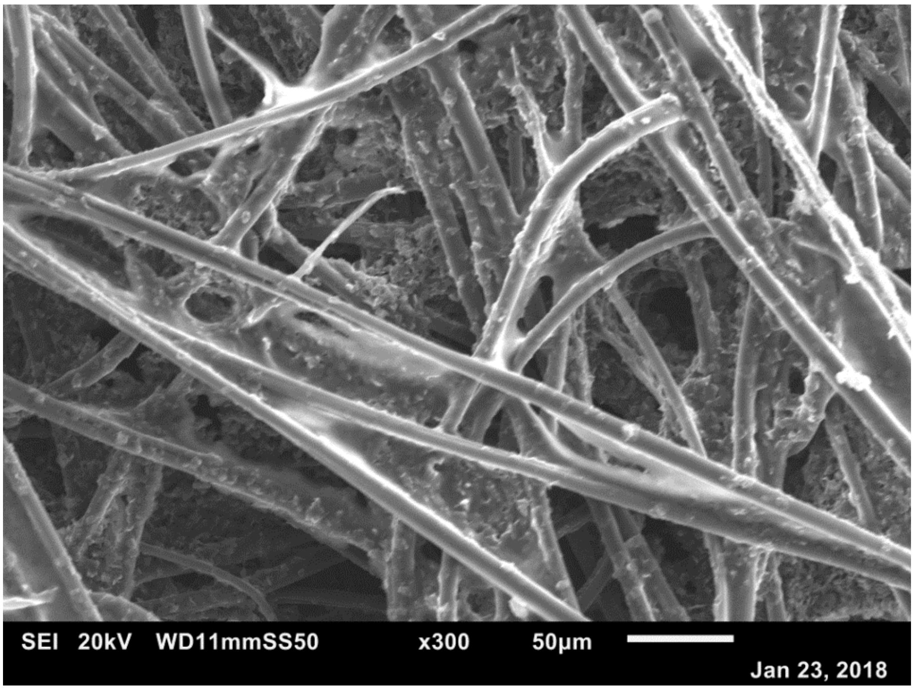
SEI 20kV WD11mmSS50 x300 50µm
Jan 23, 2018

(b)

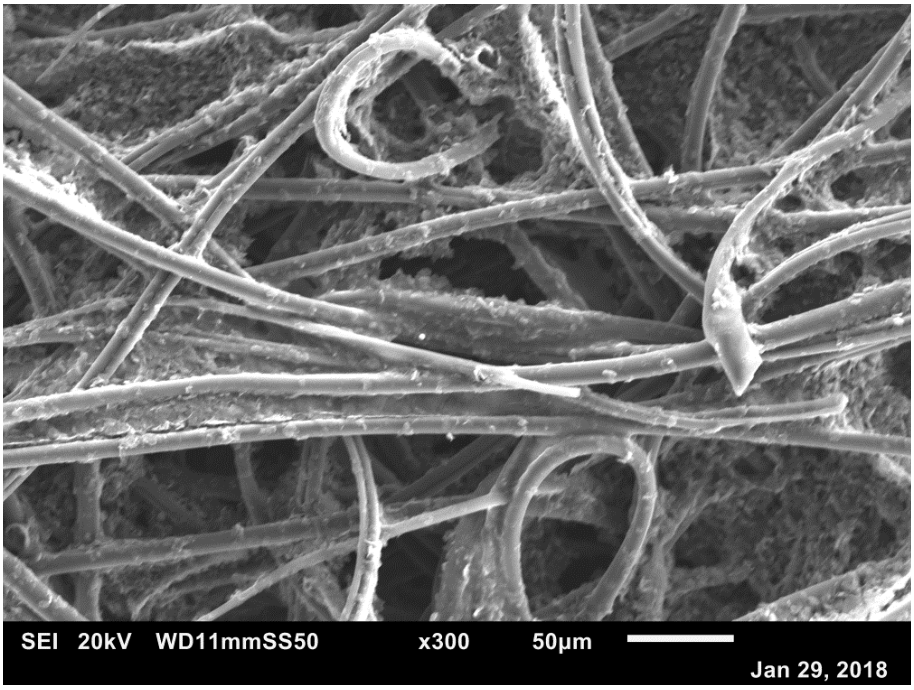

(c)

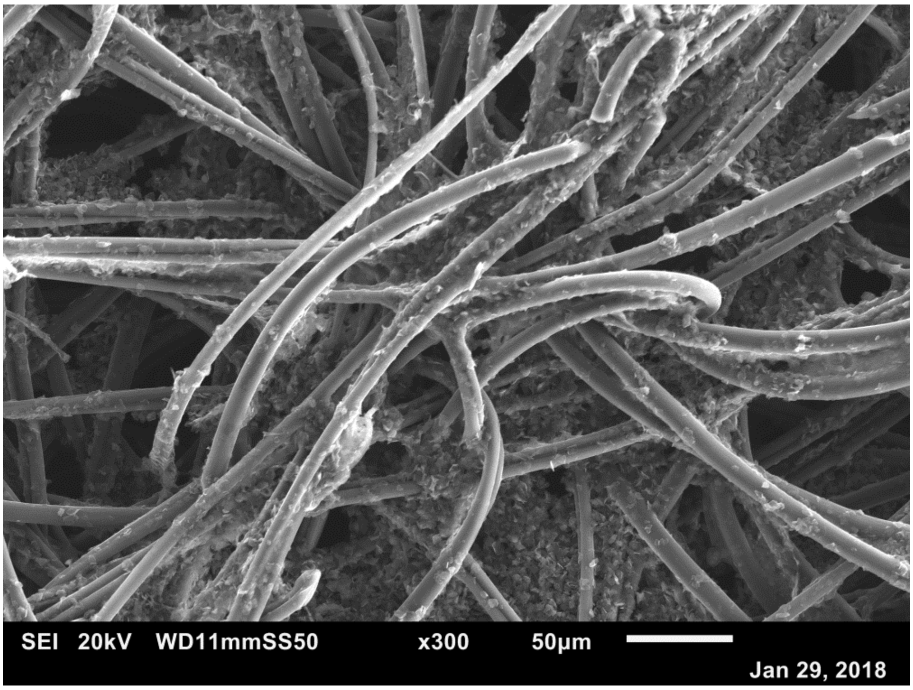

(d)

Figure 6.7: SEM images of SGL 10CA at 300x magnification (a) room temperature, (b) 200 °C, (c) 500 °C and (d) 800 °C.

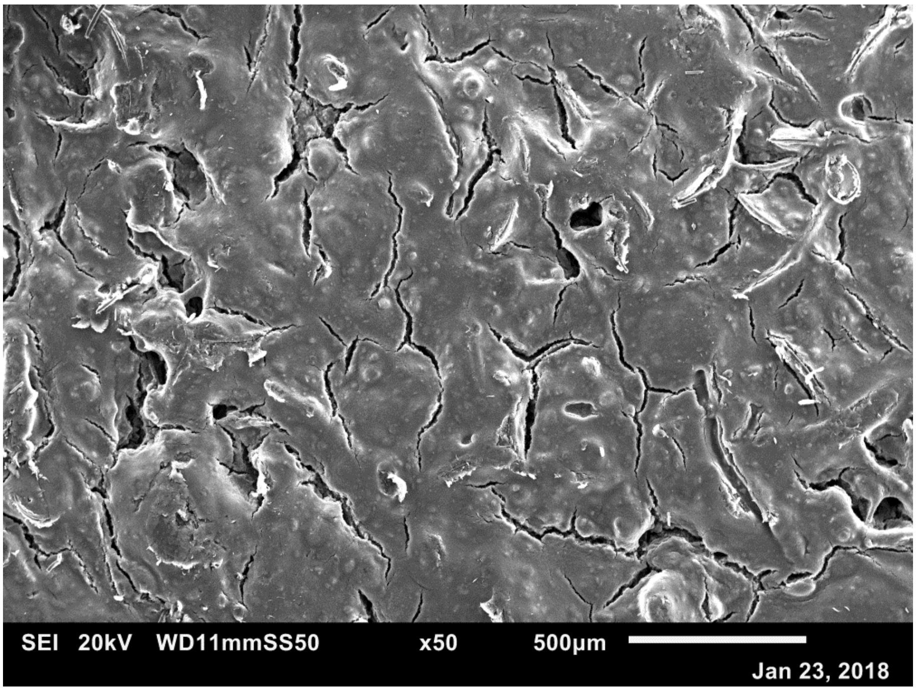
SEI 20kV WD11mmSS50 x50 500µm
Jan 23, 2018

(a)

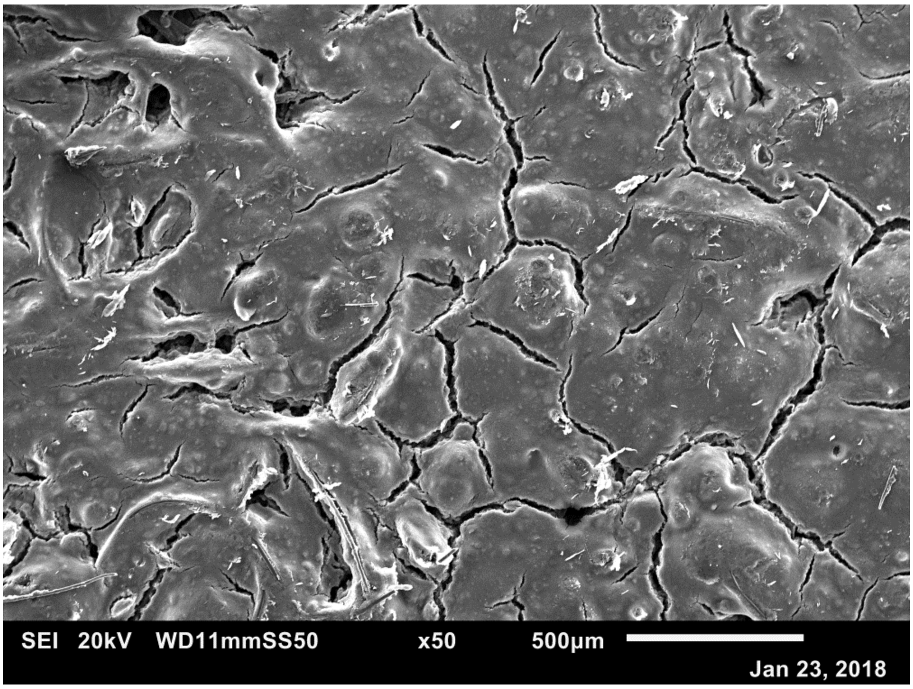
SEI 20kV WD11mmSS50 x50 500µm
Jan 23, 2018

(b)

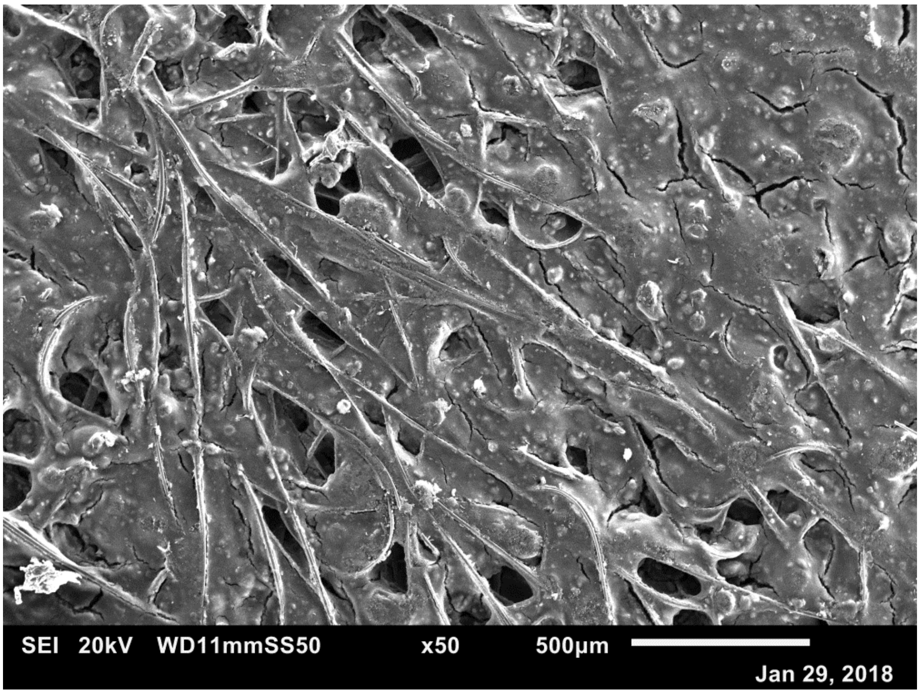

(c)

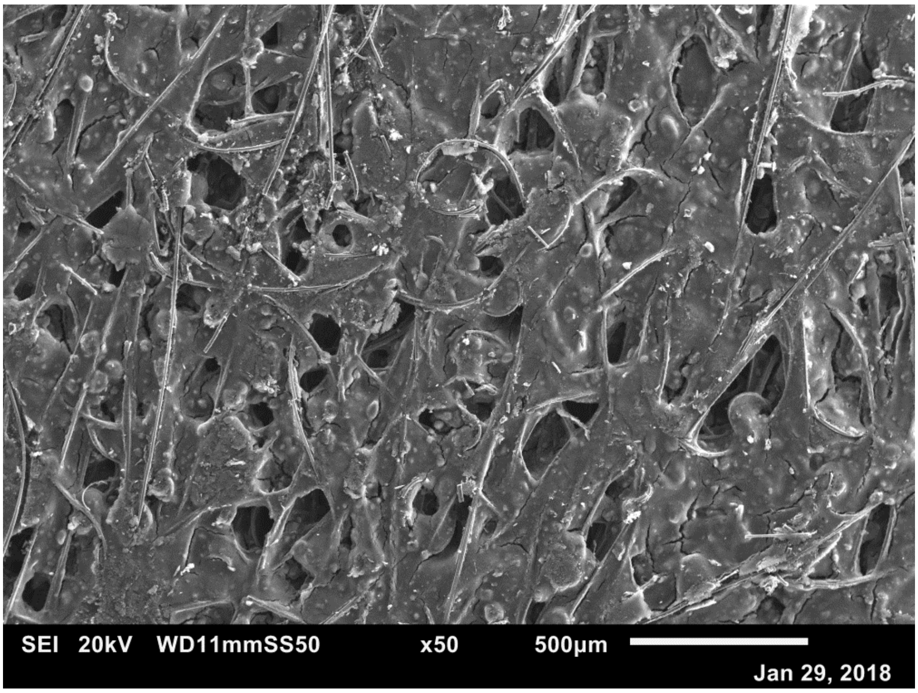

(d)

Figure 6.8: SEM images of SGL 10BC at 50x magnification (a) room temperature, (b) 200 °C, (c) 500 °C and (d) 800 °C.

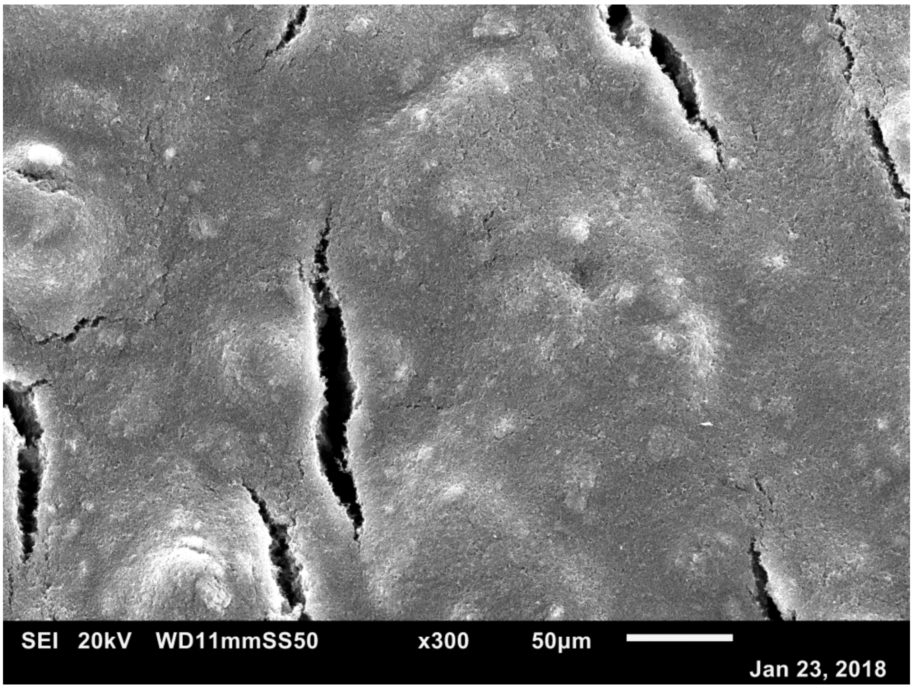
SEI 20kV WD11mmSS50 x300 50µm
Jan 23, 2018

(a)

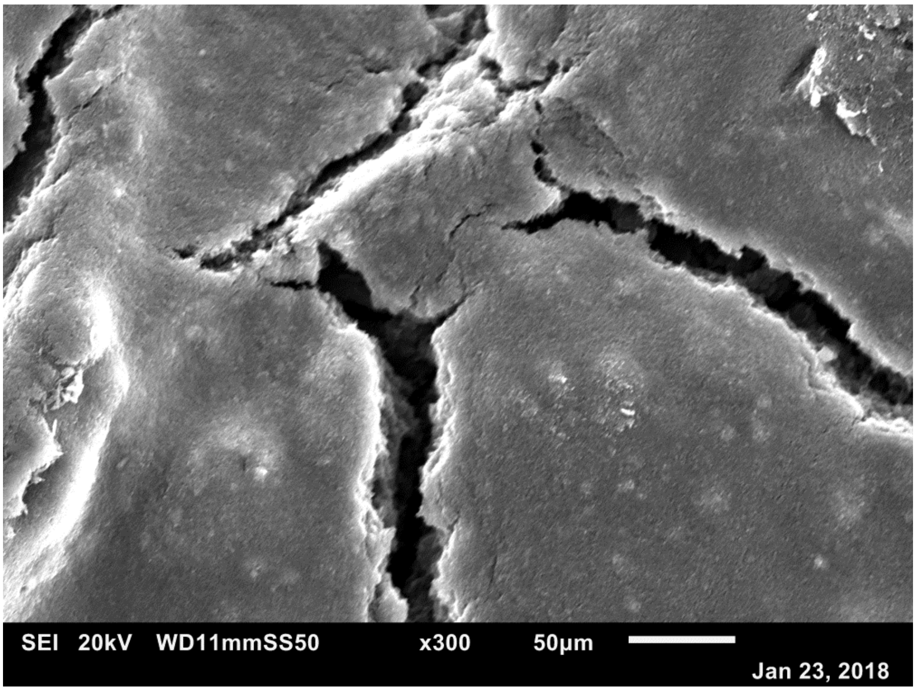
SEI 20kV WD11mmSS50 x300 50µm
Jan 23, 2018

(b)

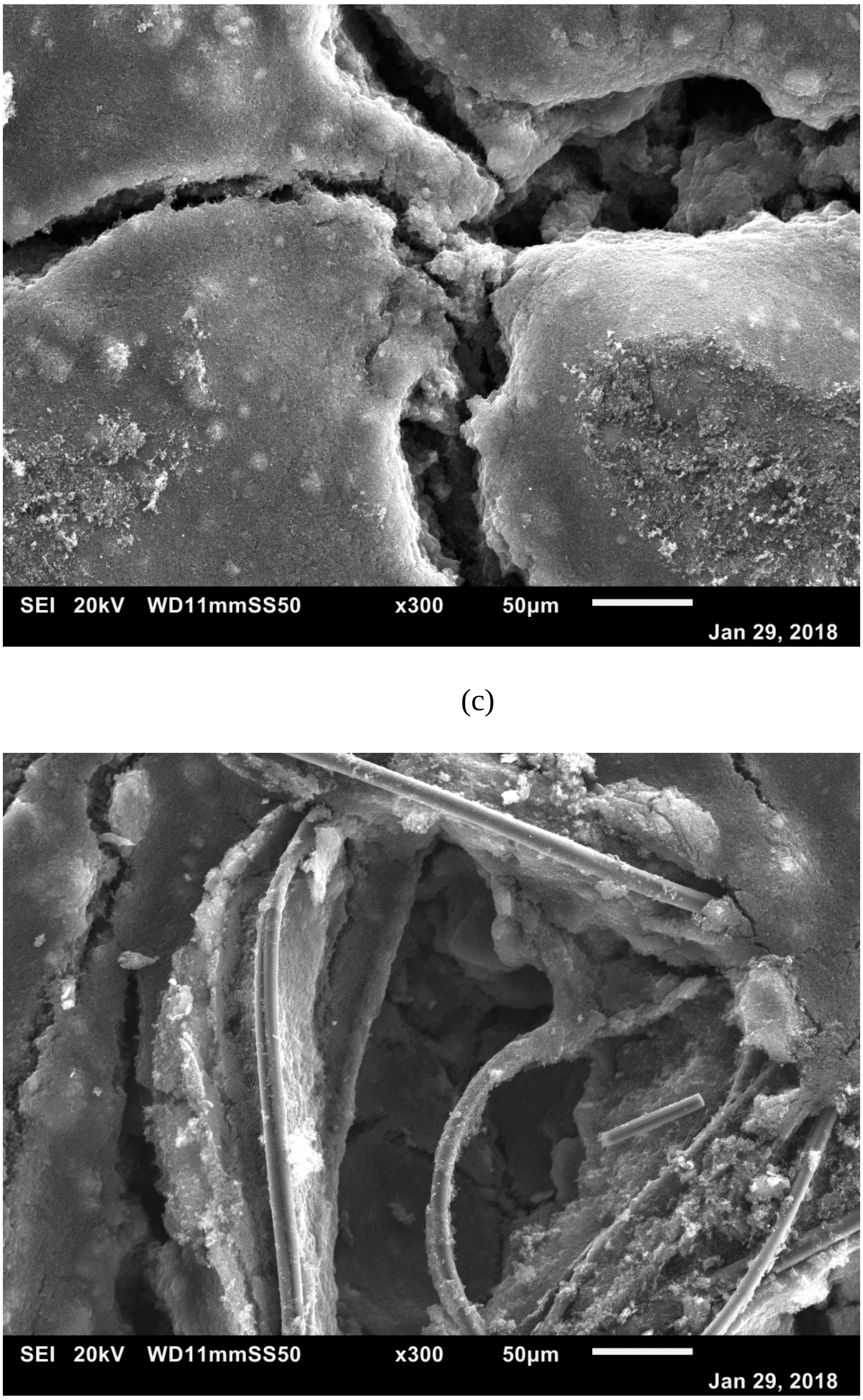

(c)

(d)

Figure 6.9: SEM images of SGL 10BC at 300x magnification (a) room temperature, (b) 200 °C, (c) 500 °C and (d) 800 °C.

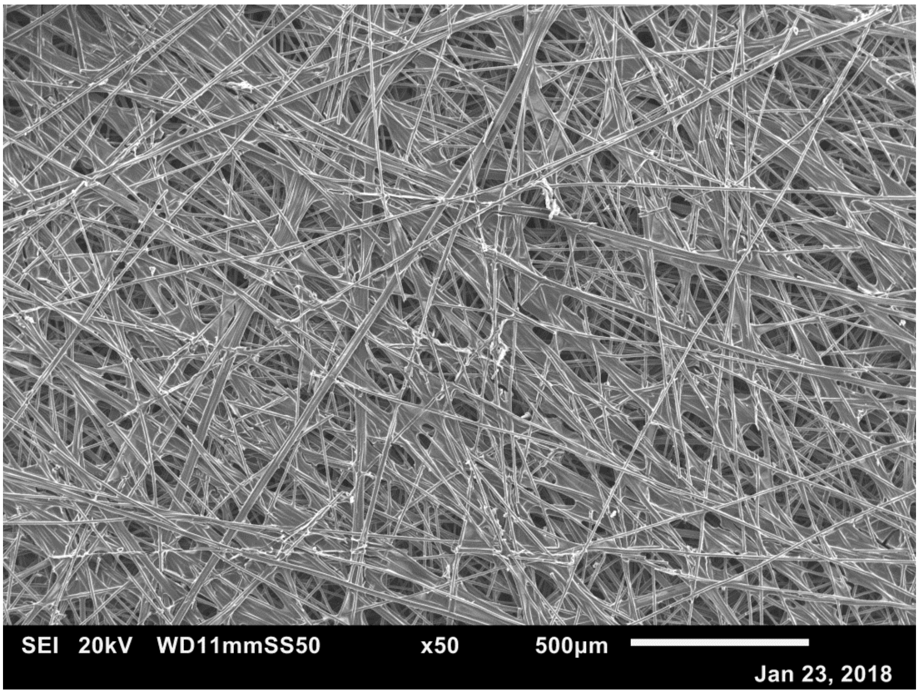
SEI 20kV WD11mmSS50 x50 500µm
Jan 23, 2018

(a)

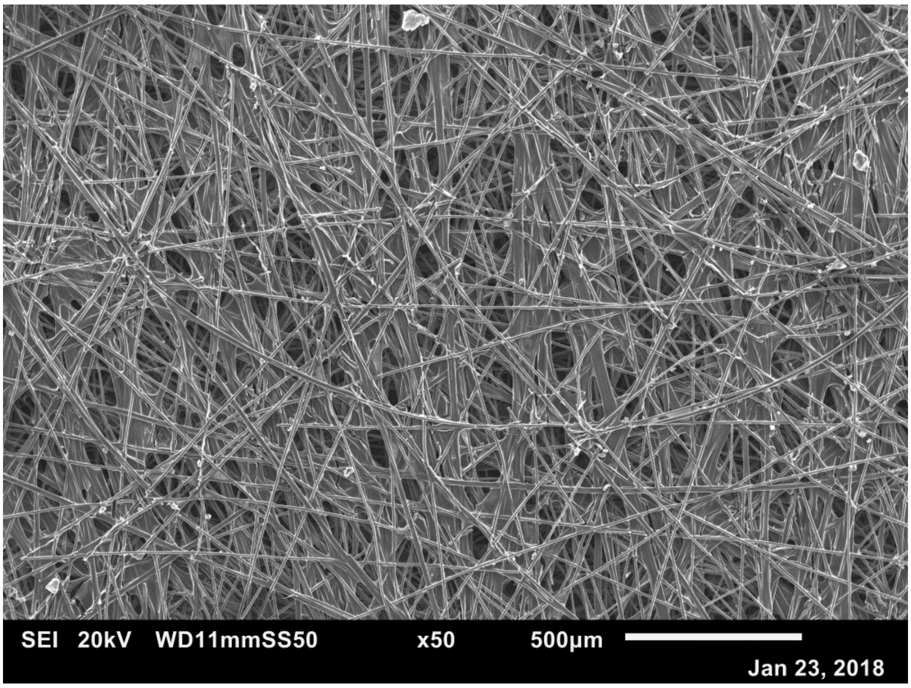
SEI 20kV WD11mmSS50 x50 500µm
Jan 23, 2018

(b)

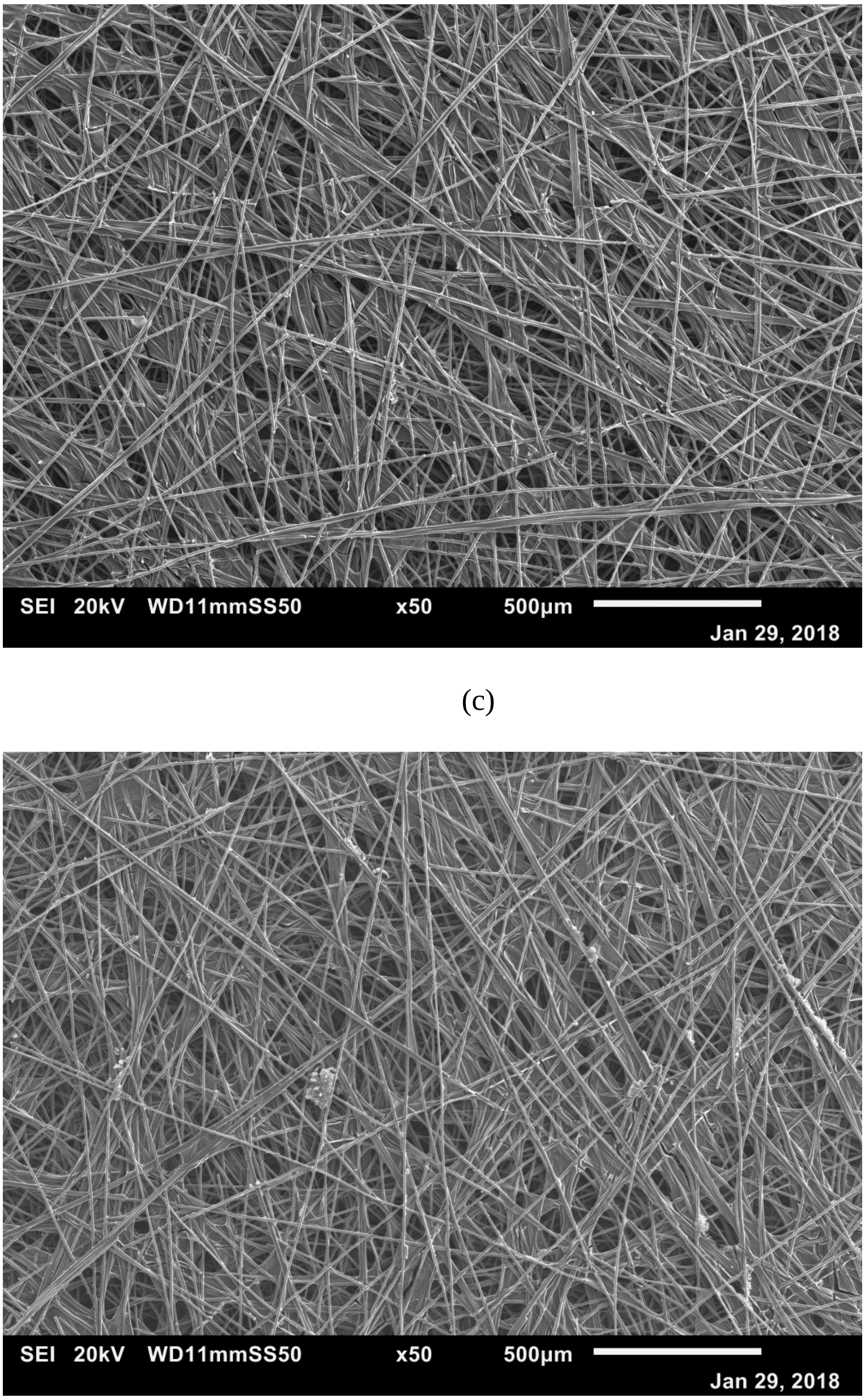

(c)

(d)

Figure 6.10: SEM images of Toray 060 at 50x magnification (a) room temperature, (b) 200 °C, (c) 500 °C and (d) 800 °C.

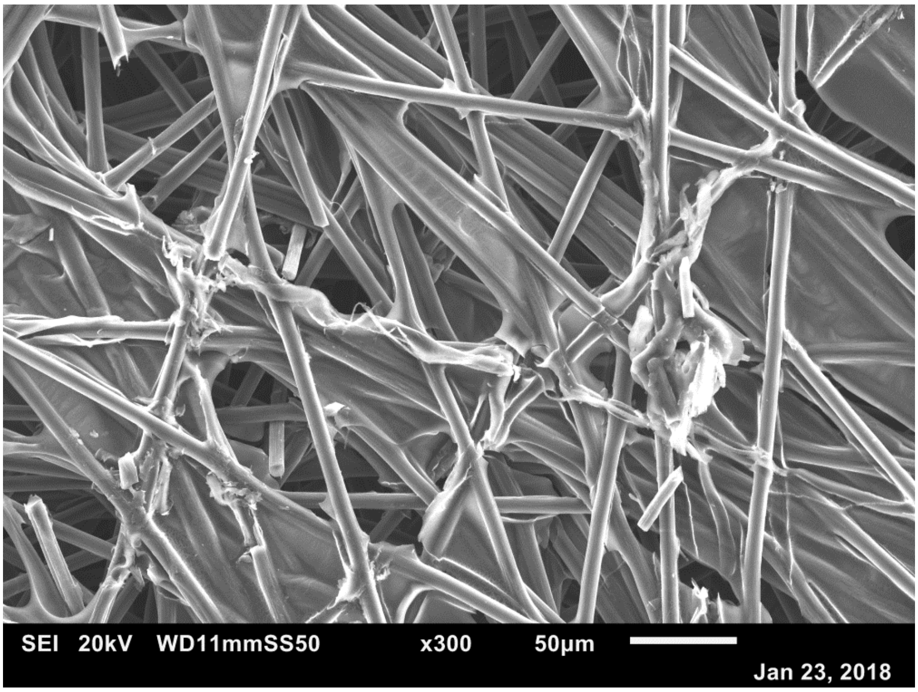
SEI 20kV WD11mmSS50 x300 50µm
Jan 23, 2018

(a)

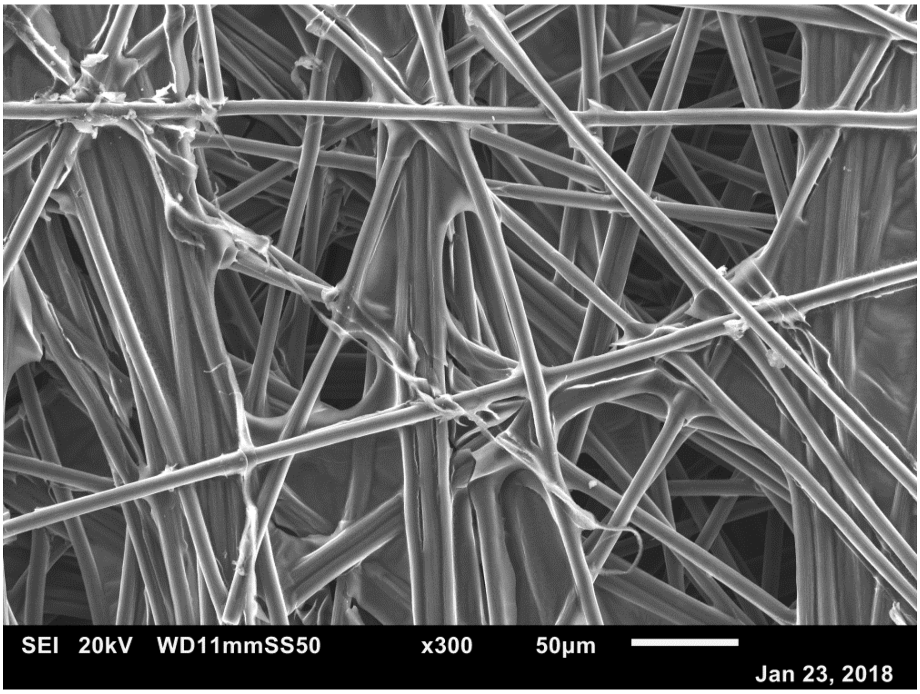
SEI 20kV WD11mmSS50 x300 50µm
Jan 23, 2018

(b)

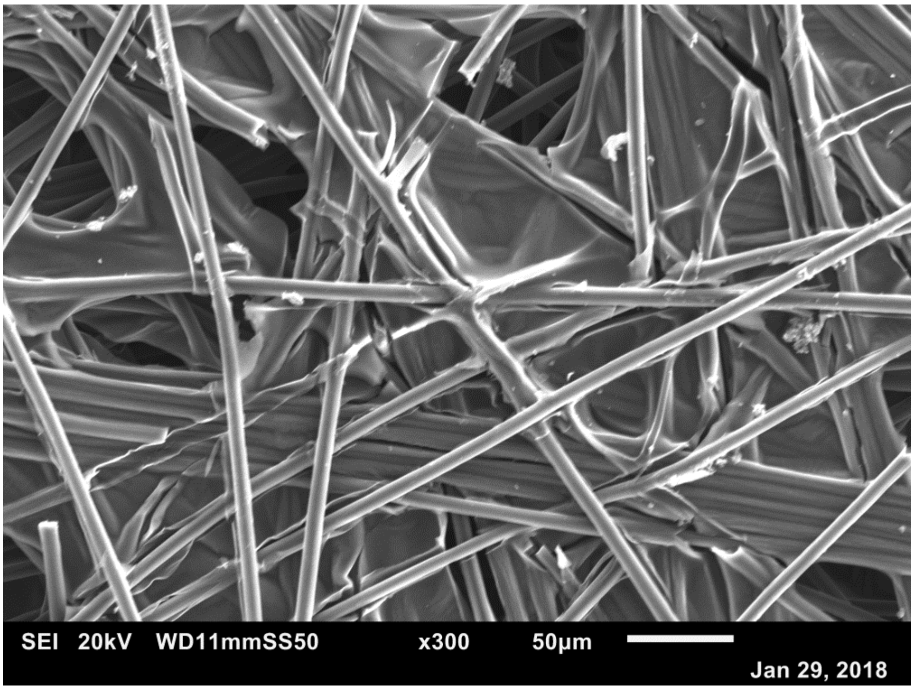

(c)

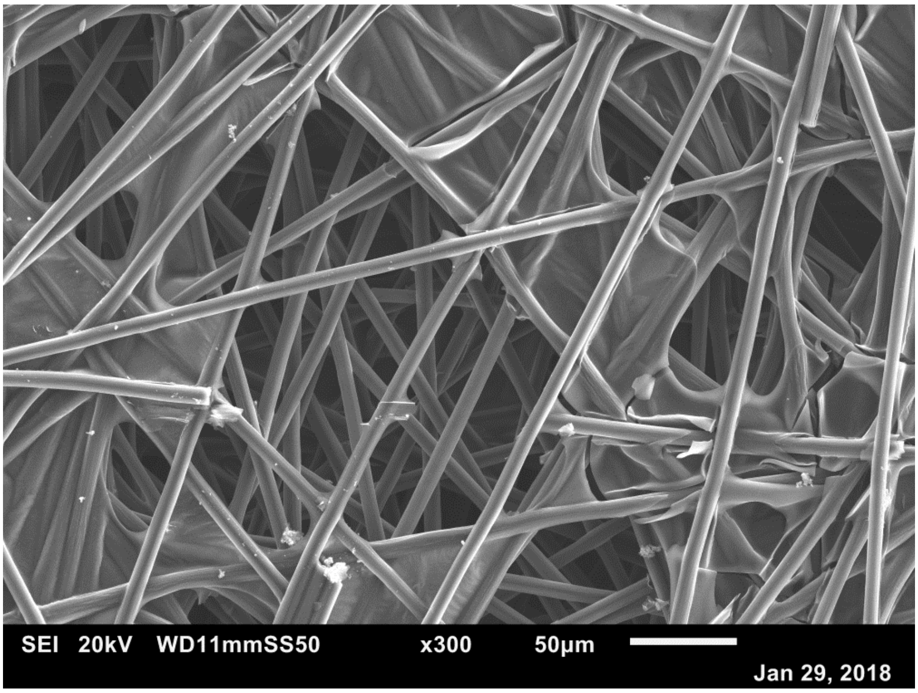

(d)

Figure 6.11: SEM images of Toray 060 at 300x magnification (a) room temperature, (b) 200 °C, (c) 500 °C and (d) 800 °C.

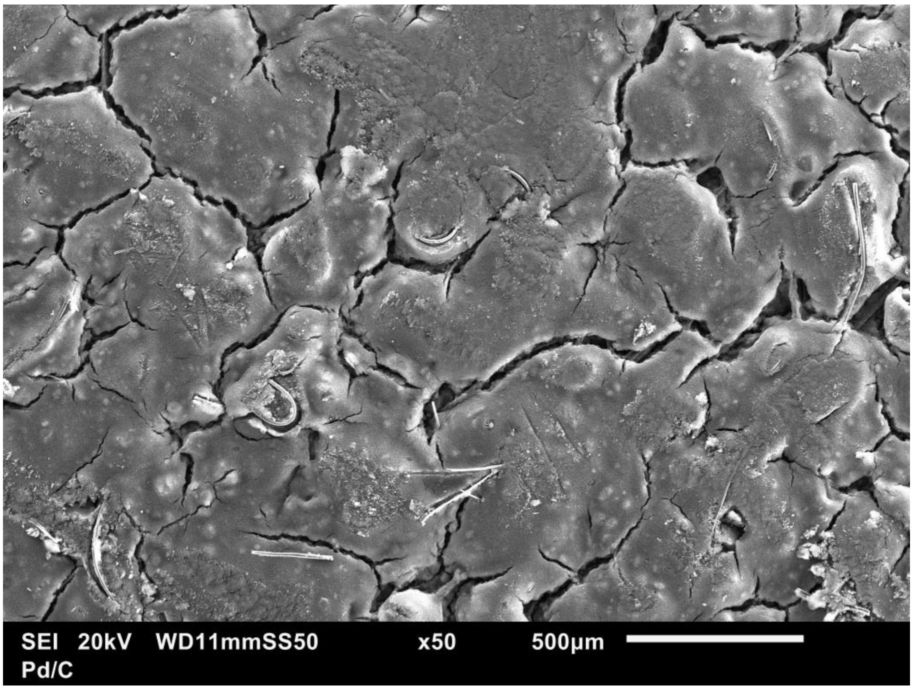

Figure 6.12: SEM image of SGL 10BC at 50x magnifications at 1000 C.

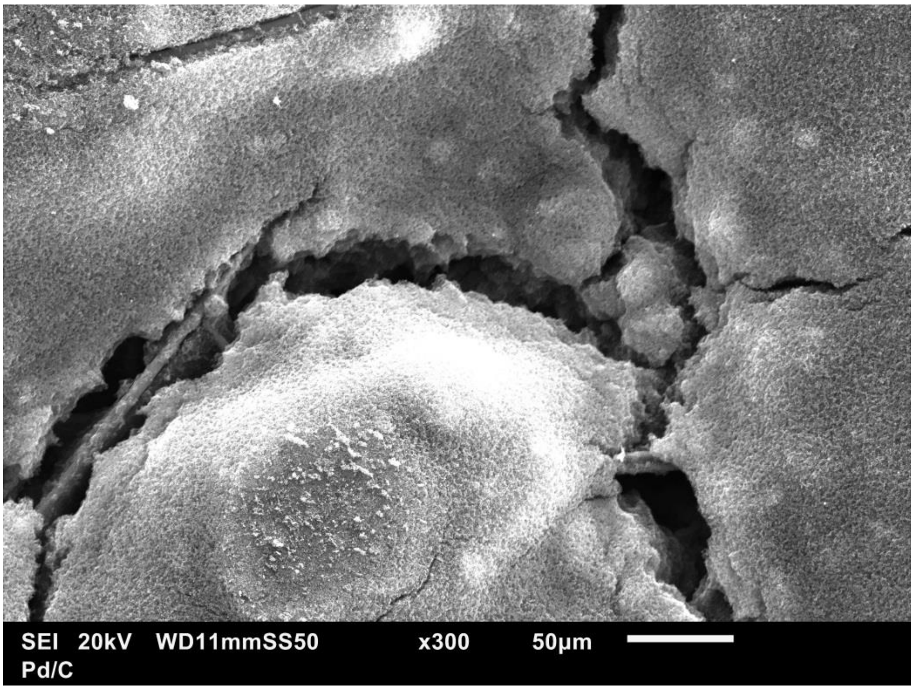

Figure 6.13: SEM image of SGL 10BC at 300x magnifications at 1000 C.

6.3 CHAPTER SUMMARY

In this chapter, the through-plane gas permeability of the GDL samples, namely SGL 10CA, SGL 10BC and Toray 060 have been experimentally investigated under the effect of heat treatment processing. The following are the main observations and findings:

- The through-plane gas permeability of the SGL 10CA and Toray 060 increases as the heat-treatment temperature increases.
- The through-plane gas permeability of the MPL-coated GDL sample i.e. SGL 10BC increases from room temperature to 500 °C. However, further heating at 800 °C and 1000 °C for SGL 10BC shows a reduction in the through-plane gas permeability.
- The morphological changes on the surface of the GDL samples may explain the through-plane gas permeability trend. The number and size of the cracks on the surface after the heating process might be the reason behind the changes in through-plane gas permeability of the GDL samples.

CHAPTER 7

CONCLUSIONS AND FUTURE WORK

In this thesis, the water and thermal management of PEM fuel cells have been experimentally investigated. The investigations involved the use of an in-house fuel cell test station, a commercially available and in-house modified transparent PEM fuel cell, and in-house gas permeability setup. The objectives of these investigations were to provide qualitative and quantitative measures for the effects of the operating conditions on the generation of liquid water and heat. As an extension to the above investigations, the gas permeability of GDL material was measured after being subject to relatively higher temperatures (>100 °C). This has been performed to gain insights on how the structure of the GDL material is affected when the fuel cell operates at such high temperatures to overcome water flooding. The below are the main findings of the thesis.

7.1 CONCLUSIONS

1. A new quantitative parameter, wetted bend ratio, has been introduced to quantify the amount of liquid water in the flow channels and to signify how flooded the fuel cell is under various operating conditions.
2. In most of the investigations, it is shown that the trends of the wetted ratio numbers for both the cathode and anode have been similar. This implies that the anode side, where there is no water production, can also be used

to explain the relationship between the fuel cell performance and the operating conditions.

3. There is an existence of optimum values for the air and hydrogen flow rates. These values form the trade-off between the positive effect of purging the liquid water from the flow channel and the negative effect of the membrane dry-out.
4. Also, there is an existence of optimum value for the air relative humidity which is trade-off between the positive effect of membrane hydration and negative effect of water flooding. On the other hand, the fuel cell performance was found to increase with increasing hydrogen relative humidity. As expected, the wetted bend ratio was found to be increased as the relative humidity of either air or hydrogen increases.
5. As the operating pressure increases, the fuel cell performance and the wetted bend ratio increases.
6. The temperature distribution along the MEA at the cathode side becomes more non-uniformed as air flow rate increases. This could be attributed to the observation that the liquid water (which has significantly larger thermal conductivity than air) in the cathode flow channels become less as the air flow rate increases, thus resulting in less efficient heat dissipation.
7. In relevance to the above point, it was found that the temperature distribution across the MEA becomes less uniformed as the wetted ratio number decreases.
8. For the given in-house modified transparent fuel cell, the fuel cell performance decreases as the air flow rate increases. This was attributed

to the increase in the rate of water removal from the cathode which increasing air flow rate, leading to the availability of less water to adequately humidify the membrane electrolyte.

9. Finally, it has been found that the through plane of gas permeability of GDL samples slightly increases with increasing temperature in the range from 20 °C to 800 °C. This somewhat imparts confidence in the use of such materials in high-temperature PEM fuel cells.

7.2 FUTURE WORK

The items below are some recommendations for future work:

1. In this thesis, the operating conditions investigated were reactant flow rates, relative humidity of the reacting gases and operating pressure. However, the effects of cell temperature have not been investigated as it is rather complicated to control the temperature of the transparent PEM fuel cell. Therefore, devising a method to control and measure the temperature of the transparent PEM fuel cell is an interesting future work.
2. It would be interesting and insightful to thermally visualise the temperature of the anode and cathode sides simultaneously. Due to a limitation in the availability of the thermal camera, only the cathode side has been thermally visualised. It has been selected as it is the side in which most of the heat is generated.
3. Due to the presence of some technical problems, only the effects of air flow rates on the temperature distribution across the MEA have been investigated. Therefore, an investigation, in which the effects of other operating conditions (e.g. hydrogen flow rate, relative humidity,

operating pressure and cell temperature) on the distribution of the temperature are explored, is highly recommended.

4. The thinning of the cathode transparent plate of the fuel cell has resulted in lower fuel cell performance. This is attributed to the poor contact between the MEA and the current collectors of the fuel cell resulting from the thinning of the transparent plates. A new material for transparent plates, which is stiffer than that used in this investigation, is highly recommended.
5. In Chapter 6, the GDL materials were subject to one-hour heat-treatment before measuring their gas permeability. PEM fuel cells are normally operated for significantly longer hours. Hence, it will be of interest to investigate the effect of time of heat-treatment on the through plane of the GDL.

REFERENCES

[1] A. M. Omer, “Energy, environment and sustainable development,” *Renew. Sustain. Energy Rev.*, vol. 12, no. 9, pp. 2265–2300, Dec. 2008.

[2] U.S. Energy Information Agency, “International Energy Outlook 2013,” *Outlook 2013*, p. 312, 2013.

[3] S. Shafiee and E. Topal, “When will fossil fuel reserves be diminished?,” *Energy Policy*, vol. 37, no. 1, pp. 181–189, Jan. 2009.

[4] K. Sopian and W. R. Wan Daud, “Challenges and future developments in proton exchange membrane fuel cells,” *Renew. Energy*, vol. 31, no. 5, pp. 719–727, Apr. 2006.

[5] J. T. Arias, J. C. Higuita, and O. D. Castrillón, “BP Annual Report 2012,” *Cuad. Admnistracion*, vol. 23, no. 41, pp. 81–105, 2010.

[6] L. Chiari and A. Zecca, “Constraints of fossil fuels depletion on global warming projections,” *Energy Policy*, vol. 39, no. 9, pp. 5026–5034, Sep. 2011.

[7] D. Y. C. Leung, G. Caramanna, and M. M. Maroto-Valer, “An overview of current status of carbon dioxide capture and storage technologies,” *Renew. Sustain. Energy Rev.*, vol. 39, pp. 426–443, 2014.

[8] H. L. (Eds. . Solomon, S., Qin, D., Manning, M., Chen, Z., Marquis, M., Averyt, K.B., Tignor, M., Miller, *Intergovernmental Panel on Climate Change (IPCC), 2007. Climate Change 2007: The Physical Science Basis*. Cambridge University Press, Cambridge, United Kingdom and New York, NY, USA, 2007.

[9] Unfccc, “Kyoto Protocol To the United Nations Framework Kyoto Protocol

To the United Nations Framework," *Rev. Eur. Community Int. Environ. Law*, vol. 7, pp. 214–217, 1998.

[10] House of Commons Energy and Climate Change Committee Carbon capture and storage, "Carbon Capture and Storage," *Ninth Rep. Sess. 2013–14*, no. London: The Stationery Office Limited, 2014.

[11] UK Parliament, "Climate Change Act 2008," pp. 1–103, 2008.

[12] UNFCCC. Conference of the Parties (COP), "Paris Climate Change Conference-November 2015, COP 21," *Adopt. Paris Agreement. Propos. by Pres.*, vol. 21932, no. December, p. 32, 2015.

[13] U.S. Energy Information, "Annual Energy Outlook 2013," *Off. Integr. Int. Energy Anal.*, vol. 1, pp. 1–244, 2013.

[14] U.S. Energy Information Administration, *International Energy Outlook 2016*, vol. 0484(2016), no. May 2016. 2016.

[15] G. W. Crabtree, M. S. Dresselhaus, and M. V. Buchanan, "The Hydrogen Economy," *Phys. Today*, vol. 57, no. 12, p. 39, 2004.

[16] F. Barbir, *PEM Fuel Cells : Theory and Practice ACADEMIC PRESS*. Elsevier Academic Press, 2005.

[17] K. Prater, "(1990) 239 - 250 239 the renaissance of the solid polymer fuel cell keith prater," vol. 29, pp. 239–250, 1990.

[18] T. Branch and N. A. Space, "The fuel cell in space: yesterday," vol. 29, pp. 193–200, 1990.

[19] G. McLean, "An assessment of alkaline fuel cell technology," *Int. J. Hydrogen Energy*, vol. 27, no. 5, pp. 507–526, 2002.

[20] N. Sammes, R. Bove, and K. Stahl, "Phosphoric acid fuel cells: Fundamentals and applications," *Curr. Opin. Solid State Mater. Sci.*, vol. 8, no. 5, pp. 372–

378, 2004.

[21] A. L. Dicks, “Molten carbonate fuel cells,” *Curr. Opin. Solid State Mater. Sci.*, vol. 8, no. 5, pp. 379–383, 2004.

[22] C. Lamy, A. Lima, V. LeRhun, F. Delime, C. Coutanceau, and J. M. Léger, “Recent advances in the development of direct alcohol fuel cells (DAFC),” *J. Power Sources*, vol. 105, no. 2, pp. 283–296, 2002.

[23] H. Liu, C. Song, L. Zhang, J. Zhang, H. Wang, and D. P. Wilkinson, “A review of anode catalysis in the direct methanol fuel cell,” *J. Power Sources*, vol. 155, no. 2, pp. 95–110, 2006.

[24] A. B. Stambouli and E. Traversa, “Solid oxide fuel cells (SOFCs): A review of an environmentally clean and efficient source of energy,” *Renew. Sustain. Energy Rev.*, vol. 6, no. 5, pp. 433–455, 2002.

[25] N. Mahato, A. Banerjee, A. Gupta, S. Omar, and K. Balani, “Progress in material selection for solid oxide fuel cell technology: A review,” *Prog. Mater. Sci.*, vol. 72, pp. 141–337, 2015.

[26] “Toyota Mirai: the facts | Toyota UK.” [Online]. Available: https://www.toyota.co.uk/new-cars/new-mirai/the-facts. [Accessed: 16-Mar-2018].

[27] “Toyota to recall all 2,800 Mirai fuel cell cars on the road.” [Online]. Available: https://www.reuters.com/article/us-toyota-recall-fuelcells/toyota-to-recall-all-2800-mirai-fuel-cell-cars-on-the-road-idUSKBN15U0F1. [Accessed: 16-Mar-2018].

[28] C. Dyer, “Fuel cells for portable applications,” *Fuel Cells Bull.*, no. 42, pp. 9–10, 2002.

[29] J. Stumper and C. Stone, “Recent advances in fuel cell technology at Ballard,”

J. Power Sources, vol. 176, no. 2, pp. 468–476, Feb. 2008.

[30] F. Barbir and S. Yazici, “Status and development of PEM fuel cell technology,” no. October 2007, pp. 369–378, 2008.

[31] A. Li and S. H. Chan, “Understanding the role of cathode structure and property on water management and electrochemical performance of a PEM fuel cell,” *Int. J. Hydrogen Energy*, vol. 38, no. 27, pp. 11988–11995, Sep. 2013.

[32] S. Litster and G. McLean, “PEM fuel cell electrodes,” *J. Power Sources*, vol. 130, no. 1–2, pp. 61–76, May 2004.

[33] V. Mehta and J. S. Cooper, “Review and analysis of PEM fuel cell design and manufacturing,” *J. Power Sources*, vol. 114, no. 1, pp. 32–53, Feb. 2003.

[34] R. Borup, J. Meyers, B. Pivovar, Y. S. Kim, R. Mukundan, N. Garland, D. Myers, M. Wilson, F. Garzon, D. Wood, P. Zelenay, K. More, K. Stroh, T. Zawodzinski, J. Boncella, J. E. McGrath, M. Inaba, K. Miyatake, M. Hori, K. Ota, Z. Ogumi, S. Miyata, A. Nishikata, Z. Siroma, Y. Uchimoto, K. Yasuda, K.-I. Kimijima, and N. Iwashita, “Scientific aspects of polymer electrolyte fuel cell durability and degradation.,” *Chem. Rev.*, vol. 107, no. 10, pp. 3904–51, Oct. 2007.

[35] L. Carrette, K. a Friedrich, and U. Stimming, “Fuel cells: principles, types, fuels, and applications.,” *Chemphyschem*, vol. 1, no. 4, pp. 162–93, Dec. 2000.

[36] J. Larminie and A. Dicks, *Fuel cell systems explained*. 2003.

[37] S. Park, J.-W. Lee, and B. N. Popov, “A review of gas diffusion layer in PEM fuel cells: Materials and designs,” *Int. J. Hydrogen Energy*, vol. 37, no. 7, pp. 5850–5865, Apr. 2012.

[38] L. Cindrella, a. M. Kannan, J. F. Lin, K. Saminathan, Y. Ho, C. W. Lin, and J. Wertz, “Gas diffusion layer for proton exchange membrane fuel cells—A review,” *J. Power Sources*, vol. 194, no. 1, pp. 146–160, Oct. 2009.

[39] S. Escribano, J.-F. Blachot, J. Ethève, A. Morin, and R. Mosdale, “Characterization of PEMFCs gas diffusion layers properties,” *J. Power Sources*, vol. 156, no. 1, pp. 8–13, May 2006.

[40] A. Z. Weber and J. Newman, “Effects of Microporous Layers in Polymer Electrolyte Fuel Cells,” *J. Electrochem. Soc.*, vol. 152, p. A677, 2005.

[41] M. S. Wilson, J. a. Valerio, and S. Gottesfeld, “Low platinum loading electrodes for polymer electrolyte fuel cells fabricated using thermoplastic ionomers,” *Electrochim. Acta*, vol. 40, no. 3, pp. 355–363, 1995.

[42] Z. Qi and A. Kaufman, “Improvement of water management by a microporous sublayer for PEM fuel cells,” *J. Power Sources*, vol. 109, pp. 38–46, 2002.

[43] E. Passalacqua, F. Lufrano, G. Squadrito, a Patti, and L. Giorgi, “Influence of the structure in low-Pt loading electrodes for polymer electrolyte fuel cells,” *Electrochim. Acta*, vol. 43, no. 24, pp. 3665–3673, 1998.

[44] L. R. Jordan, a K. Shukla, T. Behrsing, N. R. Avery, B. C. Muddle, and M. Forsyth, “Effect of diffusion-layer morphology on the performance of polymer electrolyte fuel cells operating at atmospheric pressure,” *J. Appl. Electrochem.*, no. 30, pp. 641–646, 2000.

[45] C. S. Kong, D. Y. Kim, H. K. Lee, Y. G. Shul, and T. H. Lee, “Influence of pore-size distribution of diffusion layer on mass-transport problems of proton exchange membrane fuel cells,” *J. Power Sources*, vol. 108, no. 1–2, pp. 185–191, 2002.

[46] Y. Tabe, Y. Aoyama, K. Kadowaki, K. Suzuki, and T. Chikahisa, “Impact of

micro-porous layer on liquid water distribution at the catalyst layer interface and cell performance in a polymer electrolyte membrane fuel cell," *J. Power Sources*, vol. 287, pp. 422–430, 2015.

[47] S. Hirano, J. Kim, and S. Srinivasan, "High performance proton exchange membrane fuel cells with sputter-deposited Pt layer electrodes," *Electrochim. Acta*, vol. 42, no. 10, pp. 1587–1593, 1997.

[48] D. Malevich, E. Halliop, B. a. Peppley, J. G. Pharoah, and K. Karan, "Investigation of Charge-Transfer and Mass-Transport Resistances in PEMFCs with Microporous Layer Using Electrochemical Impedance Spectroscopy," *J. Electrochem. Soc.*, vol. 156, no. 2, p. B216, 2009.

[49] T. Kim, S. Lee, and H. Park, "A study of water transport as a function of the micro-porous layer arrangement in PEMFCs," *Int. J. Hydrogen Energy*, vol. 35, no. 16, pp. 8631–8643, 2010.

[50] Z. Zhan, J. Xiao, D. Li, M. Pan, and R. Yuan, "Effects of porosity distribution variation on the liquid water flux through gas diffusion layers of PEM fuel cells," *J. Power Sources*, vol. 160, no. 2 SPEC. ISS., pp. 1041–1048, 2006.

[51] S. Shimpalee, U. Beuscher, and J. W. Van Zee, "Investigation of gas diffusion media inside PEMFC using CFD modeling," *J. Power Sources*, vol. 163, no. 1 SPEC. ISS., pp. 480–489, 2006.

[52] T. Sasabe, P. Deevanhxay, S. Tsushima, and S. Hirai, "Investigation on the effect of microstructure of proton exchange membrane fuel cell porous layers on liquid water behavior by soft X-ray radiography," *J. Power Sources*, vol. 196, no. 20, pp. 8197–8206, Oct. 2011.

[53] A. Casalegno, L. Colombo, S. Galbiati, and R. Marchesi, "Quantitative characterization of water transport and flooding in the diffusion layers of

polymer electrolyte fuel cells," *J. Power Sources*, vol. 195, no. 13, pp. 4143–4148, 2010.

[54] J. M. Lamanna and S. G. Kandlikar, "Determination of effective water vapor diffusion coefficient in pemfc gas diffusion layers," *Int. J. Hydrogen Energy*, vol. 36, no. 8, pp. 5021–5029, 2011.

[55] M. Mortazavi and K. Tajiri, "Liquid water breakthrough pressure through gas diffusion layer of proton exchange membrane fuel cell," *Int. J. Hydrogen Energy*, vol. 39, no. 17, pp. 9409–9419, 2014.

[56] J. Lee, J. Hinebaugh, and a. Bazylak, "Synchrotron X-ray radiographic investigations of liquid water transport behavior in a PEMFC with MPL-coated GDLs," *J. Power Sources*, vol. 227, pp. 123–130, Apr. 2013.

[57] H. Meng, "Multi-dimensional liquid water transport in the cathode of a PEM fuel cell with consideration of the micro-porous layer (MPL)," *Int. J. Hydrogen Energy*, vol. 34, no. 13, pp. 5488–5497, 2009.

[58] J. Chen, T. Matsuura, and M. Hori, "Novel gas diffusion layer with water management function for PEMFC," *J. Power Sources*, vol. 131, no. 1–2, pp. 155–161, 2004.

[59] G. Lin and T. Van Nguyen, "Effect of Thickness and Hydrophobic Polymer Content of the Gas Diffusion Layer on Electrode Flooding Level in a PEMFC," *J. Electrochem. Soc.*, vol. 152, no. 10, p. A1942, 2005.

[60] D. Spernjak, A. K. Prasad, and S. G. Advani, "Experimental investigation of liquid water formation and transport in a transparent single-serpentine PEM fuel cell," *J. Power Sources*, vol. 170, no. 2, pp. 334–344, Jul. 2007.

[61] M. Blanco and D. P. Wilkinson, "Investigation of the effect of microporous layers on water management in a proton exchange membrane fuel cell using

novel diagnostic methods," *Int. J. Hydrogen Energy*, vol. 39, no. 29, pp. 16390–16404, 2014.

[62] U. Pasaogullari, C.-Y. Wang, and K. S. Chen, "Two-Phase Transport in Polymer Electrolyte Fuel Cells with Bilayer Cathode Gas Diffusion Media," *J. Electrochem. Soc.*, vol. 152, no. 8, p. A1574, 2005.

[63] J. H. Nam and M. Kaviany, "Effective diffusivity and water-saturation distribution in single- and two-layer PEMFC diffusion medium," *Int. J. Heat Mass Transf.*, vol. 46, no. 24, pp. 4595–4611, 2003.

[64] G. G. Park, Y. J. Sohn, T. H. Yang, Y. G. Yoon, W. Y. Lee, and C. S. Kim, "Effect of PTFE contents in the gas diffusion media on the performance of PEMFC," *J. Power Sources*, vol. 131, no. 1–2, pp. 182–187, 2004.

[65] U. Pasaogullari and C. Y. Wang, "Two-phase transport and the role of micro-porous layer in polymer electrolyte fuel cells," *Electrochim. Acta*, vol. 49, no. 25, pp. 4359–4369, 2004.

[66] J. H. Nam, K. J. Lee, G. S. Hwang, C. J. Kim, and M. Kaviany, "Microporous layer for water morphology control in PEMFC," *Int. J. Heat Mass Transf.*, vol. 52, no. 11–12, pp. 2779–2791, 2009.

[67] J. T. Gostick, M. a. Ioannidis, M. W. Fowler, and M. D. Pritzker, "On the role of the microporous layer in PEMFC operation," *Electrochem. commun.*, vol. 11, no. 3, pp. 576–579, 2009.

[68] Z. Lu, M. M. Daino, C. Rath, and S. G. Kandlikar, "Water management studies in PEM fuel cells, part III: Dynamic breakthrough and intermittent drainage characteristics from GDLs with and without MPLs," *Int. J. Hydrogen Energy*, vol. 35, no. 9, pp. 4222–4233, May 2010.

[69] H. K. Atiyeh, K. Karan, B. Peppley, A. Phoenix, E. Halliop, and J. Pharoah,

"Experimental investigation of the role of a microporous layer on the water transport and performance of a PEM fuel cell," *J. Power Sources*, vol. 170, no. 1, pp. 111–121, Jun. 2007.

[70] A. Thomas, G. Maranzana, S. Didierjean, J. Dillet, and O. Lottin, "Thermal and water transfer in PEMFCs: Investigating the role of the microporous layer," *Int. J. Hydrogen Energy*, vol. 39, no. 6, pp. 2649–2658, 2014.

[71] W. Lee, C.-H. Ho, J. W. Van Zee, and M. Murthy, "The effects of compression and gas diffusion layers on the performance of a PEM fuel cell," *J. Power Sources*, vol. 84, no. 1, pp. 45–51, Nov. 1999.

[72] P. C. Ghosh, "Influences of Contact Pressure on the Performances of Polymer Electrolyte Fuel Cells," *J. Energy*, vol. 2013, pp. 1–11, 2013.

[73] D. Ye and Z. Zhan, "A review on the sealing structures of membrane electrode assembly of proton exchange membrane fuel cells," *J. Power Sources*, vol. 231, pp. 285–292, Jun. 2013.

[74] X. Li and I. Sabir, "Review of bipolar plates in PEM fuel cells: Flow-field designs," *Int. J. Hydrogen Energy*, vol. 30, no. 4, pp. 359–371, Mar. 2005.

[75] a Hermann, T. Chaudhuri, and P. Spagnol, "Bipolar plates for PEM fuel cells: A review," *Int. J. Hydrogen Energy*, vol. 30, no. 12, pp. 1297–1302, Sep. 2005.

[76] W. Dai, H. Wang, X.-Z. Yuan, J. J. Martin, D. Yang, J. Qiao, and J. Ma, "A review on water balance in the membrane electrode assembly of proton exchange membrane fuel cells," *Int. J. Hydrogen Energy*, vol. 34, no. 23, pp. 9461–9478, Dec. 2009.

[77] H. Li, Y. Tang, Z. Wang, Z. Shi, S. Wu, D. Song, J. Zhang, K. Fatih, J. Zhang, H. Wang, Z. Liu, R. Abouatallah, and A. Mazza, "A review of water

flooding issues in the proton exchange membrane fuel cell," *J. Power Sources*, vol. 178, no. 1, pp. 103–117, Mar. 2008.

[78] K. Jiao and X. Li, "Water transport in polymer electrolyte membrane fuel cells," *Prog. Energy Combust. Sci.*, vol. 37, no. 3, pp. 221–291, Jun. 2011.

[79] Q. Yan, H. Toghiani, and J. Wu, "Investigation of water transport through membrane in a PEM fuel cell by water balance experiments," *J. Power Sources*, vol. 158, no. 1, pp. 316–325, Jul. 2006.

[80] A. Bazylak, "Liquid water visualization in PEM fuel cells: A review," *Int. J. Hydrogen Energy*, vol. 34, no. 9, pp. 3845–3857, May 2009.

[81] K. Tüber, D. Pócza, and C. Hebling, "Visualization of water buildup in the cathode of a transparent PEM fuel cell," *J. Power Sources*, vol. 124, no. 2, pp. 403–414, Nov. 2003.

[82] T. Ous and C. Arcoumanis, "Visualisation of water accumulation in the flow channels of PEMFC under various operating conditions," *J. Power Sources*, vol. 187, pp. 182–189, 2009.

[83] F.-B. Weng, A. Su, C.-Y. Hsu, and C.-Y. Lee, "Study of water-flooding behaviour in cathode channel of a transparent proton-exchange membrane fuel cell," *J. Power Sources*, vol. 157, no. 2, pp. 674–680, Jul. 2006.

[84] J. M. Sergi and S. G. Kandlikar, "Quantification and characterization of water coverage in PEMFC gas channels using simultaneous anode and cathode visualization and image processing," *Int. J. Hydrogen Energy*, vol. 36, no. 19, pp. 12381–12392, Sep. 2011.

[85] A. Bozorgnezhad, M. Shams, H. Kanani, M. Hasheminasab, and G. Ahmadi, "Two-phase flow and droplet behavior in microchannels of PEM fuel cell," *Int. J. Hydrogen Energy*, vol. 41, no. 42, pp. 1–18, 2016.

[86] Z. Zhan, C. Wang, W. Fu, and M. Pan, “Visualization of water transport in a transparent PEMFC,” *Int. J. Hydrogen Energy*, vol. 37, no. 1, pp. 1094–1105, Jan. 2012.

[87] X. Liu, H. Guo, and C. Ma, “Water flooding and two-phase flow in cathode channels of proton exchange membrane fuel cells,” *J. Power Sources*, vol. 156, no. 2, pp. 267–280, Jun. 2006.

[88] A. Ramiar, A. A. Ranjbar, and E. Alizadeh, “Design , manufacturing , assembling and testing of a transparent PEM fuel cell for investigation of water management and contact resistance at dead-end mode,” *Int. J. Hydrogen Energy*, vol. 42, no. 16, pp. 11673–11688, 2017.

[89] S. G. Kandlikar and Z. Lu, “Thermal management issues in a PEMFC stack – A brief review of current status,” *Appl. Therm. Eng.*, vol. 29, no. 7, pp. 1276–1280, May 2009.

[90] S. G. Goebel, “Evaporative cooled fuel cell,” vol. 2, no. 12, 2005.

[91] M. J. Lampinen, “Analysis of Free Energy and Entropy Changes for Half-Cell Reactions,” *J. Electrochem. Soc.*, vol. 140, no. 12, p. 3537, 1993.

[92] M. Wang, H. Guo, and C. Ma, “Temperature distribution on the MEA surface of a PEMFC with serpentine channel flow bed,” *J. Power Sources*, vol. 157, no. 1, pp. 181–187, 2006.

[93] J. G. Pharoah and O. S. Burheim, “On the temperature distribution in polymer electrolyte fuel cells,” *J. Power Sources*, vol. 195, no. 16, pp. 5235–5245, 2010.

[94] A. Hakenjos, H. Muenter, U. Wittstadt, and C. Hebling, “A PEM fuel cell for combined measurement of current and temperature distribution, and flow field flooding,” *J. Power Sources*, vol. 131, no. 1–2, pp. 213–216, May 2004.

[95] H. Lin, T.-F. Cao, L. Chen, Y.-L. He, and W.-Q. Tao, “In situ measurement of temperature distribution within a single polymer electrolyte membrane fuel cell,” *Int. J. Hydrogen Energy*, vol. 37, no. 16, pp. 11871–11886, Aug. 2012.

[96] K. Jiao, I. E. Alaefour, G. Karimi, and X. Li, “Simultaneous measurement of current and temperature distributions in a proton exchange membrane fuel cell during cold start processes,” *Electrochim. Acta*, vol. 56, no. 8, pp. 2967–2982, Mar. 2011.

[97] E. Afshari, S. A. Jazayeri, and Y. Mollayi Barzi, “Effect of water phase change on temperature distribution in proton exchange membrane fuel cells,” *Heat Mass Transf.*, vol. 46, no. 11–12, pp. 1295–1305, 2010.

[98] H. Guo, M. H. Wang, F. Ye, and C. F. Ma, “Experimental study of temperature distribution on anodic surface of MEA inside a PEMFC with parallel channels flow bed,” *Int. J. Hydrogen Energy*, vol. 37, no. 17, pp. 13155–13160, 2012.

[99] C. Y. Lee, W. J. Hsieh, and G. W. Wu, “Embedded flexible micro-sensors in MEA for measuring temperature and humidity in a micro-fuel cell,” *J. Power Sources*, vol. 181, no. 2, pp. 237–243, 2008.

[100] H.-S. Kim and K. Min, “An experimental investigation of temperature distribution and flooding phenomena of cathode flow fields in a proton exchange membrane (PEM) fuel cell,” *J. Mech. Sci. Technol.*, vol. 28, no. 9, pp. 3837–3843, 2014.

[101] J. O’Rourke, M. Ramani, and M. Arcak, “In situ detection of anode flooding of a PEM fuel cell,” *Int. J. Hydrogen Energy*, vol. 34, no. 16, pp. 6765–6770, 2009.

[102] S. Ge and C.-Y. Wang, “Liquid Water Formation and Transport in the PEFC

Anode," *J. Electrochem. Soc.*, vol. 154, no. 10, p. B998, 2007.

[103] M. M. Daino, Z. Lu, J. M. LaManna, J. P. Owejan, T. a. Trabold, and S. G. Kandlikar, "Through-Plane Water Transport Visualization in a PEMFC by Visible and Infrared Imaging," *Electrochem. Solid-State Lett.*, vol. 14, no. 6, p. B51, 2011.

[104] K. Nishida, Y. Yokoi, K. Umeda, S. Tsushima, and S. Hirai, "Measurement of water, temperature and current distributions in anode of polymer electrolyte fuel cell during low humidity operation," pp. 1–8, 2016.

[105] L. Wang, "A parametric study of PEM fuel cell performances," *Int. J. Hydrogen Energy*, vol. 28, no. 11, pp. 1263–1272, Nov. 2003.

[106] Q. Jian, G. Ma, and X. Qiu, "Influences of gas relative humidity on the temperature of membrane in PEMFC with interdigitated flow field," *Renew. Energy*, vol. 62, pp. 129–136, Feb. 2014.

[107] K. H. Wong, K. H. Loo, Y. M. Lai, S.-C. Tan, and C. K. Tse, "A theoretical study of inlet relative humidity control in PEM fuel cell," *Int. J. Hydrogen Energy*, vol. 36, no. 18, pp. 11871–11885, Sep. 2011.

[108] M. Tohidi, S. H. Mansouri, and H. Amiri, "Effect of primary parameters on the performance of PEM fuel cell," *Int. J. Hydrogen Energy*, vol. 35, no. 17, pp. 9338–9348, Sep. 2010.

[109] J. Zhang, Y. Tang, C. Song, Z. Xia, H. Li, H. Wang, and J. Zhang, "PEM fuel cell relative humidity (RH) and its effect on performance at high temperatures," *Electrochim. Acta*, vol. 53, no. 16, pp. 5315–5321, Jun. 2008.

[110] X.-D. Wang, Y.-Y. Duan, W.-M. Yan, and F.-B. Weng, "Effect of humidity of reactants on the cell performance of PEM fuel cells with parallel and interdigitated flow field designs," *J. Power Sources*, vol. 176, no. 1, pp. 247–

258, Jan. 2008.

[111] G. H. Guvelioglu and H. G. Stenger, “Flow rate and humidification effects on a PEM fuel cell performance and operation,” *J. Power Sources*, vol. 163, no. 2, pp. 882–891, Jan. 2007.

[112] M. M. Saleh, T. Okajima, M. Hayase, F. Kitamura, and T. Ohsaka, “Exploring the effects of symmetrical and asymmetrical relative humidity on the performance of H2/air PEM fuel cell at different temperatures,” *J. Power Sources*, vol. 164, no. 2, pp. 503–509, Feb. 2007.

[113] Q. Yan, H. Toghiani, and H. Causey, “Steady state and dynamic performance of proton exchange membrane fuel cells (PEMFCs) under various operating conditions and load changes,” *J. Power Sources*, vol. 161, no. 1, pp. 492–502, Oct. 2006.

[114] M. Amirinejad, S. Rowshanzamir, and M. H. Eikani, “Effects of operating parameters on performance of a proton exchange membrane fuel cell,” *J. Power Sources*, vol. 161, no. 2, pp. 872–875, Oct. 2006.

[115] L. Wang and H. Liu, “Performance studies of PEM fuel cells with interdigitated flow fields,” *J. Power Sources*, vol. 134, no. 2, pp. 185–196, Aug. 2004.

[116] M. V. Williams, H. R. Kunz, and J. M. Fenton, “Operation of Nafion®-based PEM fuel cells with no external humidification: influence of operating conditions and gas diffusion layers,” *J. Power Sources*, vol. 135, no. 1–2, pp. 122–134, Sep. 2004.

[117] W. Lee and J. Van Zee, “Effect of Humidity on PEM Fuel Cell Performance: Part I-Experiments,” *Proc. ASME, Heat Transf. Div.*, vol. 364–1, pp. 356–366, 1999.

[118] E. Misran, N. S. M. Hassan, W. R. W. Daud, E. H. Majlan, and M. I. Rosli, “Water transport characteristics of a PEM fuel cell at various operating pressures and temperatures,” *Int. J. Hydrogen Energy*, vol. 38, no. 22, pp. 9401–9408, Jul. 2013.

[119] P. K. Sinha, C.-Y. Wang, and U. Beuscher, “Transport Phenomena in Elevated Temperature PEM Fuel Cells,” *J. Electrochem. Soc.*, vol. 154, no. 1, p. B106, 2007.

[120] D. Rohendi, E. H. Majlan, A. B. Mohamad, W. R. W. Daud, A. A. H. Kadhum, and L. K. Shyuan, “Effects of temperature and backpressure on the performance degradation of MEA in PEMFC,” *Int. J. Hydrogen Energy*, vol. 40, no. 34, pp. 10960–10968, 2015.

[121] M. Bilgili, M. Bosomoiu, and G. Tsotridis, “Gas flow field with obstacles for PEM fuel cells at different operating conditions,” *Int. J. Hydrogen Energy*, vol. 40, no. 5, pp. 2303–2311, 2015.

[122] D. Spernjak, A. K. Prasad, and S. G. Advani, “In situ comparison of water content and dynamics in parallel, single-serpentine, and interdigitated flow fields of polymer electrolyte membrane fuel cells,” *J. Power Sources*, vol. 195, no. 11, pp. 3553–3568, Jun. 2010.

[123] F. Barbir, “Pem F Uel C Ells Theory and Practice,” *Elsevier*, p. 543, 2013.

[124] Y. Wang, C. Y. Wang, and K. S. Chen, “Elucidating differences between carbon paper and carbon cloth in polymer electrolyte fuel cells,” *Electrochim. Acta*, vol. 52, no. 12, pp. 3965–3975, 2007.

[125] V. Gurau, M. J. Bluemle, E. S. De Castro, Y. M. Tsou, J. A. Mann, and T. A. Zawodzinski, “Characterization of transport properties in gas diffusion layers for proton exchange membrane fuel cells. 1. Wettability (internal contact

angle to water and surface energy of GDL fibers),” *J. Power Sources*, vol. 160, no. 2 SPEC. ISS., pp. 1156–1162, 2006.

[126] V. Gurau, M. J. Bluemle, E. S. De Castro, Y. M. Tsou, T. A. Zawodzinski, and J. A. Mann, “Characterization of transport properties in gas diffusion layers for proton exchange membrane fuel cells. 2. Absolute permeability,” *J. Power Sources*, vol. 165, no. 2, pp. 793–802, 2007.

[127] J. G. Pharoah, “On the permeability of gas diffusion media used in PEM fuel cells,” *J. Power Sources*, vol. 144, no. 1, pp. 77–82, 2005.

[128] J. T. Gostick, M. W. Fowler, M. D. Pritzker, M. A. Ioannidis, and L. M. Behra, “In-plane and through-plane gas permeability of carbon fiber electrode backing layers,” *J. Power Sources*, vol. 162, no. 1, pp. 228–238, 2006.

[129] N. Zamel and X. Li, “Effective transport properties for polymer electrolyte membrane fuel cells - With a focus on the gas diffusion layer,” *Prog. Energy Combust. Sci.*, vol. 39, no. 1, pp. 111–146, 2013.

[130] M. S. Ismail, T. Damjanovic, K. Hughes, D. B. Ingham, L. Ma, M. Pourkashanian, and M. Rosli, “Through-Plane Permeability for Untreated and PTFE-Treated Gas Diffusion Layers in Proton Exchange Membrane Fuel Cells,” *J. Fuel Cell Sci. Technol.*, vol. 7, no. 5, p. 51016, 2010.

[131] D. H. Ahmed, H. J. Sung, and J. Bae, “Effect of GDL permeability on water and thermal management in PEMFCs-I. Isotropic and anistropic permeability,” *Int. J. Hydrogen Energy*, vol. 33, no. 14, pp. 3786–3800, 2008.

[132] O. M. Orogbemi, D. B. Ingham, M. S. Ismail, K. J. Hughes, L. Ma, and M. Pourkashanian, “The effects of the composition of microporous layers on the permeability of gas diffusion layers used in polymer electrolyte fuel cells,” *Int. J. Hydrogen Energy*, vol. 41, no. 46, pp. 21345–21351, 2016.

[133] M. S. Ismail, D. Borman, T. Damjanovic, D. B. Ingham, and M. Pourkashanian, “On the through-plane permeability of microporous layer-coated gas diffusion layers used in proton exchange membrane fuel cells,” *Int. J. Hydrogen Energy*, vol. 36, no. 16, pp. 10392–10402, 2011.

[134] O. M. Orogbemi, D. B. Ingham, M. S. Ismail, K. J. Hughes, L. Ma, and M. Pourkashanian, “Through-plane gas permeability of gas diffusion layers and microporous layer: Effects of carbon loading and sintering,” *J. Energy Inst.*, 2016.

[135] A. Tamayol, F. McGregor, and M. Bahrami, “Single phase through-plane permeability of carbon paper gas diffusion layers,” *J. Power Sources*, vol. 204, pp. 94–99, 2012.

[136] J. Ihonen, M. Mikkola, and G. Lindbergh, “Flooding of Gas Diffusion Backing in PEFCs,” *J. Electrochem. Soc.*, vol. 151, no. 8, p. A1152, 2004.

[137] M. I. Rosli, D. J. Borman, D. B. Ingham, M. S. Ismail, L. Ma, and M. Pourkashanian, “Transparent PEM Fuel Cells for Direct Visualization Experiments,” *J. Fuel Cell Sci. Technol.*, vol. 7, no. 6, p. 61015, 2010.

[138] M. I. Rosli, “Water Management in PEM Fuel Cell Gas Distributor Plates,” University of Leeds, 2011.

[139] M. J. Assael, S. Botsios, K. Gialou, and I. N. Metaxa, “Thermal conductivity of polymethyl methacrylate (PMMA) and borosilicate crown glass BK7,” *Int. J. Thermophys.*, vol. 26, no. 5, pp. 1595–1605, 2005.

[140] D. Shou, Y. Tang, L. Ye, J. Fan, and F. Ding, “Effective permeability of gas diffusion layer in proton exchange membrane fuel cells,” *Int. J. Hydrogen Energy*, vol. 38, no. 25, pp. 10519–10526, 2013.

[141] E. Afshari, M. Ziaei-Rad, and M. M. Dehkordi, “Numerical investigation on a

novel zigzag-shaped flow channel design for cooling plates of PEM fuel cells," *J. Energy Inst.*, pp. 1–12, 2016.

[142] G.-L. Hu, J.-R. Fan, and Y.-Q. Zheng, "CFD based two-phase modelling of proton exchange membrane fuel cell with interdigitated flow field," *J. Energy Inst.*, vol. 83, no. 2, pp. 93–100, 2002.

[143] S. Patel, A. S. Bansode, T. Sundararajan, and S. K. Das, "The Performance Analysis of a Multi-Duct Proton Exchange Membrane Fuel Cell Cathode," *Int. J. Green Energy*, vol. 5, no. 1–2, pp. 35–54, 2008.

[144] Y. H. Park and J. A. Caton, "Monitoring an Electrode Flooding Through the Back Pressure in a Proton Exchange Membrane (PEM) Fuel Cell," *Int. J. Green Energy*, vol. 5, no. 5, pp. 347–359, 2008.

[145] J. Zhang, C. Song, J. Zhang, R. Baker, and L. Zhang, "Understanding the effects of backpressure on PEM fuel cell reactions and performance," *J. Electroanal. Chem.*, vol. 688, pp. 130–136, 2013.

[146] J. Zhang, H. Li, Z. Shi, and J. Zhang, "Effects of Hardware Design and Operation Conditions on PEM Fuel Cell Water Flooding," *Int. J. Green Energy*, vol. 7, no. 5, pp. 461–474, 2010.

[147] A. Bozorgnezhad, M. Shams, H. Kanani, M. Hasheminasab, and G. Ahmadi, "The experimental study of water management in the cathode channel of single-serpentine transparent proton exchange membrane fuel cell by direct visualization," *Int. J. Hydrogen Energy*, vol. 40, no. 6, pp. 2808–2832, 2015.

[148] G. Hu, G. Li, Y. Zheng, Z. Zhang, and Y. Xu, "Optimization and parametric analysis of PEMFC based on an agglomerate model for catalyst layer," *J. Energy Inst.*, vol. 87, no. 2, pp. 163–174, 2014.

[149] B. P. Saripella, U. O. Koylu, and M. C. Leu, "Experimental and

Computational Evaluation of Performance and Water Management Characteristics of a Bio-Inspired Proton Exchange Membrane Fuel Cell," *J. Fuel Cell Sci. Technol.*, vol. 12, no. 6, p. 61007, 2015.

[150] P. Quan, B. Zhou, A. Sobiesiak, and Z. Liu, "Water behavior in serpentine micro-channel for proton exchange membrane fuel cell cathode," *J. Power Sources*, vol. 152, no. 1–2, pp. 131–145, 2005.

[151] T. Ous and C. Arcoumanis, "Visualisation of water droplets during the operation of PEM fuel cells," *J. Power Sources*, vol. 173, no. 1, pp. 137–148, 2007.

[152] E. Kimball and T. Whitaker, "Drops, slugs, and flooding in polymer electrolyte membrane fuel cells," *AIChE*, vol. 54, no. 5, 2008.

[153] Z. Lu, S. G. Kandlikar, C. Rath, M. Grimm, W. Domigan, a. D. White, M. Hardbarger, J. P. Owejan, and T. a. Trabold, "Water management studies in PEM fuel cells, Part II: Ex situ investigation of flow maldistribution, pressure drop and two-phase flow pattern in gas channels," *Int. J. Hydrogen Energy*, vol. 34, no. 8, pp. 3445–3456, May 2009.

[154] M. Rosli, D. Borman, D. Ingham, Ismail, L. Ma, and M. Pourkashanian, "Transparent PEM Fuel Cells for Direct Visualization Experiments," *J. Fuel Cell Sci. Technol.*, vol. 7, no. 6, p. 61015, 2010.

[155] M. M. Daino, Z. Lu, J. LaManna, J. Owejan, T. Trabold, and S. G. Kandlikar, "Through-Plane Water Transport Visualization in an Operating PEM Fuel Cell by Visible and Infrared Imaging," *Ecs …*, vol. 33, no. 1, pp. 1423–1433, 2010.

[156] W. Yuan, A. Wang, Z. Yan, Z. Tan, Y. Tang, and H. Xia, "Visualization of two-phase flow and temperature characteristics of an active liquid-feed direct

methanol fuel cell with diverse flow fields,” *Appl. Energy*, vol. 179, pp. 85–98, 2016.

[157] I. S. Hussaini and C.-Y. Wang, “Visualization and quantification of cathode channel flooding in PEM fuel cells,” *J. Power Sources*, vol. 187, no. 2, pp. 444–451, Feb. 2009.

[158] M. Yamauchi, K. Sugiura, T. Yamauchi, T. Taniguchi, and Y. Itoh, “Proposal for an optimum water management method using two-pole simultaneous measurement,” *J. Power Sources*, vol. 193, no. 1, pp. 1–8, 2009.

[159] A. Su, F. Weng, C. Hsu, and Y. Chen, “Studies on flooding in PEM fuel cell cathode channels,” *Int. J. Hydrogen Energy*, vol. 31, no. 8, pp. 1031–1039, Jul. 2006.

[160] “ClearPak single cells – Pragma Industries.” [Online]. Available: https://www.pragma-industries.com/products/lab-equipment/clearpak/. [Accessed: 07-Feb-2018].

[161] M. S. Ismail, D. B. Ingham, K. J. Hughes, L. Ma, and M. Pourkashanian, “Thermal modelling of the cathode in air-breathing PEM fuel cells,” *Appl. Energy*, vol. 111, pp. 529–537, 2013.

[162] M. S. Ismail, D. B. Ingham, K. J. Hughes, L. Ma, and M. Pourkashanian, “An efficient mathematical model for air-breathing PEM fuel cells,” *Appl. Energy*, vol. 135, pp. 490–503, 2014.

[163] R. M. Aslam, D. B. Ingham, M. S. Ismail, K. J. Hughes, L. Ma, and M. Pourkashanian, “Simultaneous direct visualisation of liquid water in the cathode and anode serpentine flow channels of proton exchange membrane (PEM) fuel cells,” *J. Energy Inst.*, pp. 1–14, 2017.

[164] A. Oshima, Y. Tabata, H. Kudoh, and T. Seguchi, “Radiation induced

crosslinking of polytetrafluoroethylene," *Radiat. Phys. Chem.*, vol. 45, no. 2, pp. 269–273, 1995.

[165] M. S. Ismail, T. Damjanovic, D. B. Ingham, M. Pourkashanian, and a. Westwood, "Effect of polytetrafluoroethylene-treatment and microporous layer-coating on the electrical conductivity of gas diffusion layers used in proton exchange membrane fuel cells," *J. Power Sources*, vol. 195, no. 9, pp. 2700–2708, 2010.